ROYAL INSTITUTE
OF TECHNOLOGY

Spectral Management in Quasi-Phase-Matched Parametric Devices

Mikael Tiihonen

Doctoral Thesis
Department of Applied Physics
Royal Institute of Technology
Stockholm
Sweden
2006

Royal Institute of Technology
Department of Applied Physics - Laser Physics
Albanova
Roslagstullsbacken 21
SE-106 91 Stockholm, Sweden

Akademisk avhandling som med tillstånd av Kungliga Tekniska Högskolan framlägges till offentlig granskning för avläggande av teknologie doktorsexamen i fysik, tisdagen den 13 juni 2006, kl. 10 i Sal FD5, Albanova, Roslagstullsbacken 21, Stockholm.
Avhandligen kommer att försvaras på engelska.

TRITA-FYS 2006:37
ISSN 0280-316X
ISRN KTH/FYS/--06:37--SE

ISBN 91-7178-379-2

Printed by Universitetsservice AB, Stockholm 2006.

Mikael Tiihonen, *Spectral Management in Quasi-Phase-Matched Parametric Devices*,
Royal Institute of Technology, Department of Applied Physics - Laser Physics, SE-106 91 Stockholm, Sweden.

Abstract

Nonlinear optical interaction in quasi-phase-matched structures opens up unique possibilities to build compact and efficient parametric devices such as optical parametric oscillators, generators, and amplifiers with tailored spectral properties. The focus of this thesis is on novel parametric interactions with periodically-poled $KTiOPO_4$ (PPKTP) as the parametric gain medium.

Optical parametric oscillators (OPOs) are attractive light sources for many applications, particularly in spectroscopy, and plays a central role in this thesis. Special attention is put on simple, yet powerful, spectral-manipulation and bandwidth-narrowing techniques for OPOs. The overall knowledge gained from these studies has been used for device construction of several tunable ultraviolet sources for biological sensing.

In the case of bandwidth narrowing, the observation of decreasing spectral bandwidth in a noncollinear, idler-resonant OPO, as compared with a signal-resonant one, has been found to be due to the interplay between the material properties and the angular dispersion of PPKTP. To further reduce the bandwidth, we have shown that it is very beneficial to replace the output mirror in an OPO with a bulk Bragg grating. In fact, even close to degeneracy, where the bandwidth is typically wide, this approach is able to decrease the bandwidth drastically.

Moreover, different OPO cavity designs have been examined in order to spectrally manipulate the resonant waves. By deploying a grating in a ring OPO cavity, it becomes possible to access the resonant wave and spectrally manipulated it in a zero-dispersion arrangement; the filtered wave is subsequently sent back into its own cavity as a seed signal, in a self-seeding arrangement. This particular cavity design decreases the bandwidth close to ~ 1000 times as compare to the free-running mode. An interesting phenomenon arises when two mutually coherent laser beams are used to pump a linear OPO cavity. When the pump beams intersect within the PPKTP crystal, an interference grating is formed and acts as a catalyst for the generation of new spectral sidebands through multiple cascaded four-wave mixing, in the pump, the idler and the signal directions. The spacing of these sidebands is determined geometrically by the incident pump angle, while the signals are continuously tunable over the c-band telecom window ($\lambda \sim 1.5$ μm) by rotating the cavity.

Ultrabroad bandwidths have been generated in an optical parametric generator (OPG) pumped by an amplified picosecond Ti:sapphire laser. In the collinear direction the output spectrum extends over three octaves in the mid-infrared region. This enormously broad spectrum is also Fourier-filtered and subsequently used for narrowband seeding of an optical parametric amplifier (OPA).

Finally, the spectral range between 285 nm and 340 nm is of importance for detection of biological substances through fluorescence spectroscopy. With this spectral region in mind a practical way to generate a tunable parametric device in the ultraviolet region is presented in the thesis. The developed ultraviolet laser is used for studies of the characteristics of biological particles. The ultraviolet source and the results from these studies, will be utilized in an integrated detection system, a so called early-warning system.

Keywords: optical parametric devices, nonlinear optics, ultraviolet generation, mid-infrared generation, optical parametric oscillator, optical parametric generator, optical parametric amplifier, $KTiOPO_4$, frequency conversion, tunable parametric device.

TRITA-FYS 2006:37; ISSN 0280-316X; ISRN KTH/FYS/--06:37--SE; ISBN 91-7178-379-2

To my two lovely girls at home Minna and Anna

In loving memory of my Mother

Preface

The studies treated in this thesis were mainly conducted at the Department of Applied Physics at the Royal Institute of Technology, Stockholm, Sweden from February 2002 to June 2006.

Throughout the project time continuous collaboration with Professor M. Lindgren, Dr P. Jonsson, Dr F. Kullander, Dr T. Tjärnhage, G. Olofsson and P. Wästerby at FOI - Swedish Defence Research Agency has been conducted within the frame of the biological sensing project.

The studies were sponsored by FOI - Swedish Defence Research Agency, FMV - Swedish Defence Material Administration, and the Western European Armaments Organisation in Brussels, Belgium.

The thesis is a summary of seven articles. In the introductory part a short historical outline of the field of nonlinear optics is given, which is followed by an overview of nonlinear optics theory. The remaining Chapters treat the experimental studies and are ended with the concluding remarks. The relevant articles are reprinted at the end.

List of Publications

Publications included in the thesis

I. M. Tiihonen, V. Pasiskevicius and F. Laurell, *Spectral and spatial limiting in an idler-resonant PPKTP optical parametric oscillator*, Optics Communication **250**, 207 (2005).

II. B. Jacobsson, M. Tiihonen, V. Pasiskevicius and F. Laurell, *Narrowband bulk Bragg grating optical parametric oscillator*, Optics Letters **30**, 2281 (2005).

III. M. Tiihonen, V. Pasiskevicius and F. Laurell, *Noncollinear double-ring optical parametric oscillators with periodically poled $KTiOPO_4$*, Optics Express **12**, 5526 (2004).

IV. M. Tiihonen and V. Pasiskevicius, *2D Quasi-Phase-Matched Multiple-Cascaded Four-Wave Mixing in a Periodically Poled $KTiOPO_4$*, Submitted to Optics Letter in May 2006.

V. M. Tiihonen, V. Pasiskevicius, A. Fragemann, C. Canalias and F. Laurell, *Ultrabroad Gain in an Optical Parametric Generator with periodically poled $KTiOPO_4$*, Accepted for publication in Applied Physics B in March 2006.

VI. M. Tiihonen, V. Pasiskevicius, and F. Laurell, *Broadly Tunable Picosecond Narrowband pulses in a periodically poled $KTiOPO_4$ parametric amplifier,* Submitted to Optics Express in May 2006.

VII. M. Tiihonen, V. Pasiskevicius and F. Laurell, *Tailored UV-laser source for fluorescence spectroscopy of biomolecules*, Accepted for publication in Optics and Lasers in Engineering in March 2005.

Publications not included in the thesis

A1. M. Tiihonen, V. Pasiskevicius, F. Laurell, P. Hammarström and M. Lindgren, *A UV laser source for biological and chemical sensing***,** Proceedings of SPIE **5240**, 127 (2003).

A2. M. Tiihonen, V. Pasiskevicius, F. Laurell, P. Jonsson and M. Lindgren, *A compact OPO/SFG laser for ultraviolet biological sensing*, Proceedings of SPIE **5332**, 134 (2004).

A3. B. Agate, E. U. Rafailov, W. Sibbett, S. M. Saltiel, K. Koinov, M. Tiihonen, S. Wang, F. Laurell, P. Battle, T. Fry, T. Roberts and E. Noonan, *Portable ultrafast blue light sources*, IEEE Journal on Selected Topics in Quantum Electronics **10,** 1268 (2004).

A4. M. Tiihonen, V. Pasiskevicius, F. Laurell and M. Lindgren, *A novel UV-laser source for fluorescence excitation of proteins*, Proceedings of SPIE **5617**, 261 (2004).

A5. P. Jonsson, F. Kullander, P. Wästerby, M. Tiihonen and M. Lindgren, *Detection of fluorescence spectra of individual bioaerosol particles*, Proceedings of SPIE **5990B**, 151 (2005).

A6. M. Henriksson, M. Tiihonen, V. Pasiskevicius and F. Laurell, *$ZnGeP_2$ Parametric Oscillator Pumped by a Linewidth Narrowed Parametric 2 μm Source*, Optics Letter **31**, July (2006).

A7. P. Jonsson, F. Kullander, M. Tiihonen, M. Nordstrand, T. Tjärnhage, P. Wäasterby, G. Olofsson, and M. Lindgren, *Development of Fluorescence-Based LIDAR for Biological Sensing*, Materials Research Society Symposium Proceeding **883**, FF1.6.1 (2005).

The articles will be referred to in the text by their respective notation above.

Acknowledgements

Firstly, I would like to express my thanks to Professor Fredrik Laurell for accepting me as a PhD student in his group. He has always helped and supported me whenever I was in trouble, and his endless “happy energy” has lightened up my mood more than once. Thanks for giving me the opportunity to visit and work in different parts of the world; it has been a fantastic experience.

Without the help, encouragement, and guidance from Dr Valdas Pasiskevicius the many long days in the lab would have been fruitless. His vast experience in experimental work and physics has been a great inspiration. Especially, when we together develop “high-tech” solutions with a piece of scotch-tape and a dull razorblade. Thanks for always taking the time with me and explaining advanced physics, as well as having the patience to explain *kindergarten* physics to me.

It has been a pleasure to be a part of the Laser Physics Group, where all the people are really fantastic. I would like to thank all the present and the former co-workers for all the help and joy you have given me throughout these years. Special thanks goes to: Dr Carlota Canalias for not being so PhD-ish, Stefan Holmgren for always having the time to talk, Björn Jakobsson for fruitful collaboration, Sandra Johansson for bringing me cookies in the lab, Junji Hirohashi for buying my first car ever, Marcus Alm for learning me that one can survive on noodles (if necessary), Assoc. Prof. Jens A. Tellefsen for updating me on what’s up in Scotland and for coerctring my swenglish, Dr Stefan Bjurshagen for lending me his equipment, Pär Jelger for helping me with everything from computers to where the best clothes are bought, Dr Anna Fragemann for poling nice crystals, Lars-Gunnar Andersson for making fresh coffee each morning, Dr Stefan Spiekermann for northern-light lectures in the lab, and finally Jonas Hellström (Jr.) for putting up with me (and I with him).

Within KTH there is a number of people that have made my work much easier and interesting, and they are: Agneta Falk for helping me with all travel arrangements and administrative issue, Rolf Helg for fabricating all my crazy ideas in the mechanical workshop, Dr Göran Manneberg for introducing me to Fredrik in the first place and letting me teach undergraduate students, and the guys at *godsmottagningen* for all the help with package going from here to there.

I would also like to thank my colleagues at FOI Professor Mikael Lindgren, Dr Fredrik Kullander and Dr Per Jonsson for great times in Linköping, Umeå, and London. It was always a nice break from KTH to come and work with you guys. Without the generous support from FOI and FMV (Kenth Henningsson), this thesis would not have been possible. Furthermore, thanks to Markus Henriksson at FOI for introducing me to mid-infrared optics.

Moreover, thanks to all the people at Cobolt for helping me with spare optics and crystals whenever I had broken something in my lab. My gratitude goes primarily to Mats Hede, Dr Håkan Karlsson and Dr Jonas Hellström (Sr.).

I would also like to thank my colleagues involved in the European consortium FABIOLA. Especially, Gilles Feugnet at Thales (France), Dr Krzysztof Kopczynski, Dr Zbigniew Zawadzki and Dr Miroslaw Kwasny at the Military University of Technology Warsaw (Poland), for interesting collaboration and sightseeing when visiting Paris and Warsaw.

Unconditional love goes out to all my friends who have support me and telling me what’s important in life and foremost for making me laugh whenever I needed it the best. I will not mention any names, in case I forget someone, but you know who you are. You are the greatest inspiration!

Last, but not least important, my family and my beautiful fiancé Anna (and her family), they have been by my side all the way, and supported me with love and encouragement at difficult and good times. I am so happy to say that there has been an addition to our growing family. Our beautiful daughter *Minna* came to the world on the 16th of February (2006). Finally, I love you Anna!

Table of Contents

CHAPTER 1. INTRODUCTION 1

1.1 Background 1
1.2 Development of the work 2
1.3 Outline of the thesis 4

CHAPTER 2. NONLINEAR OPTICS THEORY 5

2.1 Higher Order Susceptibilities 5
2.2 The Coupled Wave Equations 7
2.3 Harmonic and Parametric Processes 8
2.3.1 Second Harmonic Generation and Frequency Mixing 9
2.3.2 Optical Parametric Generation 10
2.3.3 Optical Parametric Oscillator 11
2.3.4 Optical Parametric Amplification 13
2.3.5 Cascaded Interactions 13

CHAPTER 3. PHASE-MATCHING 15

3.1 Birefringent Phase-matching 15
3.2 Quasi-Phase-matching 17
3.3 Nonlinear Optical Crystals 20

CHAPTER 4. OPTICAL PARAMETRIC OSCILLATORS 23

4.1 Novel Linewidth Narrowing Techniques 23
4.1.1 Idler Resonant Optical Parametric Oscillator 24
4.1.2 Bulk Bragg Grating as an Output Coupler 28
4.1.4 Self-Seeded Optical Parametric Oscillator 31
4.2 Cascaded Second-Order Interactions 36

CHAPTER 5. BROADBAND PARAMETRIC GENERATION AND AMPLIFICATION 41

5.1 Towards Ultra-Broad Spectral Bandwidths 42
5.2 Parametric Amplification 45

CHAPTER 6. APPLICATION - BIOLOGICAL SENSING 51

6.1 Low frequency - The Ultraviolet Laser Source 52
6.1.1 Beam shaping of a Diode Bar and Construction of a pulsed Nd:YAG Laser 52
6.1.2 Intra-cavity Sum-Frequency Mixing in an Optical Parametric Oscillator 53
6.2 Detecting Biological Particels 54
6.3 The FABIOLA Consortium 56
6.3.1 High Frequency - The Ultraviolet Laser Source 56

CHAPTER 7. DESCRIPTION OF WORK AND AUTHOR CONTRIBUTION 59

CHAPTER 8. CONCLUSIONS 63

REFERENCES 65

Chapter 1

Introduction

1.1 Background

The field of nonlinear optics is the part of physics which studies the interaction between electromagnetic (light) waves inside optical materials. If we assume that the natural light surrounding us have relatively low intensity and when propagating through a material (e.g. windows, glasses, water) the constituent waves do not interact with each other. Then the response is said to be linear and this is what we see in our daily lives. However, if light of high enough intensity is incident on a material, the response will be nonlinear and the waves will interact with each other and with the material. This phenomenon will give rise to new optical frequencies and can be said to be the essence of nonlinear optics. These high intensities was not available until Maiman in 1960 demonstrated the first laser,[1] and this was essentially also the starting-point for the field of nonlinear optics. Shortly after, Franken *et al.* demonstrated frequency doubling of a ruby laser in crystalline quartz.[2] These two reports paved the way for an intense research activity in the fields of laser physics and nonlinear optics that still today attracts a lot of interest and continuous to evolve.

The number of applications for lasers today is enormous and they are found in biomedicine, heavy industry, IT, telecommunication, entertainment, etc. However, a conventional laser is restricted to a predetermined emission wavelength and is in general not tunable over a large spectral range. The reason is that the excitation and emission wavelengths of a laser are governed by the energy levels in the active ions, atoms or molecules that the gain medium consists of. Even so, one practical way of extending the tuning range is to combine the lasers with some nonlinear optical materials in a device and this makes it possible to access wavelength regions which are, in some cases, inaccessible to the lasers themselves. An over simplified scheme is that the laser acts as a pump source and the nonlinear optical material converts the frequency. In principle, with this kind of device, the spectral region from the ultra-violet to the mid-infrared is attainable.

Throughout the 1960s many important discoveries in the field of nonlinear optics were made. Practically all of the nonlinear-optical theory used to day dates back to this decade. A few of the many pioneering experiments from this period include: the first demonstration of a tunable optical parametric oscillator (OPO) by Giordmaine and Miller;[3] the observation of tunable optical parametric fluorescence by Byer *et al*.[4] and the demonstration of optical parametric amplification (OPA) by Wang and Racette.[5] The physical similarity of these parametric processes is that they distribute the pump photon energy into two parts and provides coherent radiation at two different frequencies.

Basically, second-order nonlinear phenomena consist of either splitting a pump photon into two or adding (or subtracting) two photons to generate one photon. This probably sound

too good to be true, and there are, of course, physical constraints. First, the energy conservation must be met; with the pump wave at frequency ω_3, the so called signal and idler waves at frequencies ω_1 and ω_2, respectively, must obey the relation $\omega_3 = \omega_1 + \omega_2$. Secondly, for the parametric process to be efficient, the interacting waves must be phase-matched, i.e., momentum conservation. All materials have frequency dependent refractive indices and care must be taken to ensure that the constituent waves are in phase with each other. At first, birefringent phasematching (BPM) was the only way to achieve adequate efficiencies in parametric devices. The technique was not optimal since BPM could not, in most cases, access the highest nonlinearities in the optical materials. The development of quasi-phase matching (QPM) technique led to an increased interest in the field of parametric frequency conversion. Undoubtedly, it was also prompted by the appearance of new nonlinear materials and laser sources in the 1980s and 1990s. The most efficient technique relies on periodic domain inversion in ferroelectric materials, and is able to access the highest nonlinearities. The impact of these QPM materials has led to the development of efficient, compact and, foremost, practical parametric devices. Presently, these devices are available on all time scales, from continuous wave to femtosecond pulses. Today they can be found in a widespread of applications, for example in atmospheric monitoring, time-resolved spectroscopy of semiconductors, confocal microscopy and biological sensing.

The flexibility and utilization areas of these parametric devices are still evolving in parallel with the advances in material science. For example, improvements in the growth technique of nonlinear materials that have high nonlinearities in the mid-infra red region enables the operation of parametric devices past the transparency region of the common oxide based QPM materials, such as $LiNbO_3$ and $KTiOPO_4$ isomorphs. The various aspects of the field of nonlinear optics bring together different areas of research, ranging from material sciences and material processing to practical device construction, as well as applications. This is probably why the field is still vital, growing and attracts a lot of interest both from industry and academia.

1.2 Development of the work

This thesis project began with a preliminary study to investigate the possibility to construct tunable ultraviolet (UV) laser sources for biological sensing applications. The spectral range of interest for this particular application is between 285 nm to 340 nm, and at the beginning of the project there were no available laser systems capable of delivering these wavelengths in a practical way. However, by taking advantage of the mature technical status of the field of laser physics and QPM-technology, a viable and flexible way of generating these wavelengths was proposed and subsequently demonstrated. The UV-light is generated through a cascade of nonlinear processes using a nanosecond infrared (IR) laser as a pump source. The frequency conversion unit was built around an OPO with an intra-cavity sum-frequency mixing scheme. A new pump source was also developed to fit the requirements, it was a frequency-doubled Q-switched neodymium yttrium aluminium garnet (Nd:YAG) laser. The wavelength flexibility is possible by deploying periodically poled $KTiOPO_4$ (PPKTP) with different grating periods inside the OPO. Since KTP is not transparent in the UV, a barium borate (BBO) crystal sum-frequency mixed the OPO signal and the remaining pump to UV. With this device, the given wavelength region is accessible and measurements on biological substances are possible.[VII] This particular project has continued within an European consortium called FABIOLA, where the overall aim is to build a prototype of a detection system for biological agents, a so called early-warning system. The UV-converting unit was

built around the same technology as above, while the pump source needed to have a higher repetition rate.

However, to get a deeper understanding and to further explore the properties of PPKTP OPOs, a series of experiments were conducted in parallel with the above project. The main part is focused on novel passive bandwidth narrowing techniques for near-degenerate OPOs in the IR spectral range. These devices are pumped by nanosecond lasers emitting at 532 nm and 1064 nm.

An interesting form of line-narrowing, from a physical point of view, is by taking advantage of the intrinsic dispersion properties of the KTP crystal; for a given pump wavelength and QPM period the angular dispersion of the idler can be higher than for the signal. This favours an idler-resonant OPO, if the aim is to have a smaller bandwidth. Thus, by resonating the idler in a noncollinear OPO, the spectral bandwidth decreased two-times in comparison with a signal-resonant cavity and efficiencies of approximately 70 % are achieved in both cases.[I] Another advantage obtained by operating a noncollinear OPO is that it is truly singly-resonant, since the idler and the signal are not co-propagating and no backconversion is possible. Continuing the exploration of idler-resonant OPO cavities, a self-seeded doubled pumped OPO with independently counter-propagating idlers was studied. The OPO is now a ring cavity with a grating as the third mirror. Through the first-order diffraction from the grating, a small fraction of the forward propagating idler was coupled out, and spectrally filtered in a zero-dispersion arrangement. The filtered idler was then sent back into the same cavity, however now propagating in the opposite direction, and thus acted as a seed for the second pump. This self-seeding technique led to a drastic decrease of the spectral bandwidth by a factor of ~ 1000 by using a single OPO cavity and one beamsplit laser pump source.[III] To make things easier when designing narrow linewidth OPOs, a bulk Bragg grating was deployed as an output coupler in a linear OPO cavity. The experiment showed a spectral bandwidth of 50 GHz at 975 nm, which corresponded to a decrease in bandwidth of 20 times as compared to a conventional dielectric output mirror.[II] This simple and compact OPO has attracted a lot of interest from both industry and academia, since it has the ability to accommodate spectral narrowing at any spectral range of KTP's and bulk glass's transparency range.

Hence, the natural way was to further explore this novel OPO technique. In order to avoid photo-damaging of the ZnGeP (ZGP) crystals it must be pumped above 2 μm and one way of generating this is by using an OPO pumped at 1 μm. However, line-narrowing is required since the bandwidth at degeneracy is extremely broad and would also damage the ZGP crystal. Naturally, a bulk Bragg grating was used as an output coupler, which limited the bandwidth to approximately 37 GHz at 2008 nm. As a result, the ZGP OPO could be pumped efficiently without any damage to the crystal, and a tunable output between 3.3 μm and 5.2 μm was achieved.[A6] However, this particular work is not part of the Thesis.

To conclude the studies made with OPOs, we experimentally investigated cascaded interactions in a double-pumped OPO. The pump beams were mutually coherent and generated a gain grating inside the PPKTP. This gave rise to two signal-idler pairs, which interacted through multiple-cascaded four-wave mixing processes. The processes produced frequency side-bands spaced by 1.5 THz in the spectral vicinity of the signals, the idlers and the pumps.[IV]

All of the above experiments were conducted in the nanosecond time scale and with the goal to generate narrow line-widths (except the work described in [IV]). The next step was to move to the picosecond time-scale and to generate ultrabroad bandwidths in an optical parametric generator (OPG) based on PPKTP. Ultrabroad bandwidth can be obtained by pumping at approximately one half the wavelength of the zero group-velocity dispersion point. According to our calculations this is around 900 nm. In the experiment we used an

amplified Ti:Sapphire laser as a pump source and found that the broadest parametric gain was for a pump wavelength of 827 nm and with a PPKTP crystal grating period of 28 μm. The spectral bandwidth was measured to 115 THz (FWHM) having a central wavelength of ~ 1650 nm.[V] The work continued by constructing an amplification stage for the ultrabroad bandwidth OPG source. First, however, the OPG seed output was spectrally filtered in a zero-dispersion arrangement, which enabled us to decreased the signal spectral bandwidth from 80 THz to 0.3 THz. The narrow linewidth signal seed was then amplified in a double-pass configuration in the OPA PPKTP crystal, with preserved spectral bandwidth, and reaching a small-signal parametric gain of 70 dB.[VI]

1.3 Outline of the thesis

The thesis is written as a summary of the studies described in the articles [I-VII]. The focus is on the versatile properties of periodically poled $KTiOPO_4$ crystals, when utilized in different parametric devices. Properties such as wavelength flexibility, spectral narrowing and manipulation, generation and amplification of ultrabroad bandwidths, and cascading effects are investigated and explained.

The outline of the thesis is as follows: Chapter 2 deals with the theory of nonlinear optics and the emphasis is on parametric interactions through the second-order susceptibility. In Chapter 3, birefringent and quasi-phase matching techniques are discussed and a short review of the nonlinear crystals used within the frame of this thesis is presented. The experiments conducted with optical parametric oscillators are further elaborated in Chapter 4 and theoretical considerations the regarding generation of narrow linewidths and cascaded interaction are explained. In Chapter 5, I deal with the investigation of the generation of ultrabroad bandwidths in a Ti:sapphire pumped periodically poled $KTiOPO_4$ optical parametric generator. It is followed by the amplification of the spectrally manipulated output. Chapter 6 is devoted to the development of the UV-laser and biological sensing, which has evolved into a “hot” topic over the last couple of years. The description of the original work and my contribution to each paper that I have published is presented in Chapter 7. Finally, I will conclude my work in Chapter 8.

Chapter 2

Nonlinear Optics Theory

When an electric field is propagating through a medium, it induces a response that depends on the strength of the electric field. In the case of lasers, the light will induce a nonlinear response which will lead to an interaction between the fields and with the medium to generate new optical frequencies. In the following subsections, I will in brief describe the nonlinear processes that are relevant to this thesis and give examples on a few applications. For a more thorough description of nonlinear optics found in text books, see references [6-8].

2.1 Higher Order Susceptibilities

Here, we are concerned with dielectric materials (non-conductive) and how the electromagnetic fields perturb the atoms within it. An optical wave oscillates at frequencies between $\sim 10^{12}$ - 10^{17} Hz, and induces motion of the charges inside the medium. This oscillatory behaviour of the electrical field creates electric dipoles, where the negatively charged electrons move in one direction and the positive ion in the opposite direction and thereby creating a time-varying polarization inside the material; whereas the magnetic field has a much lower effect on the dielectric and is not considered here. However, the mass of the ion is much greater than that for an electron and, thus, the induced movement will be more pronounced for the electron. In the linear regime, the electrons oscillate with the electric field, E, and the induced polarization can be approximated by:

$$P(t) = \varepsilon_0 \chi^{(1)} E(t), \tag{2.1}$$

where $P(t)$ is the induced polarization inside the dielectric, ε_0 is the permittivity in vacuum, and $\chi^{(1)}$ is the linear susceptibility and, in a mathematical description, it is a second-rank tensor. The $\chi^{(1)}$ has a real and an imaginary part, the real part being related to the refractive index, $n = \mathrm{Re}(1 + \chi^{(1)})^{1/2}$, while the imaginary part is related to the loss. Generally in physics, a linear approximation that depends on several different variables is only accurate over a limited range. Hence, when increasing the amplitude of the E-field, the above relation does not hold true any longer. The dipoles will not be able to follow the applied field's oscillation linearly and, as a consequence, the system will respond in a nonlinear manner. This induced nonlinear polarization will generate new spectral components at harmonic frequencies and, by expanding equation (2.1) in a perturbation series, these harmonic frequencies can now be derived:

$$P(t) = \varepsilon_0\left(\chi^{(1)}E(t) + \chi^{(2)}E^2(t) + \chi^{(3)}E^3(t) + ...\right), \tag{2.2}$$

where $\chi^{(2)}$, $\chi^{(3)}$,… are the nonlinear susceptibilities of the dielectric medium and the rank of the m:th order susceptibility tensor, $\chi^{(m)}$, is (m+1).[6-8] The magnitude of these susceptibilities decreases with the order m and requires higher and higher electrical fields in order to be observed. Later in this chapter, the distinction between $\chi^{(2)}$ and $\chi^{(3)}$ will be considered, with the focus on $\chi^{(2)}$. However, not all dielectrics have second-order nonlinearities, since this requires that the crystal lacks inversion symmetry, whereas the third-order nonlinearity is present in all materials. In nature, there are 32 crystal classes and 21 of them are non-centrosymmetric.[6]

Here, the $\chi^{(m)}$ is a matrix with the dimensions (m+1) and it consists of 3^{m+1} elements. For instance, the $\chi^{(2)}$ then has a matrix of the form 3×3×3 and it consists of 27 elements. Calculations with these kinds of matrices are cumbersome and can be avoided. If the overall permutation and Kleinman symmetry holds (all the field's frequencies are lossless and far away from resonances of the nonlinear medium),[9] the second-order susceptibility tensor can be contracted into a more convenient form employing the so-called *d*-tensor, with components given by:

$$2d_{\mu m}(-\omega_3;\omega_1,\omega_2) = \chi^{(2)}_{\mu\alpha\beta}(-\omega_3;\omega_1,\omega_2) = \chi^{(2)}_{\mu\beta\alpha}(-\omega_3;\omega_2,\omega_1) = \chi^{(2)}_{\mu\alpha\beta}(-\omega_3;\omega_2,\omega_1), \tag{2.3}$$

where the notation of reference [6] has been followed. The indices μ, α, and β are related to the polarization direction of the fields, i.e., the axes x, y, and z. The index m is a combination of the indices α and β.[6] This contracted *d*-tensor has a more convenient form of a 3 by 6 matrix with 18 independent elements. The interacting frequencies follow the energy conservation law, $\omega_3 = \omega_1 + \omega_2$, where ω_3 is the "new" frequency. In matrix form, the induced second-order nonlinear polarization, $P^{(2)}_{\omega_i}$, and its dependence on the electric fields are given by:

$$\begin{bmatrix} \left(P^{(2)}_{\omega_3}\right)_x \\ \left(P^{(2)}_{\omega_3}\right)_y \\ \left(P^{(2)}_{\omega_3}\right)_z \end{bmatrix} = 2\varepsilon_0 K \begin{bmatrix} d_{11} & d_{12} & d_{13} & d_{14} & d_{15} & d_{16} \\ d_{21} & d_{22} & d_{23} & d_{24} & d_{25} & d_{26} \\ d_{31} & d_{32} & d_{33} & d_{34} & d_{35} & d_{36} \end{bmatrix} \begin{bmatrix} \left(E_{\omega_1}\right)_x\left(E_{\omega_2}\right)_x \\ \left(E_{\omega_1}\right)_y\left(E_{\omega_2}\right)_y \\ \left(E_{\omega_1}\right)_z\left(E_{\omega_2}\right)_z \\ \left(E_{\omega_1}\right)_y\left(E_{\omega_2}\right)_z + \left(E_{\omega_2}\right)_y\left(E_{\omega_1}\right)_z \\ \left(E_{\omega_1}\right)_x\left(E_{\omega_2}\right)_z + \left(E_{\omega_2}\right)_x\left(E_{\omega_1}\right)_z \\ \left(E_{\omega_1}\right)_x\left(E_{\omega_2}\right)_y + \left(E_{\omega_2}\right)_x\left(E_{\omega_1}\right)_y \end{bmatrix}, \tag{2.4}$$

Here, the frequency arguments have been left out for convenience. The constant *K* represent the degeneracy factor and it has the value of 1/2 for second-harmonic generation and optical rectification, otherwise it is $K = 1$ for all other parametric processes. When evaluating the spatial properties of the crystal, the d-matrix can be further simplified. In many cases the spatial symmetry of the crystal imposes some of the $d_{\mu m}$-elements to vanish and some of the nonzero elements to be equal. This is an important factor to take into account when designing parametric devices, since it is beneficial to access the highest $d_{\mu m}$-coefficent in order to have highest conversion efficiency.

2.2 The Coupled Wave Equations

The propagation of all electromagnetic fields is governed by the Maxwell's equations. In the case of propagation in dielectric media, which do not have any free charges and low magnetic permeability, the Maxwell's equations are then reduced to the well known wave-equation:

$$\left(\nabla^2 - \frac{1}{c^2}\frac{\partial^2}{\partial t^2}\right)E(\bar{r},t) = \mu_0 \frac{\partial^2}{\partial t^2} P(\bar{r},t), \tag{2.5}$$

where c is the speed of light and μ_0 is the permeability of vacuum. The $\bar{r}$-vector is in Cartesian coordinates (x,y,z). Since this equation has derivatives both in space and time, equation (2.5) can be Fourier transformed. First, by considering the case of infinite plane wave approximation and unidirectional propagation, the quasi-monochromatic plane waves can be written in the Fourier domain as:

$$\widetilde{E}(x,\omega) = \frac{1}{2}\sum_{\omega}\left[\widetilde{E}_{\omega}(x)\exp\left[ik_{\omega}x\right] + c.c.\right], \tag{2.7}$$

Here, ω is the angular frequency of the waves and the wave vector $k_{\omega} = \omega n_{\omega}/c$, where n_{ω} is the frequency dependent refractive index. The losses are neglected and *c.c.* denotes the complex conjugate of the ***E***-fields. Then the Fourier transformed wave-equation takes the following form:

$$\left(\nabla^2 + \frac{\omega^2}{c^2}\varepsilon(\omega)\right)\widetilde{E}(\bar{r},\omega) = -\mu_0\omega^2\widetilde{P}^{NL}(\bar{r},\omega), \tag{2.6}$$

where the real part of $\varepsilon(\omega) = 1+\chi^{(1)}$, the real part is the refractive index square, $n^2(\omega)$, and the imaginary part being the losses. $\widetilde{P}^{NL}$ contains the higher order susceptibilities. Due to the linear and nonlinear processes, the amplitude, $\widetilde{E}_{\omega}$, varies over a spatial distance. However, if the fluctuations of the amplitude are slow over a distance of one wavelength, it is possible to approximate equation (2.6) to a first-order wave equation. In nonlinear optics, this is usually valid and it is commonly called the slow varying envelope approximation (SVEA):

$$\left|\frac{\partial^2\widetilde{E}_{\omega}}{\partial x^2}\right| << \left|k\frac{\partial\widetilde{E}_{\omega}}{\partial x}\right|, \tag{2.8}$$

Thus, by inserting equations (2.7) into (2.6) and, after some algebra, using SVEA, the wave equation then finally becomes:

$$\frac{\partial\widetilde{E}_{\omega}}{\partial x} = \frac{i\mu_0\omega^2}{2k_{\omega}}\widetilde{P}^{NL}\exp\left[-ik_{\omega}x\right], \tag{2.9}$$

where $\tilde{P}^{NL}$ is the arbitrary nonlinear polarization. The higher order terms can be seen in equation (2.2). In the case of the second-order susceptibility, the nonlinear polarization is given by equation (2.4), and it basically contains the interaction between three waves. These waves are coupled to each other through their induced polarizations and can be expressed by inserting equation (2.4) into the first-order wave equation [equation (2.9)]. This yields three coupled-wave equations and the result is usually expressed in scalar form:

$$\begin{aligned}
\frac{\partial E_1}{\partial x} &= \frac{i\omega_1^2}{k_1 c^2} K d_{eff} E_3 E_2^* \, exp[i\Delta kx], \\
\frac{\partial E_2}{\partial x} &= \frac{i\omega_2^2}{k_2 c^2} K d_{eff} E_3 E_1^* \, exp[i\Delta kx], \\
\frac{\partial E_3}{\partial x} &= \frac{i\omega_3^2}{k_3 c^2} K d_{eff} E_1 E_2 \, exp[-i\Delta kx],
\end{aligned} \tag{2.10}$$

where $\Delta k = k_3 - k_2 - k_1$ is the phase-mismatch between the interacting waves and $\omega_3 = \omega_1 + \omega_2$ preserves the energy conservation. The d_{eff} parameter is the effective nonlinear coefficient obtained from equation (2.3); that is, depending on the interacting waves' polarization, different nonlinear coefficients will be accessed. It will also depend on which phase-matching technique is used, more on this in the next chapter. With these sets of equations, all second-order nonlinear processes within the SVEA approximation can be calculated.

2.3 Harmonic and Parametric Processes

In this section the different harmonic and parametric processes that can be derived from the second-order nonlinear susceptibility tensor are described. Let us first consider a strong pump wave that is incident on a general nonlinear medium. The pump will, through the medium's

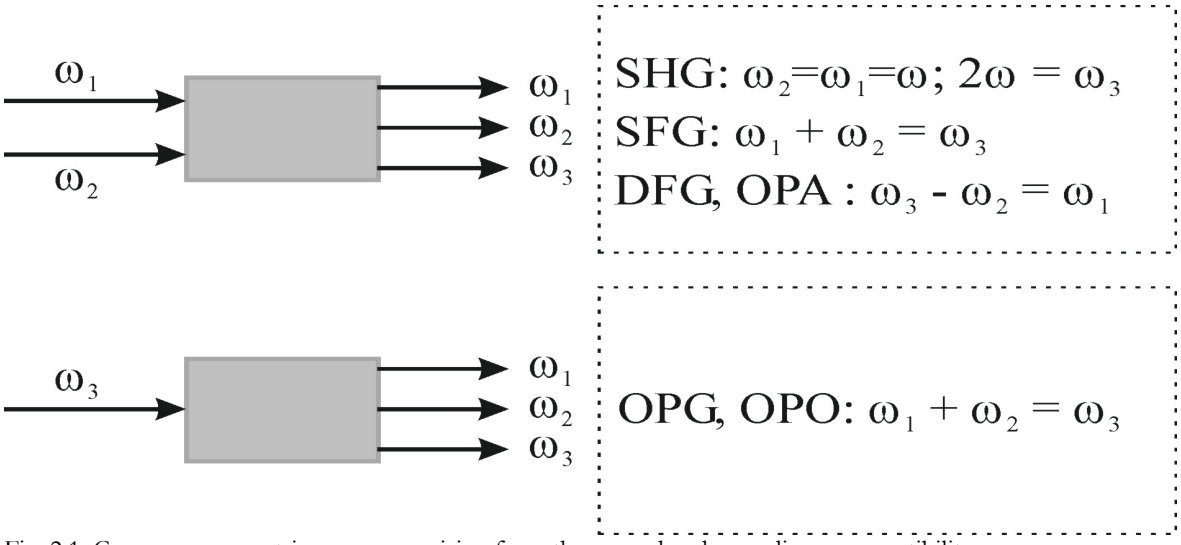

Fig. 2.1. Common parametric processes arising from the second-order nonlinear susceptibility.

$\chi^{(2)}$, generate a signal and an idler at lower frequencies. This is commonly called optical parametric generation (OPG) and can be referred to as parametric down conversion. If we

then enclose the nonlinear medium in a cavity, it will act as an optical parametric oscillator (OPO), where either the signal or the idler is resonant or both. When two waves are incident, the list of the nonlinear processes gets longer: second harmonic generation (SHG), optical rectification, sum-frequency generation (SFG), difference frequency generation (DFG), and optical parametric amplification (OPA). It is also possible to change the refractive index for an incident photon by applying an external DC-field, which is referred to as the electro-optic effect. In Fig. 2.1, a collection of nonlinear processes are depicted.

2.3.1 Second Harmonic Generation and Frequency Mixing

The simplest form of a nonlinear process is the generation of the second harmonic, and it was also the first one to be observed.[2] It basically takes two pump photons of the same frequency, ω, and adds their energy so it becomes: $\omega_{SH} = \omega + \omega = 2\omega$. In this case, where two fields have the same frequency and amplitude, the coupled wave equations (2.10) can be reduced to only two coupled equations:

$$\begin{aligned} \frac{\partial E_{\omega}}{\partial x} &= \frac{i\omega}{n_{\omega} c} d_{eff} E_{2\omega} E_{\omega}^{*} \exp[i\Delta k x], \\ \frac{\partial E_{2\omega}}{\partial x} &= \frac{i\omega}{n_{2\omega} c} d_{eff} E_{\omega} E_{\omega} \exp[-i\Delta k x], \end{aligned} \tag{2.11}$$

where now the phase mismatch is $\Delta k = k_{2\omega} - 2k_{\omega}$ and the degeneracy factor, K, has been given appropriate values. In the limit of no pump depletion, $\partial E_{\omega}/\partial x = 0$, and with the initial condition $E_{2\omega}(0) = 0$ and employing plane waves, the second equation in (2.11) can be integrated over the nonlinear crystal length to become:

$$I_{2\omega}(L) = \frac{\varepsilon_0 n_{2\omega} c}{2} \left| E_{2\omega} \right|^2 = \ldots = \frac{2\omega^2 d_{eff}^2 L^2 I_{\omega}^2}{\varepsilon_0 n_{\omega}^2 n_{2\omega} c^3} sinc^2\left[\frac{\Delta k L}{2} \right], \tag{2.12}$$

where I_{ω} is the intensity of the pump wave, L is the length of the nonlinear interaction, and n_{ω} and $n_{2\omega}$ are the refractive indices of the fundamental beam and the second harmonic, respectively. The function $sinc(\zeta) \equiv sin(\zeta)/\zeta$. This is, thus, valid for a plane wave and loosely focused beam. In the case of pump depletion, the above two coupled wave equations can be calculated analytically.[7,10] Moreover, for real-world laser beams having a Gaussian beam profile, it has been shown that the SHG efficiency is dependent on the Rayleigh length of the laser beam and the optical path length inside the crystal.[11]

The sinc-function in equation (2.12) determines the conversion efficiency of the process, and when this factor goes to 0.5, which occurs when $\Delta kL/2 = 0.4429\pi$, the spectral full-width at half maximum (FWHM) can be found. Expanding Δk in a Taylor series as a function of wavelength and neglecting higher order terms, the FWHM spectral bandwidth then becomes:[12]

$$\Delta\lambda = \frac{0.4429\lambda}{L} \left| \frac{n_{2\omega} - n_{\omega}}{\lambda} - \frac{\partial n_{\omega}}{\partial \lambda} - \frac{1}{2} \frac{\partial n_{2\omega}}{\partial \lambda} \right|^{-1}, \tag{2.13}$$

where λ is the fundamental wavelength and the derivatives are the group-velocity mismatch (GVM) between the fundamental and the second-harmonic waves, respectively.

2.3.2 Optical Parametric Generation

Consider a pump beam with high intensity that is incident on a suitable nonlinear crystal. In the photon picture, the pump photon (ω_p) will probably split spontaneously into a signal (ω_s) of higher frequency and an idler (ω_i) of lower frequency. If the process also is phase-matched the generated signal and idler can be amplified to a level at which the fluorescence is detectable.[4] This is the optical parametric generation process mentioned earlier and it is also called parametric superfluoresence. It is common to denote the signal's frequency range as $\omega_p > \omega_s > \omega_p/2$, and the idler's frequency range as $\omega_p/2 > \omega_i > 0$. By solving the wave equations (2.10), and assuming negligible pump depletion, the single pass power gain G can be calculated to be:[13,14]

$$G = \Gamma^2 L^2 \frac{\sinh\left[\sqrt{\Gamma^2 - \frac{\Delta k^2}{4}}L\right]}{\left(\Gamma^2 - \frac{\Delta k^2}{4}\right)L^2}, \tag{2.14}$$

where $\Delta k = k_p - k_i - k_s$, L is the interaction length, and Γ is the parametric gain factor given by:

$$\Gamma^2 = \frac{2\omega_s \omega_i d_{eff}^2 I_p}{\varepsilon_0 n_p n_s n_i c^3}, \tag{2.15}$$

The spectral power distribution can be calculated by integrating the function G over the angular distribution of the generated signal (or idler). The angular distribution of the fluorescence is dependent on the pump power characteristics and the phase-mismatch, which effects the spectral bandwidth of the signal and the idler.[13] In the case of a collimated pump beam, and assuming that the angular spread of the signals and the idlers are small, then equation (2.14) gives the spectral power distribution directly.[V] As mentioned above, it is common to express the spectral bandwidth at FWHM, and this can be done by expanding the phase-mismatch, Δk, in a Taylor series with respect to frequency. To the first-order in the high-gain non-degenerate OPG limit, this would yield:[15]

$$\Delta\upsilon \cong \frac{2(\ln 2)^{1/2}}{\pi}\left(\frac{\Gamma}{L}\right)^{1/2} \frac{1}{\left|\frac{\partial k_s}{\partial \omega_s} - \frac{\partial k_i}{\partial \omega_i}\right|}, \tag{2.16}$$

where the two terms within the absolute bracket express the group velocity mismatch (GVM) between the signal and the idler. So, when operating the OPG far away from degeneracy the GVM will be large and the spectral bandwidth small. Large spectral bandwidths can be expected to appear close to degeneracy ($\omega_s \approx \omega_i$). However, at this point, the GVM is close to zero and a second-order dispersion term is needed in order to describe the spectral bandwidth properly. Thus, the bandwidth at degeneracy for an OPG can be approximated by:[16]

$$\Delta\upsilon \cong \frac{2(\ln 2)^{1/4}}{\pi}\left(\frac{\Gamma}{L}\right)^{1/4}\frac{1}{\left|\frac{\partial^2 k_s}{\partial\omega_s^2}+\frac{\partial^2 k_i}{\partial\omega_i^2}\right|}, \tag{2.17}$$

where the terms $\partial^2 k_j / \partial\omega_j^2$ (j = s, i) are the group-velocity dispersion (GVD) for the signal and the idler, respectively. Consequently, nonlinear materials which have low GVD will generate large bandwidths; an important application for this would be, for example, for amplification of ultrashort pulses.[16]

2.3.3 Optical Parametric Oscillator

If spectral refinement is wanted of the OPG output, the nonlinear crystal can be enclosed in a cavity and, when the parametric gain is higher than the losses of the cavity, the signal (and/or the idler) starts to oscillate. Thus, optical parametric oscillation is achieved.

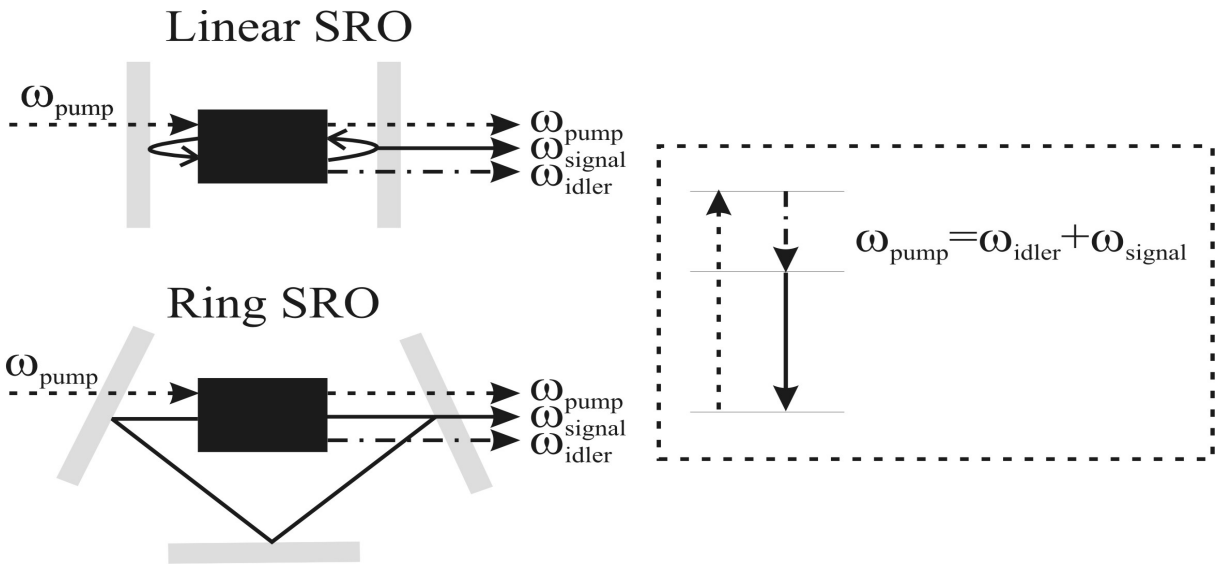

Fig. 2.2. Singly-resonant OPOs in a linear and a ring configuration. To the right is an energy diagram of an OPO process, equivalent for OPG.

There are different ways to operate an OPO. If one field in the OPO is resonant, it is called singly-resonant (SRO) and in the case of a doubly-resonant OPO (DRO), both the signal and the idler are resonant in the cavity. It is also possible to have the pump reflected back into the cavity in a double-pass configuration. An important condition for the OPO to work is that the generated signals and idlers must correspond to two longitudinal modes of the cavity, similar to that of a laser cavity.[17] However, in the case of DRO, this causes instabilities of the output when small changes in the cavity length occurs, due to temperature fluctuations or mechanical vibrations. The reason is that the signal and the idler shift in frequency in the same direction as the cavity and this will cause the energy conservation to fail and special steps need to be taken in order to stabilize the cavity.[18] SRO is the most frequently used case, since it does not need external stabilization measures and it is practical in the sense of cavity design. Depending on the application, various cavity designs can be deployed, such as linear and ring cavities,[2,19] which are most common. In this work, mainly SROs with linear and ring

cavities have been investigated, seen in Fig. 2.2. The main difference between an OPO and a laser is that an OPO does not store energy in an excited level and is inherently unidirectional.

To operate an OPO, it is necessary to focus the pump beam into the cavity. Usually, laser beams have approximately a Gaussian profile,[17] and this needs to be taken into account when calculating the parametric gain. Adding the pump's sptatial characteristics to the plane wave approximated, equation (2.15) it will have the following form:

$$\Gamma^2_{Gaussian} = \Gamma^2_{plain} \frac{n_p}{\lambda_p} \frac{A}{L} h_m(B, \xi), \tag{2.18}$$

where $h_m(B,\xi)$ is the Boyd-Kleinman factor.[10] The first argument in h_m is the double refraction parameter, B, that takes Poynting vector walk-off (more on walk-off in Chapter 3) into account, and $\xi = L/b$, where L is the crystal length and b is the confocal parameter, i.e., twice the Rayleigh length.[17] Finally, $A = \pi(w_0)^2$ is the effective area and w_0 is the Gaussian radius at the e^{-2}-intensity. In the limit of loose focusing ($\xi < 1$) and no walk-off ($B = 0$), which is the case for the OPOs in this work, the h_m-factor becomes $\xi = L/b = L\lambda_p / (2\pi w_0^2 n_p)$. As a result, equation (2.15) is restored and the plane wave approximation can then be said to be valid.

OPOs can be very efficient. For pulsed SROs, it has been shown theoretically that a conversion efficiency of 100 % is possible in the plane wave approximation; however, with Gaussian beams, the theoretical conversion is slightly over 70 %.[20] The explanation for this is that the wings of the Gaussian beam is below threshold and do not participate in the frequency conversion process. To obtain a measure on how efficient parametric process is would be to calculate the ratio of the generated signal and idler powers over the incident pump power, i.e.:

$$\eta = \frac{P_s + P_i}{P_p(x = 0)}, \tag{2.19}$$

where P_j (j = s, i, p) is the power (or energy) of the signal, the idler, and the input pump, respectively. Equation (2.19) is, thus, the overall conversion efficiency. However, in some cases it is not possible to measure the idler power due to absorption in the nonlinear crystal or the cavity mirrors; then by measuring the pump depletion, it is possible to "reconstruct" the idler power through the so-called Manley-Rowe equations.[21] These equations originate from the coupled wave equations (2.10) and, after some manipulation, it yields:

$$\frac{1}{\omega_i}\frac{\partial I_i}{\partial x} = \frac{1}{\omega_s}\frac{\partial I_s}{\partial x} = -\frac{1}{\omega_p}\frac{\partial I_p}{\partial x}, \tag{2.20}$$

where I_j is the intensity of the three constituent waves. This equation states the photon number conservation and, for an OPO, it simply says that energy flows from the pump to the signal and the idler. Moreover, it is also possible to measure the efficiency as ratio between the number of generated photons over the amount of incident pump photons, which is referred to as quantum efficiency, $\eta_{quantum}$. In the case of mid-infrared or far-infrared wavelength generation, the $\eta_{quantum}$ can be higher than the overall efficiency, η.

There are different ways of spectrally tuning an OPO. The simplest form is by changing the temperature of the crystal, and, in doing so, the refractive index changes and, thus, the phase-matching conditions are affected.[3] Another way to extend the tuning range is by rotating the crystal or the whole cavity. However, in a SRO, the spectral bandwidth varies over a large range due to the dispersion properties of the nonlinear crystal and chosen the

pump wavelength, which is seen in equation (2.16). This equation, however, is not entirely correct for an OPO, since the cavity limits the angular spread of the resonant wave and acts as a spatial and spectral filter. This has been discussed in reference [22] and, according to that, the total spectral bandwidth for a linear OPO can be approximated by:

$$\Delta\upsilon_{tot} = \Delta\upsilon / \sqrt{N}, \tag{2.21}$$

where N is the total number of roundtrips for the signal (or idler) pulse in the cavity and $\Delta\nu$ can be replaced by either equation (2.16) or (2.17). Even though this decreases the available bandwidth, it is not enough for some spectroscopic applications, where very narrow linewidths are desired. It is then possible to further decrease the linewidth by deploying some optical elements inside the OPO cavity. For example, by inserting a birefringent etalon inside the cavity or by using a grating as an end mirror in a folded cavity.[22] In Chapter 4, I will further discuss different linewidth narrowing techniques.

2.3.4 Optical Parametric Amplification

When two fields at ω_p and ω_s are incident on a nonlinear crystal, they will interact and create an idler wave at $\omega_i = \omega_p - \omega_s$. In the case of a strong pump field, P_p, and a week signal, P_s, the ensuing interaction will lead to an amplification of the signal with preserved phase, while the idler will monotonically grow with a phase depending on both the pump and the signal.[7] Furthermore, the process of OPA is quite similar to that of DFG, as seen in Fig. 2.1; however, the magnitude of the signal (also called the seed) is much lower than that of the pump, whereas in the case of DFG both incident fields are approximately equal in magnitude. The amplification of an OPA is determined by the parametric gain as seen in equation (2.15). The expression for the amplified signal and idler, assuming a signal seed, are given by:[15,16]

$$\begin{aligned} I_s(L) &= I_s(0)[1+G], \\ I_i(L) &= I_s(0)\frac{\omega_i}{\omega_s}G, \end{aligned} \tag{2.22}$$

where G was given in equation (2.14) and $I_s(0)$ is the initial seed intensity. These expressions are valid for a nondepleted pump.

In order to amplify a signal, the gain material needs to support the spectral range of the seed. In the limit of large spectral bandwidth, which is present in femtosecond pulses, it is crucial that the amplifying mediums parametric fluorescence overlap or is broader than the seeds spectrum. The spectral bandwidths of OPA are also set by the GVM parameter and the parametric gain, which was earlier discussed in paragraph 2.3.2. In Chapter 5, the experimental results of ultrabroad bandwidth generation and the applications of this in an OPA are described in detail.

2.3.5 Cascaded Interactions

In quadratic media, it is common to observe sum-frequency mixing between the pump and the generated signal (idler) or between the signal and the idler. The occurrence of this kind of

non-phase matched cascaded effects through the $\chi^{(2)}$ is very likely when, for example, operating an OPG. The lowest order of cascaded effects is through the $\chi^{(2)}:\chi^{(2)}$ interaction and was discussed by Armstrong *et al*. already in 1962.[11] This is then a fourth rank tensor which involves four fields which adds an additional contribution to the total third order nonlinearity.[23] One reason for using a quadratic media for cascaded interaction instead of a pure $\chi^{(3)}$ material (such as a silica fiber), is that the effective third-order nonlinearity can become much higher when the phase-matching condition is properly chosen. For example, the intensity dependent refractive index and nonlinear phase-shift, which is proportional to the third order nonlinearity, can be mimicked through the interaction scheme:[15]

$$\left[\chi^{(3)}(-\omega;\omega,\omega,-\omega)\right]_{eff}=\chi^{(2)}(-\omega;2\omega,-\omega):\chi^{(2)}(-2\omega;\omega,\omega), \tag{2.23}$$

where the first and second terms to the right are the second-order susceptibilities present in equation (2.12) (identified as d_{eff}). By eliminating $E_{2\omega}$ in the equations (2.11), and integrating over the crystal length L, the cascaded interaction's contribution to the intensity dependent refractive index can be approximated by:[24]

$$n_2^{eff}=-\frac{4\pi}{c\varepsilon_0}\frac{L}{\lambda}\frac{Re\left[\chi^{(3)}(-\omega;\omega,\omega,-\omega)\right]_{eff}}{n_{2\omega}n_{\omega}^2}\frac{1}{\Delta kL}, \tag{2.24}$$

This approximation is only valid for small intensity variations and all the variables are given in subsection 2.3.1. The result is connected to the optical Kerr effect and is described as a modulation of the refractive index: $n=n_0+n_2^{eff}I_{\omega}$.[15] It should be noted that the effective nonlinear index can be either positive or negative depending on the sign of the phase mismatch Δk. The imaginary part of equation (2.23) is the losses of the fundamental beam, i.e., it undergoes frequency conversion to the SH-beam. This Kerr-like behaviour can be used for mode-locking solid-state lasers; conceptually, the phase of the fundamental beam is modulated as described above and, depending on the sign of the phase-mismatch, the beam will be defocused or focused.[25,26] This then works, from a physical point a view, as the Kerr lens mode-locked Ti:sapphire laser, which was first discovered by Sibbett *et al*.[27]

However, the cascaded interaction is not limited to the emulation of Kerr-like media. It have been used in various areas ranging from dispersion compensation in optical fiber networks,[28] to allowing accurate measurements of the *real* third-order susceptiblity.[29] In Chapter 4 the cascaded interaction due to a parametric gain grating, is observed and explained.

Chapter 3

Phase-matching

For efficient parametric interaction, the induced polarizations and their respective waves need to be phase matched. If perfect phase-matching occurs ($\Delta k = 0$) then the parametric process will be highly efficient. However, perfect phase-matching is difficult to achieve, since the refractive index is a function of the frequency. In the case of SHG, with E_ω and $E_{2\omega}$ polarized in the same direction, the condition that n_ω should be equal to $n_{2\omega}$ is, generally, not true and, as a consequence, the SHG conversion efficiency will be low, as was evident for Franken *et al.* back in 1962.[2] Nevertheless, most of the second-order nonlinear materials used today are birefringent (except GaAs), which means that, depending on the polarization of the optical field, it will encounter different refractive indices. This property can be utilized for so called birefringent phase-matching (BPM). Another way is to manipulate the nonlinear coefficient in a periodic manner, so that all the waves can be polarized in the same direction and their phases are reset at optimum propagation length. This is called quasi-phase matching (QPM). In this chapter a short description of phase-matching techniques will be covered and an overview of the nonlinear crystals used in this thesis will be given.

3.1 Birefringent Phase-matching

In the case of SHG, equation (2.12) describes the generated SH and it can be seen that the intensity at 2ω will oscillate over the crystal length if the phase-mismatch, Δk, is not zero:

$$\Delta k = k_{2\omega} - 2k_\omega = \frac{2\omega(n_{2\omega} - n_\omega)}{c} \neq 0, \tag{3.1}$$

The interpretation of equation (3.1) is that the driving polarisation propagates at a phase velocity of $v_{phase}^{\omega} = (2k_\omega/\omega)^{-1}$, whereas the generated wave, $E_{2\omega}$, has the phase velocity of $v_{phase}^{2\omega} = (2k_{2\omega}/\omega)^{-1}$. Hence, after a distance called the coherence length, the driving polarisation and the generated beam have drifted out of phase by π. At this point backconversion starts and the energy will flow back into the fundamental beam again. The coherence length is defined as the ratio of π over the phase-mismatch and, inserting into equation (3.1), yields:

$$L_c = \left|\frac{\pi}{\Delta k}\right| = \left|\frac{\lambda}{4(n_{2\omega} - n_\omega)}\right|, \tag{3.2}$$

Franken *et al*.[2] used a fundamental wavelength of 694 nm and the coherence length in quartz glass can be calculated to be approximately 10 μm. This is not a sufficient length for high conversion efficiencies; however, by utilizing the natural birefringence of nonlinear materials, the length can be extended.

There are two types of BPM: type-I is when two fields at ω_1 and ω_2 will have the same polarization, while the third field, at ω_3, is polarized orthogonally with respect to the first two; type-II, on the other hand, will have the two fields at ω_1 and ω_2 orthogonal. In a uniaxial material, the principal optics axis is commonly along the crystal's z-axis (symmetry axis) and the principal refractive indices are then $n_x = n_y = n_o$ and $n_z = n_e$, which are called the ordinary and the extraordinary refractive indices, respectively. For a positive uniaxial crystal, $n_o < n_e$, and the opposite is the case for a negative uniaxial crystal. For a wavevector propagating at an angle of θ to the principal optics axis the extraordinary wave experiences a refractive index given by:

$$\frac{1}{[n_e(\theta)]^2} = \frac{\cos^2\theta}{[n_o]^2} + \frac{\sin^2\theta}{[n_e]^2}, \tag{3.3}$$

By choosing the right angle the SH process can be phase-matched. In Fig. 3.1, the refractive indices of n_o, n_e and $n_e(\theta)$ are depicted for an arbitrary negative uniaxial crystal tighter with the illustration of an appropriate phase-matching for SHG. The 2ω frequency is generated at

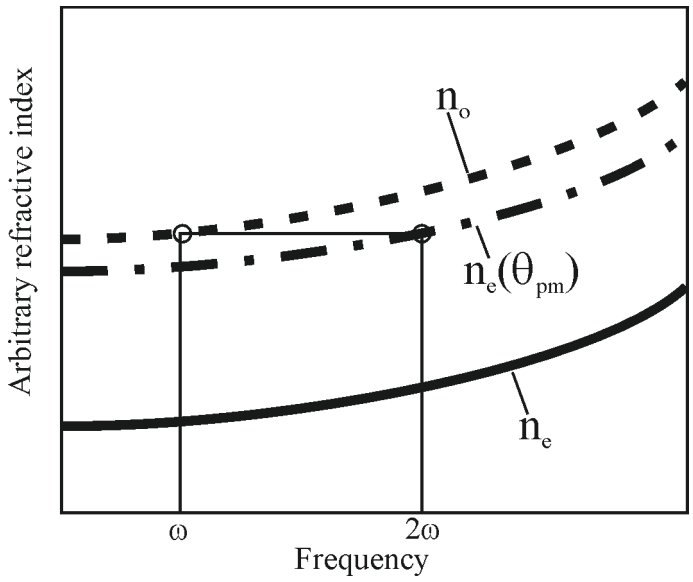

Fig. 3.1. Refractive indices n_o, n_e and $n_e(\theta)$, for an arbitrary negative uniaxial and the phase-matching condition for SHG at an arbitrary angle θ_{pm}.

the extraordinary polarization direction, while the fundamental (ω) polarization is in the ordinary one. This is called a type-I ooe process, referring to the two **o**rdinary waves at ω and the **e**xtraordinary wave at 2ω. The wavevector, k_ω, propagates at and angle of θ_{pm} to the principal optics axis of the crystal, whereas the extraordinary wave, $k_{2\omega}$, will deviate slightly from this direction. The reason for this deviation is that the power flow for a beam is normal to its index ellipsoid (or sphere) and is governed by the Poynting vector;[30] since the index ellipsoid of the extraordinary beam, $n_e(\theta)$, differs from the spherical ordinary beam, this will cause a skew in the propagation and cause the extraordinary beam to walk-off by an angle ρ, which is given by:

$$tan\rho = -\frac{1}{n_e(\theta)}\frac{d\, n_e(\theta)}{d\theta}, \tag{3.4}$$

This limits the interaction length of the ordinary and the extraordinary beams which will result in an astigmatic beam profile of the generated beam and a reduced efficiency. The inverse of Additionally, this also limits the ability to focus tightly, since a smaller beam waist separates faster than a larger one. Walk-off, obviously, does not happen when $\theta = 90°$, and this case is commonly called noncritical phase-matching (NCPM).

Since the phase-matching conditions determine the angle of propagation, it will not necessarily be in the direction of the highest effective nonlinear tensor element.[6] In addition, BPM is also very sensitive to angular deviations of the pump wave(s), which is called the acceptance angle $\Delta\theta = \theta - \theta_{pm}$, and is inversely proportional to equation (3.4), i.e., $\Delta\theta \propto \left(d\, n_e(\theta)/d\theta\right)^{-1}$. Here, θ_{pm} is the angle of perfect phase-matching, and θ is the deviation from that. The largest $\Delta\theta$ is found, once again, for NCPM, when the angle $\theta_{pm} = 90°$.

These restrictions (walk-off, small d_{eff} and $\Delta\theta$) of the BPM then limits the possible wavelengths for which adequate phasematching conditions and good conversion efficiencies can be achieved. However, it should be noted that in order to reach certain extremes in terms of wavelengths, such as the deep-UV, this is the only phase-matching technique available.

3.2 Quasi-Phase-matching

It is always desirable to isolate and to access one of the largest terms in equation (2.4). In BPM, this is not possible, so another phase-matching technique must be utilized. The largest diagonal term can be used if all the waves in a parametric process are polarized in the same direction. However, as seen above, the coherence length, L_c, sets the limits for when backconversion starts. So, if we reset the phase at L_c by adding a π phase shift to $\Delta k L_c$, the power flow will continue in the preferred direction. The question is how a π phase shift can be introduced in the coupled wave equations (2.10) at every coherence length? The answer is by reversing the sign of the d_{ij} tensor, i.e. by introducing the term: $-d_{ij} = d_{ij}e^{i\pi}$. This technique is called quasi-phase-matching (QPM) and was actually already proposed in the 1960's.[11,31] Practically, this can be done in ferroelectric crystals by modulating the spontaneous polaristaion, P, of the material. More on this in a later section.

Shown in Figs. 3.2 is the process of SHG for four different cases of Δk, using equation (2.12), as a function of L_c. In the trivial case of perfect phasematching, $\Delta k = 0$, the SHG power increases quadratically with the crystal length, shown as curve (i) in the Fig. 3.2 (a). For the non-phase-matched case, $\Delta k \neq 0$, the SHG power fluctuates with a period of $2L_c$ and the generated wave will not grow over distance, seen as curve (iii). However, if we make use of the sign reversal described above at every coherence length, the energy will continue to flow from the fundamental beam into the second-harmonic beam in a continuous manner, as seen in curve (ii). This is called first-order QPM. Depicted in Fig. 3.2 (b) is also the case for third-order QPM, shown as curve (iv), which means that the sign of d_{ij} is reversed every third coherence length. The arrows in the figures indicate the direction of d_{ij}, which is inverted by 180° at every first and third coherence lengths, respectively.

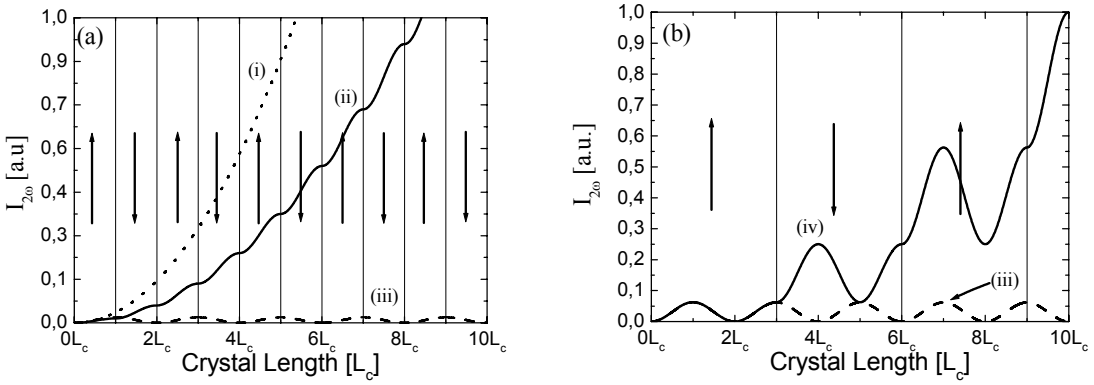

Figs. 3.2. Second harmonic output power for four different cases of Δk. (a): Dotted curve - $\Delta k = 0$, perfect phase-matching. Solid curve - first-order QPM. Dash curve - $\Delta k \neq 0$, non-phase-matched. (b): Solid curve - third-order QPM. Dash curve - non-phase-matched case.

The mathematical approach to QPM consists of expressing it in terms of a Fourier series by describing the periodic inversion of d_{ij} as:

$$g(x) = \sum_{m=-\infty}^{m=\infty} G_m \, exp(iK_m x), \tag{3.5}$$

where $g(x) \equiv d(z)/d_{ij}$ is a normalised rectangular function with the values of ± 1 and a period of $\Lambda = 2L_c$.[12] K_m is the grating wave vector with the direction along the x-axis (same as the propagating fields) and is given by:

$$K_m = \frac{2\pi m}{\Lambda}, \tag{3.6}$$

By inserting the Fourier series of equation (3.5) into the second equation of the coupled wave equations (2.11), and assuming an arbitrary d_{ij} and the m:th order, the phase-matching conditions will change to:[12]

$$E_{2\omega} = \frac{i\,\omega\,E_\omega^2}{n_{2\omega}\,c} d_{ij} \int_0^L G_m \, exp\left[i\left(K_m - \Delta k'\right)x\right] dx\,, \tag{3.7}$$

Here, the new phase-mismatch condition for SHG is given by $\Delta k = k_{2\omega} - 2k_\omega - K_m$ and the conversion can only be efficient when $\Delta k \approx 0$. In the series expansion of equation (3.5), it is only one term that fulfils this condition and, at the same time, the effective nonlinear coefficient is reduced to $d_{eff} = G_m d_{ij}$. For a rectangular structure, like in this case, the Fourier component G_m is given by:

$$G_m = \frac{2}{\pi m} sin\left(\pi m \frac{L_p}{\Lambda}\right), \tag{3.8}$$

where L_p is the length of the grating for which sign of d_{ij} is positive. For optimum QPM, m should be equal to one and the argument of the sine-function should be $\pi/2$. Thus, L_p should correspond to the coherence length L_c. This results in a value for the effective coefficient of

$d_{eff} = 2d_{ij}/\pi$. With this correction term inserted into equation (2.12), the output characteristics of the SHG will have a smoother evolution. This addition phase term can be used to tailor the output from a quasi-phase-matched crystal; seen in Fig. 3.3 is the signal and the idler wavelengths as a function of grating period for three different pump wavelengths.

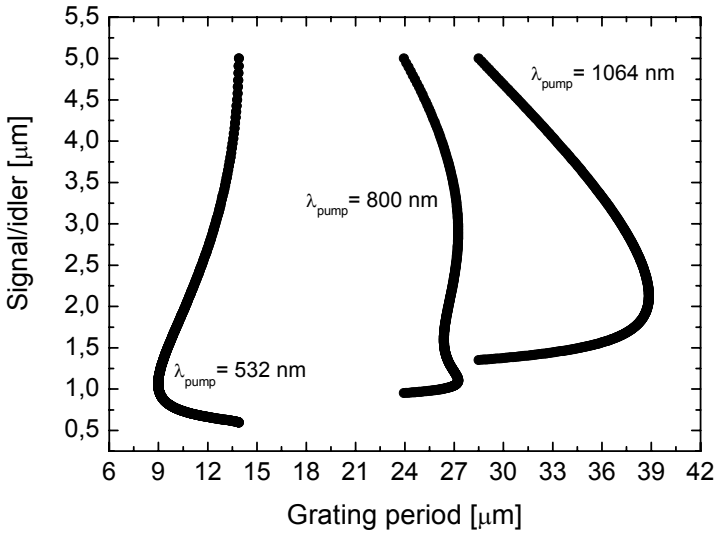

Fig. 3.3. Phase-matching curves for $KTiOPO_4$ with corresponding grating period for the pump wavelengths: λ_p = 532 nm, 800 nm, and 1064 nm.

Even though QPM imposes a reduction of the effective nonlinear coefficient, the advantages of QPM are several. First of all, all of the waves can be polarized in the same direction and parallel to one of the principal axes, e.g., the z-axis. As a consequence, there will be no Poynting vector walk-off. Furthermore, phase-matching can be achieved at any wavelength within the transparency range of the crystal, since the period Λ is engineerable, and provide phase-matching even for nonlinear materials which lack adequate birefringence. It also becomes possible to isolate the largest d_{ij} in the particular material used, were often i = j. For example, for $LiNbO_3$, $LiTaO_3$, $KNbO_3$, and for $KTiOPO_4$ and its isomorphs, the d_{33} has the largest nonlinear coefficient.[15] The interpretation of the d_{33} coefficient is that the interacting waves have to be polarized in the z-direction of the crystal. This supports the condition of low-threshold and results in highly efficient parametric devices, since the parametric gain will be higher (see equation (2.15)) and longer crystals can be used. Thus, it becomes feasible to use moderate pump powers emitted by CW lasers.

However, the restriction of QPM is that the grating of the nonlinear material needs to be fabricated in a periodic manner. Different techniques for achieving QPM in various dielectrics have been earlier studied, for example: rotating quartz wafers at periodic intervals,[31] applying a periodic electric field over liquid nitrobenzene,[33] growing of orientation-patterned GaAs in molecular-beam epitaxy, [33,34] etc. In the case of a ferroelectric material, the most widely used fabrication technique is electric-field poling.[35-37] To implement the periodic domain inversion, electrodes are deposited over one of the polar surfaces of the crystal by lithographic patterning. Then a high voltage is applied over the sample to reverse the sign of the spontaneous polarization of the material at periodic intervals. The grating periods can normally be fabricated in the range from a sub μm to hundreds of μm.

3.3 Nonlinear Optical Crystals

Below, I will give a short overview of the most common nonlinear crystals that can be utilized to cover the spectral range from the mid-IR to the deep UV by using appropriate pump frequencies.

PPKTP have a central role in this thesis, since we have the possibility to fabricate these samples at KTH, lending us the opportunity to fabricate any grating period of choice. The optical properties of KTP are very good: it possesses a high nonlinear coefficient of $d_{33} = 16.9$ pm/V,[38] it is transparent from 0.365 μm to approximately 4.3 μm,[39] and it has a high damage threshold, >900 MW/cm^2 of 5 ns pulses at 1 μm.[40] It can be used at room temperature and will withstand high intensities throughout its transparency window without showing any damage. For frequency conversion in the visible, KTP is the preferred choice. The KTP samples used in this work were made from flux-grown KTP and the periodic structures were fabricated by electric-field poling according to the technology developed by Karlsson *et al*.[37] In order to "write" the periodic structure on a KTP crystal, a photolithographic mask is constructed. Conventional masks have single-grating period, typically ranging from 3.4 μm to 36 μm for first-order QPM applications, which is patterned over the whole length of the sample.[35-37] The properties of PPKTP have been studied extensively in several earlier Doctorial thesis at KTH and, for more information regarding the poling technology and the KTP material and its isomorphs, see references [41-43]. In recent years, parallel with the improvement of e-beam and UV-laser lithography technologies, novel grating structures have appeared, such as: multigrating structures, Fibonacci-sequenced gratings, and aperiodic (i.e. chirped) gratings.[44-46] Today, there are several reliable and efficient ferroelectric nonlinear materials such as $LiNbO_3$, $LiTaO_3$, $KTiOPO_4$, $RbTiOPO_4$ and $RbTiOAsO_4$, which can by poled in similar fashion.

Periodically poled congruent $LiNbO_3$ (PPCLN) is by far the most often used QPM material today, it has good optical properties with a coefficient of $d_{33} = 27.2$ pm/V and it is transparent from approximately 0.35 to 5.4 μm. However, due to its high coercive field, the samples have been limited to ~1 mm thickness and its ability to withstand high pump intensities is lower than for KTP. A well-known fact is that the photorefractive effect degrades the crystal's performance, especially in the visible range, and it must be kept in an oven at elevated temperatures. In the case of congruent $LiTaO_3$ (CLT), it shows similar properties as those of CLN; however, it is transparent all the way down to ~0.28 μm. Measures have been taken in order to circumvent the devastating degradation of LN and LT by doping them with magnesium oxide (MgO). However, the growth techniques for these doped materials are not yet fully matured.

There are several types of borate-based crystals, such as β-BaB2O (BBO), LiB3O5 (LBO), $CsLiB_6O_{10}$ (CLBO), KBe2BO3F2 (KBBF), and BiB3O6 (BIBO).[47,48,49] The first three materials are relatively old and are not ferroelectric; however, they have been extensively used in many applications, since they all have very high damage thresholds and are transparent down into the deep UV.[47] For example, BBO has a transparency range from 185 nm to 2600 nm. A drawback of these materials is their relatively low nonlinear coefficient, typically being in the range of between 0.5 to 3 pm/V. The crystals are birefringent and are commonly birefringently phase-matched; this, of course, sets strict limits on the angular acceptance bandwidth and imposes walk-off.[15] Nevertheless, in order to reach UV wavelengths these crystals are the preferred choice, with applications in photolithography, micromachining, etc.[50]

For mid-IR generation another, type of crystal composition is used and these materials are not oxide based. The common ones here are the chalcopyrite crystals: $ZnGeP_2$ (ZGP),

$AgGaSe_2$, and $CdGeAs_2$.[51-53] All of them have extremely high figures of merit (FOM), which is defined as $FOM \equiv d_{eff}^2 / n^3$. The FOM is ~190, ~60, and ~1200, respectively, for the chalcopyrite crystals above; compared to KTP's FOM ~46. The ZGP crystal has an effective transparency range between 2 μm and 8 μm and a coefficient of $d_{eff} = 75$ pm/V. The recent improvements in crystal growth techniques enables the fabrication of large samples, which can be used for high-power applications in the mid-IR spectral range.[54] The drawback, however, is that a >2 μm source is needed to pump the ZGP and that the availability ot the material is limited. The $AgGaSe_2$ and $CdGeAs_2$ crystals are mostly suited for frequency doubling of the CO_2-laser and for parametric applications in the 8-12 μm and 6-20 μm ranges, respectively.[52,55] These crystals also rely on BPM. Moreover, new growth technologies have enabled the fabrication of orientation-patterned GaAs (OP-GaAs).[34] This semiconducting crystal relies on QPM and different periods can be fabricated, as for the ferroelectric materials; however, OP-GaAs is so far limited to around 0.5 mm apertures.

In published work by the candidate, periodically poled $KTiOPO_4$ (PPKTP), β-BaB_2O_4 (BBO) and $ZnGeP_2$ (ZGP) have been used in order to cover the spectral range from the UV to the mid-IR.

Chapter 4

Optical Parametric Oscillators

Ever since the 1960s, parametric devices have continuously been developed to become more and more efficient, while extending the tunability capabilities. These progresses have been the subject of several reviews since then.[14,56,57] The advantage with OPOs is that they are capable of providing tunable output-wavelengths that are unobtainable with conventional solid-state lasers, which is highly desirable in spectroscopic and remote-sensing applications. However, limitations associated with the BPM OPO hampered some of the applications, due to the Poynting vector walk-off and low effective nonlinear coefficient. With the development of electric-field poling for ferreoelectric materials, the above restrictions were circumvented and it became possible to construct QPM-based OPOs of practical significance. The QPM OPOs, compared to a BPM OPO, have a much reduced oscillation threshold and are highly efficient, which enables operation of these OPOs at moderate pump powers. The spectral range of these QPM materials is now only limited by their transparency and the choice of pump wavelength, since it is possible to engineer the phase matching conditions in a controlled form.

PPKTP has proven particularly efficient, reliable, and practical when utilized in singly-resonant optical parametric oscillators (SROs), as it can be operated at room temperature and will withstand high pump intensities without showing damage.

4.1 Novel Linewidth Narrowing Techniques

The simplest configuration for a nanosecond QPM OPO is by operating it collinearly, see Fig. 2.2, where the pump, the signal, and the idler beams are co-propagating. Wavelength tuning can be achieved by adjusting the temperature of the QPM crystal,[58] in the same manner as for BPM OPOs.[3] One way of extending the tuning range in collinear OPOs is by fabricating multiple-grating sections on a single chip of $LiNbO_3$ or by using fan-out period QPM structures.[44,59] If a single-periodicity QPM structure is employed in an OPO, then the tuning range can be enhanced in a rather simple way by using non-collinear configurations. Several non-collinear OPO geometries have been demonstrated, for example: (i), by rotating the cavity axis in a PPKTP OPO;[60] (ii), by rotating the crystal in a monolithic PPLN, KTP and PPKTP OPO;[61-63] (iii), by adjusting the pump angle in a Bessel-beam pumped OPO;[64] or (iv), by accousto-optically change the pump angle when launching it into the OPO.[65] Noncollinear OPO geometry possesses an additional advantage of easily separation of the signal-, the idler-, and the pump-beams, which simplifies the OPO-seeding arrangements. Angular separation of the interacting waves also reduces backconversion at high pumping intensities compared to collinear OPOs.[66]

However, in linear SRO configuration, the spectral bandwidth is inherently broad and not suitable for many spectroscopic applications, where narrow linewidths are needed. The requirements can be estimated by the properties of a typical rotational-vibrational transition,

which has a peak-to-peak distance of the order of 100 GHz and a linewidth of a few GHz. The standard approaches to decrease the bandwidth of an SRO are by introducing a dispersive element in the cavity or injection-seeding it with a narrowband source.[67] A drawback in the latter case is that it will only transfer the issue of narrowing, since the seed source itself needs to be stable and narrow in frequency. In the former case, it is common to use intra-cavity dispersive elements, such as diffraction gratings and birefringent filters.[22] Regrettably, these elements increase the cavity losses and, therefore, require increased pump power. Using dispersive elements, however, lends wavelength versatility to the OPO design, which can be adapted for any wavelength reached by the OPO. In the following sections I will describe some novel OPO designs made in order to achieve linewidth narrowing in PPKTP SROs.

4.1.1 Idler Resonant Optical Parametric Oscillator

The spectral and spatial properties of an OPO's output are dependent on the material dispersion and the angular dispersion of the interacting waves in the parametric gain medium, as well as, the properties of the pump beam.[13,14] In general, for the nondegenerate OPO, the angular dispersion is different for the signal and the idler waves. This property can be utilized in order to modify the spectral bandwidth and the spatial properties of the OPO. In the work described in article [I], we showed that larger angular dispersion of the idler wave allows the generation of more narrow spectral bandwidths and higher spatial-quality beams in an idler-resonant OPO as compared to the signal-resonant OPO having the same pump and cavity conditions. Here, we define the angular dispersion as $\partial\theta/\partial\nu$, where ν and θ are the frequency and the angle of the parametric wave with respect to the pump, respectively. Moreover, in the case of idler-resonant OPO, the resulting larger diffraction contributed to an additional limiting of the spectral bandwidth and an increase in the spatial quality of the cavity beam.

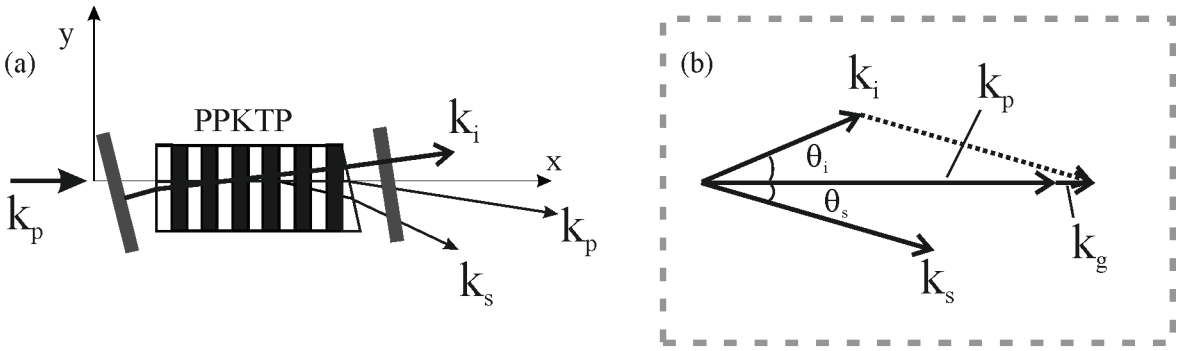

Fig. 4.1. (a): the experimental setup of the SRO. (b): the corresponding phase-matching conditions depicted with wavevectors inside the crystal.

In Fig. 4.1 (a), the experimental setup of the SRO is shown. The QPM period of the PPKTP crystal is $\Lambda = 9.1$ μm and it was enclosed by two flat cavity mirrors. Two sets of cavity mirrors were used in order to either resonate the signal or the idler, while both sets transmitted the pump at 532 nm. One of the input surfaces of the crystal was wedged in order to prevent parasitic parametric oscillation. The physical length of the OPO cavity was kept constant and equal to 14 mm throughout the experiments. The pump source was a Q-switched frequency-doubled Nd:YAG pump laser that was operated at 20 Hz and which generated 5 ns-long pulses in a non-diffraction limited beam with an $M^2 = 9$. For more detailed information regarding the setup, see article [I].

Graphically illustrated in Fig. 4.1 (b) are the wavevectors for the noncollinear case when the pump wave vector, k_p, is parallel to the QPM grating vector, $K_g = 2\pi/\Lambda$, inside the crystal. The angle θ_i between the resonated wave and the pump was varied by turning the cavity mirrors. The idler and the signal angles, θ_i and θ_s, inside the crystal can be derived from the phase-matching conditions in a way that is analogous to reference [68]:

$$k_p - k_s \cos\theta_s - k_i \cos\theta_i - K_g = 0, \tag{4.1}$$

$$k_s \sin\theta_s + k_i \sin\theta_i = 0, \tag{4.2}$$

where k_i, k_s, and k_p are the idler, the signal, and the pump wave vectors, respectively. The temperature tuning characteristics are shown in Fig. 4.2 (a) for the collinear case. The OPO could be tuned from 962 nm down to 908 nm and from 1189 nm up to 1284 nm for the signal and the idler, respectively, by changing the PPKTP temperature from T = 20°C to 100°C. In the case of angle tuning the OPO, the signal was tuned between 962 nm and 898 nm for the internal signal angles θ_s between 0 mrad and 26 mrad at room temperature; whereas the idler was tuned in the same way between 1189 nm and 1305 nm. The internal angle of the conjugate idler wave then changed between 0 mrad and 41 mrad, as seen in Fig. 4.2 (b). The phase-matching conditions, however theoretically, allow the generation of two symmetric signal-idler pairs corresponding to the non-collinear angles $\pm\theta_s$ ($\pm\theta_i$). Even so, in our experiments, only one signal-idler pair was observed in all of the non-collinear OPO

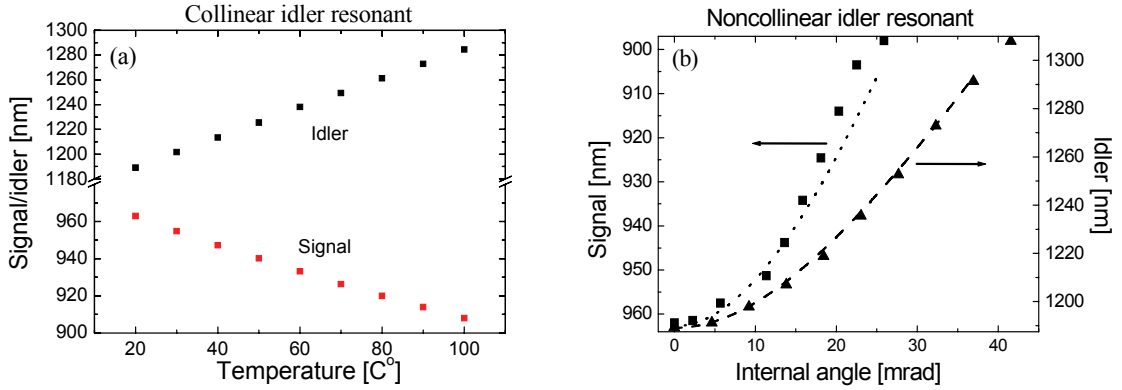

Fig. 4.2. (a): the temperature tuning characteristics when the SRO is collinear, the same dependence in both the signal and the idler resonant cases. (b): angle tuning characteristics by rotating the mirrors. It is clearly seen that the signal tunes faster with angle than the idler. Data points: measurement. Dashed and dotted lines: calculations according to equations (4.1) and (4.2).

configurations tested owing to the good spectral discrimination by the cavity mirrors used. The angular dispersion lines in Fig. 4.2 (b) have been calculated using equations (4.1) and (4.2) and using the Sellmeier expansion given by reference [69]. They show quite good correspondence to the experimentally measured results, especially for the idler wave. The small discrepancy observed in the signal dispersion might be attributed both to the Sellmeier expansion used,[69] and to the experimental uncertainties in measuring the small noncollinear angles. As is evident from Fig. 4.2 (b), the angular dependence of the idler is smaller than that of the signal. By fitting the experimental points to a second-order polynomial the angular dispersion coefficients could be extracted for both the signal and the idler, as are shown in Table 4.1. Although these dispersion coefficients are only valid for PPKTP with this

particular QPM period, the feature of larger angular dispersion for the idler wave is general for PPKTP OPOs pumped at 532 nm.

	$\beta_1 = \partial\theta / \partial\nu$	$\beta_2 = \partial^2\theta / \partial\nu^2$
Signal	1.18 mrad/THz	-0.038 mrad/THz^2
Idler	2.43 mrad/THz	-0.034 mrad/THz^2

Table 4.1. The angular dispersion coefficients for a PPKTP crystal with a period of 9.1 μm, when pumped at 532 nm. The coefficients were extracted from a second-order polynomial fit to the measured data in Fig. 4.2 (b).

From these coefficients, one important feature can be deduced: due to the larger angular dispersion for the idler wave it is possibile to generate more narrow spectral bandwidths by letting the idler resonate inside the OPO. If we consider that the angular acceptance in an OPO is limited by the physical cavity length and the gain channel dimensions as set by the diameter of the pump beam; then, for the same pumping conditions, the idler-resonant PPKTP OPO should generate more narrow spectral bandwidths than the signal-resonant PPKTP OPO even in the collinear configuration. Indeed, it was experimentally measured in our case that the collinear idler-resonant OPO spectral bandwidth was 30% narrower than that of the signal-resonant OPO for the same pump depletion conditions. In the noncollinear PPKTP OPO configuration, the spectral bandwidth is generally expected to increase with the noncollinear angle. There are two main reasons for this. First, it will increase approximately linearly due to the decreasing angular dispersion:[a]

$$\Delta\nu_j(\theta) \approx \frac{\Delta\theta}{\beta_{1j}} - \frac{2\beta_{2j}}{\beta_{1j}^3}\theta\cdot\Delta\theta, \tag{4.3}$$

where $\Delta\theta$ is the acceptance angle of the OPO cavity and $j = s,i$. Equation (4.3) is deduced from the second-order polynomial fit described above. For a flat-flat mirror OPO cavity, the acceptance angle is determined by the cavity length, the pump beam geometry and the pump intensity. Secondly, the non-collinear OPO spectral bandwidth will increase with angle due to decreasing effective interaction length as caused by the smaller overlap between the interacting beams. On the other hand, as the PPKTP OPO is tuned further away from degeneracy, the GVM will contribute to a bandwidth-narrowing effect, as seen in equation (2.16).

Even so, in our OPO case, the influence of the angular dispersion on the spectral bandwidth is clearly stronger than that of the material dispersion. Therefore, the bandwidth-decreasing trends are not observed. The measured spectral bandwidth as a function of the non-collinear angle for the signal-resonant and the idler resonant OPOs are shown in Fig. 4.3. It is evident from the discussions in Section 2.3.3 that the spectral bandwidth dependence on the parametric gain is inversely dependent on the interaction length, which becomes shorter with increasing angle. Hence, the $(gL)^2$ parameter is kept constant in all of our measurements. The data points shown in Fig. 4.3 are for the idler-resonant OPO and the signal-resonant OPO and represent the same tuning range. This makes the influence of the material dispersion on the OPOs spectral bandwidth equivalent in both cases. As expected, the idler-resonant OPO generated a narrower spectral bandwidth than that of the signal-resonant OPO. In the collinear case, the spectral bandwidth of the idler-resonant OPO was approximately 30 % smaller than that of the signal-resonant case and the difference rapidly increased with an increasing non-collinear angle. At the largest non-collinear angle, the frequency bandwidth of the idler-

[a] Unfortunately this equation in article [I] is misprinted; the one used here is the correct one.

resonant OPO was two-times smaller than in the case of the signal-resonant OPO. In strong contrast to the signal-resonant OPO, where the spectral bandwidth monotonically increases with the non-collinear angle, the spectral bandwidth of the idler-resonant PPKTP OPO remained approximately constant for non-collinear internal angles above ~ 25 mrad. In order

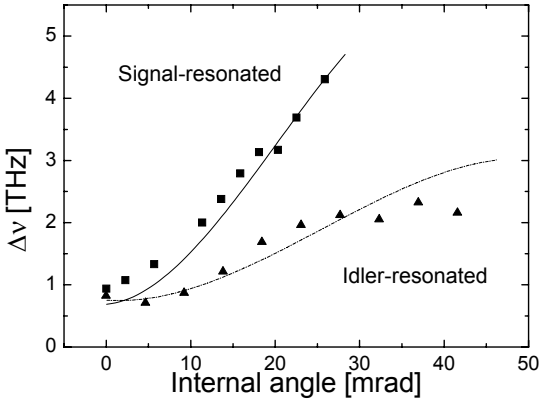

Fig. 4.3. Measured spectral bandwidths for signal- and idler-resonated OPO's. Data points: experimentally measured FWHM spectral bandwidths. The lines are theoretical calculations.

to estimate the expected OPO spectral bandwidth, the parametric fluorescence bandwidth was calculated for the noncollinear angles involved, seen as the two lines in Fig. 4.3. These calculations were preformed by integrating equation (2.14) over the angular distribution of the resonant field at the different non-collinear angles.[13] This will give the spectral bandwidth of the parametric fluorescence; however, as discussed in Section 2.3.3 the spectral bandwidth of an OPO can be estimated by equation (2.21).[22] For this case the number of round-trips was approximated to be 10.

In Fig. 4.3, there is an anomaly in the measured spectral bandwidth of the idler-resonant OPO which was not predicted by this simple model. This off-set from the theoretical

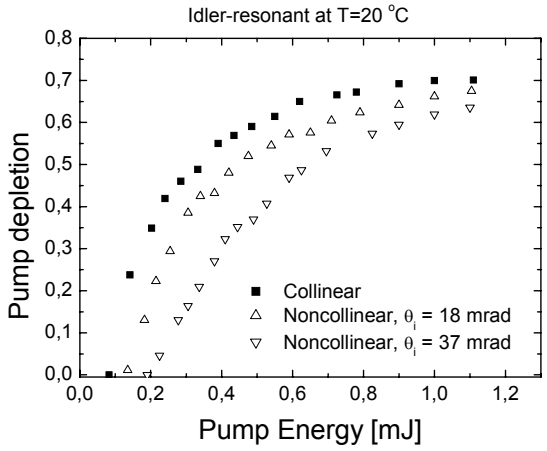

Fig. 4.4. Pump depletion versus pump energy for the idler-resonated OPO, at θ_i = 0 mrad (squares), 18 mrad (triangles) and 37 mrad (circles).

calculations can be explained by the increasing diffractive spreading of the idler-resonant OPO when the idler mode approaches 1300 nm. This diffractive behavior ultimately limits the acceptance angle of the cavity and a further reduction of the spectral bandwidth is evident.

The measured far-field half-angles for these extreme angles in the case of the idler- and the signal-resonant OPOs, were 5.8 mrad and 4.7 mrad, respectively. For the signal-resonant OPO, the M^2-values of the output beam increased with the non-collinear angle from $M^2 = 1.8$ to 3.3, while the M^2 value for the idler-resonant OPO actually decreased from $M^2 = 5$ to 2.3 at the largest non-collinear angle.

The pump depletion of the PPKTP OPO was very high in all of the configurations and this is attributed to a negligible backconversion. In Fig. 4.4, the measured pump depletion for the idler-resonant OPOs are depicted. At the internal angles of $\theta_i = 0$ mrad, 18 mrad and 37 mrad, the OPO reached threshold at pump energies of 83 μJ, 135 μJ, and 190 μJ, respectively. The pump depletion at a pump energy of 1.1 mJ reached values of 70 %, 67 % and 63 %, respectively, for these three cases. In the case of the signal-resonant OPO similar values were found.

The above study showed that by taking advantage of the angular dispersion properties of the KTP crystal, it is possible to decrease the spectral bandwidth with a factor of up to two-times (50 % reduction). Additionally, the spatial quality of the idler-resonant beam increased as an effect of diffraction. The efficiencies were also very high, even though a non-collinear geometry was chosen. This technique, by having the idler resonated in the OPO, can be the first step to decrease the spectral bandwidth and, if this is not enough, further narrowing can be accomplished by deploying a dispersive element inside the cavity or by replacing it for one of the cavity mirrors.

4.1.2 Bulk Bragg Grating as an Output Coupler

In 1943, Bragg and Lipson reported on the "*Description of an apparatus which observes Fraunhofer diffraction at small angles…*".[70] Similar reflection gratings are used in spectrum analyzers and when tuning lasers or OPOs.[17,22] The common idea is to isolate a small spectral component of the emitted spectrum and use it for detection or seeding, respectively. There are more or less efficient ways of generating narrow bandwidths in an OPO by utilizing Bragg gratings. For example, Bragg gratings may be recorded in photorefractive crystals such as PPLN or Co:$BaTiO_3$.[71,72] Unfortunately, several physical restrictions have limited their practical use. In the former case, the PPLN was exposed to UV-light in order to obtain a photorefractive grating acting as feed-back mirrors within the crystal.[71] However, the UV absorption of LN is high and the grating is only formed in the surface layer of the crystal, which results in a very weak feed-back. In the case of Co:$BaTiO_3$, it can be used as an intra-cavity element in a dual-arm OPO.[72] The photorefractive grating in this case is formed by interference and Victori *et al.* used the OPO signal itself to form the grating.[72] However, in order to utilize the grating, the OPO must be above threshold and, since the grating formation time is too slow compared to the pump pulse length, the performance is limited. An additional drawback is that the grating erases at elevated temperature; hence it limits the OPO to low power applications.

The work described here is a new and simplified method to generate narrow spectral bandwidths in near-degenerate SROs. This is done by replacing the dielectric output mirror by a bulk glass Bragg grating. The Bragg grating is permanently recorded in a photosensitive glass with a holographic technique.[73] The advantages of bulk glass Bragg gratings are: (i), their small size (typically 2×2×1 mm), (ii), that there are no measurable degradation with time, and (iii), that it has the ability to withstand high powers, typically 7 J/cm^2 for 1 ns pulses.[74] In recent work, these Bragg gratings have successfully been used to enhance the spectral brightness of Ti:sapphire, Cr:LiSAF and Er:Yb phosphate glass lasers.[75,76]

When writing the grating, a sinusoidal refractive index profile is formed within the medium, expressed as $n(x) = n_0 + n_1\cos(2\pi x/\Lambda)$. Here, n_0 and n_1 are the average refractive index and the modulation amplitude, respectively, with the condition that $n_0 >> n_1$. Λ is the expected grating period and $0<x<d$, where d is the length of the device, seen in Fig. 4.5 (b). The reflected wavelength is determined by the Bragg condition:

$$\lambda_B = 2n_0\Lambda\cos(\theta), \tag{4.4}$$

where θ is the internal angle of propagation relative to the *z*-direction. The peak reflectivity is given by $\tanh^2(\pi n_1 d/(2n_0\Lambda\cos^2\theta))$;[77] furthermore, if we define the bandwidth of the bulk Bragg grating as the distance between the two zeros closest to the peak, it is found to be:[77]

$$\Delta\lambda = \lambda_B\sqrt{\frac{n_1^2}{n_0^2\Lambda\cos(\theta)} + \frac{4\Lambda^2}{d^2}}, \tag{4.5}$$

Thus, by changing the length d or the modulation amplitude n_1, both the reflectivity and the bandwidth can be adjusted.

The experimental setup is shown in Fig. 4.5 (a) and consists of a linear PPKTP SRO cavity, where the output mirror has been replaced with a bulk glass Bragg grating. The cavity supports signal resonance and is coated accordingly. The PPKTP crystal had a QPM period of 9.01 μm and was pumped by the same laser as described in the previous paragraph. The measured characteristics of the bulk Bragg grating can be seen in Fig. 4.6 (a), having a central wavelength of 975.3 nm, a peak reflectivity of 27% and a FWHM spectral bandwidth of 0.71 nm. The corresponding idler wavelength is 1170 nm.

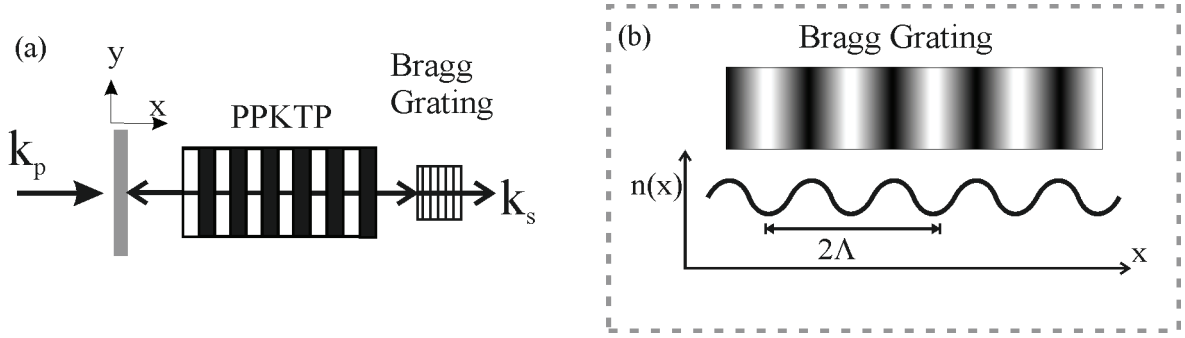

Fig. 4.5. (a): a linear SRO setup when using a Bragg grating as an output coupler. (b): an arbitrary refractive-index modulation, n(x), of a Bragg grating.

Shown in Fig. 4.6 (b) are the signal spectra for two cases. The broad spectrum is what we obtain when using a conventional dielectric output mirror, while the narrowed spectrum is the result of deploying the bulk Bragg grating. The FWMH bandwidth of the signal for the Bragg grating cavity was 0.16 nm (50 GHz), whereas the conventional mirror yielded a bandwidth of 3.0 nm (950 GHz), respectively. All-in-all, a decrease of the spectral bandwidth of approximately 20 times was achieved when using the bulk Bragg grating. As mentioned before, in order to compare the two cases, the parametric gain should be equal to each other and the two spectra seen in Fig. 4.6 (b) are measured at 30 % pump depletion.

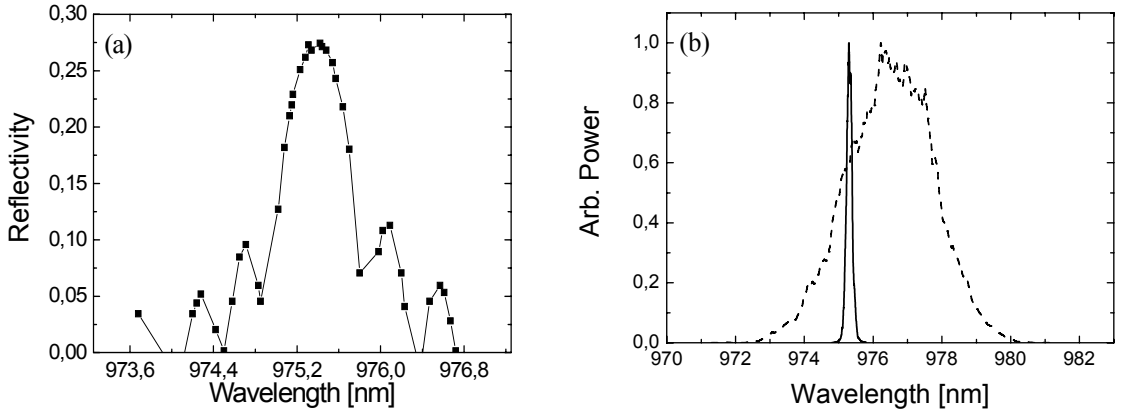

Fig. 4.6. (a): The measured reflectivity of the bulk glass Bragg grating, with a peak reflectivity of 27 % at 975.3 nm. (b): The recorded spectra for the conventional mirror (dash line) and for the Bragg grating (solid line).

One of the advantages with SRO's is the ability to improve the signal's (idler) spatial beam profile compared to that of the pump beam.[14,78] The beam propagation factor, M^2, for the signal was measured to be approximately 3.3 in both the horizontal and the vertical direction, the pump's corresponding valuc was $M^2 = 9$. When using the conventional output mirror, the M^2-value was found to be approximately the same. The OPO threshold was reached at 0.14 mJ of pump energy for a 17 mm cavity and 0.25 mJ for a 33 mm long one, increasing with the cavity length as expected.[22] The pump depletion saturated at a value of 55% for the 17 mm long cavity and at 45% for the 33 mm long one. Using the shorter cavity, the emitted signal energy reached 340 μJ for 1.7 mJ of pump energy; the corresponding value for the longer one was 250 μJ.

In order to determine if the bulk Bragg grating would cause additional cavity losses, we evaluated the efficiency of the OPO (i.e., what fraction of the pump energy is converted to OPO signal and idler), comparing the bulk Bragg grating OPO once again to one with an ordinary mirror as output coupler. In both cases, the efficiency reached 70% of the measured depletion. Thus, we concluded that no additional losses were caused by the bulk Bragg grating. Furthermore, we observed no degradation of the Bragg grating after more than 80 hours of exposure to 20 Hz, 5 ns pulses with approximately 200 MW/cm^2 peak intensity,

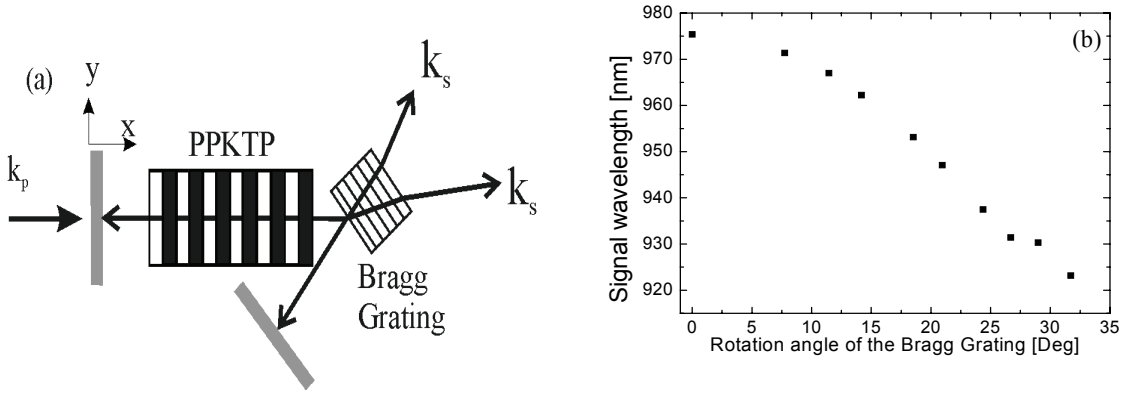

Fig. 4.7. (a): The folded cavity, with signals emitting in two directions. (b): Tuning behaviour as a function of the rotation angle of the Bragg grating.

in accordance with the results of reference [74]. In addition, the grating showed a very low temperature dependence of only 0.010 nm/°C; this stable behaviour is very attractive for

many applications where the ambient temperature fluctuates. It should also be pointed out that the signal wavelength stays constant when the device is left free running, without the need for any additional adjustments or feed-back loops, showing a notable stability for such a simple device.

The device could also be angle tuned by inserting an additional cavity mirror, as seen in Fig. 4.7 (a). This folded cavity had a total cavity length of 33 mm and, by rotating the Bragg grating, the reflected signal could be tuned according to equation (4.4). To accommodate for the tuning, the gain of the PPKTP crystal was shifted in wavelength by raising the crystal temperature. When rotating the bulk Bragg grating an external angle of 0° to 32°, the OPO signal wavelength was shifted from 975 nm to 923 nm, seen in Fig. 4.7 (b), while keeping a bandwidth of between 0.15 nm and 0.17 nm. However, this folded cavity has two signal outputs, which decreases the overall efficiency; this can, however, be avoided by constructing a ring cavity instead.

To the best of our knowledge, this was the first time a bulk Bragg grating was used as an output coupler in an OPO. This particular work, which is described in article [II], have been the subject for a review article in the magazine *Photonics Spectra's* October issue 2005.[79]

In another work, not part of this thesis, we have further explored the advantages of using a Bragg grating as an output coupler in a near-degenerate OPO pumped at 1064 nm. The signal output at 2008 nm had a spectral bandwidth of 37 GHz, a decrease of close to 80 times compared to using a conventional dielectric mirror. The spectrally narrowed signal was subsequently employed for pumping a ZGP OPO, which generated tuneable radiation in the atmospheric transmission windows of between 3.3 μm and 5.2 μm. To the best of our knowledge, this was the first time the output from a near-degenerate type-I PPKTP source was used for pumping a ZGP parametric oscillator.[A6]

4.1.4 Self-Seeded Optical Parametric Oscillator

The work described in article [III] deals with the construction of a wavelength-agile PPKTP OPO. It is a continuation of the work done on the noncollinear idler-resonant SRO described above and we will report on a self-aligned, double ring parametric oscillator, with the potential to generate narrow linewidths. The work is conducted with the same PPKTP crystal, pump source, and at the same wavelength, as well as the same input and output mirrors as for the work described in section 4.1.1.

The inherently unidirectional nature of the parametric ring oscillators and the angular separation of the generated waves in a noncollinear SRO, can be utilized for easy seeding arrangements. In the situation of a ring cavity SRO, the former property can be facilitated to support *two* independent counter-propagating resonant waves in the same cavity. The counter-propagating waves can also be tuned over practically the same spectral range as for the linear idler-resonant SRO described in article [I]; where the tuning behavior follows the equations (4.1) and (4.2), shown above. However, the tuning can now be accomplished by changing only one degree of freedom. The idea in this work was to modify the generated spectrum in *one* direction, while using this output for cross-seeding the ring oscillator propagating in the *opposite* direction. How this was done will be explained in more detail later in this section.

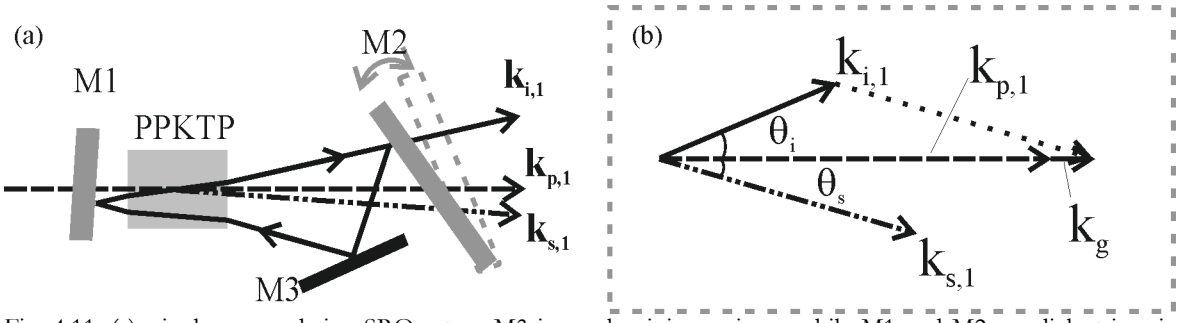

Fig. 4.11. (a): singly pumped ring SRO setup. M3 is an aluminium mirror, while M1 and M2 are dielectric mirrors supporting the idler resonance (SRO). (b): wave vector diagram for the noncollinear interaction.

First, consider the case when only one pump beam is launched into the ring SRO, as shown in Fig. 4.11 (a). The corresponding wave vector diagram is seen in Fig. 4.11 (b). By simply rotating the mirror M2, it is possible to tune the ring cavity. In our case using, a $\Lambda = 9.1$ μm PPKTP, it was tuneable from 1189 nm to 1267 nm and from 968 nm to 917 nm, for the idler and the signal, respectively. The limiting factor on the total continuous tuning range was the aperture of the mirror M3. The measured pump depletion for three different noncollinear angles are depicted in Fig. 4.12. The efficiency is lower for this ring SRO than for the linear SRO, as described in Section 4.1.1, which is primarily due to the longer cavity and some additional losses for the aluminium mirror (M3). In Fig. 4.12, the pump depletions for three noncollinear angles are depicted. For example, when a peak intensity of ~190 MW/cm^2 was incident on the crystal, a pump depletion of close to 50 % was found at an internal angle of $\theta_i = 18$ mrad, corresponding to a wavelength $\lambda_i = 1221$ nm.

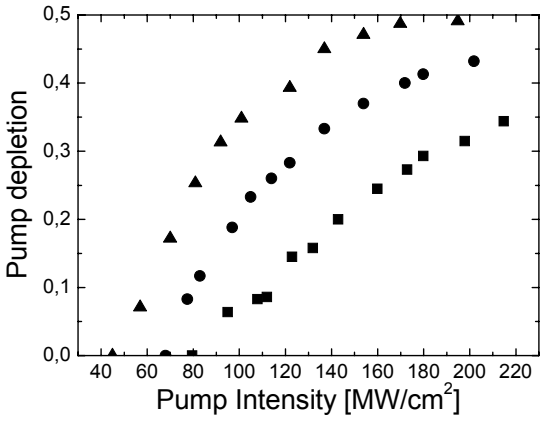

Fig. 4.12. Pump depletion for noncollinear angles $\theta_i = 18, 24,$ and 30.7 mrad, corresponding to wavelengths of 1221 nm (triangles), 1241 nm (circles) and 1267 nm (squares), respectively, as a function of peak intensity.

The unidirectional nature of the parametric ring resonators can be fully exploited by even launching a backward pump beam [$k_{p,2}$ in Fig. 4.13 (a)] into the cavity from the opposite direction with respect to the forward pump beam $k_{p,1}$. When the two beams are overlapping ($k_{p,1} = -k_{p,2}$), the cavity then supports two independent, automatically aligned and counter-propagating parametric ring oscillators. Moreover, the signal and the idler outputs of both oscillators are easily separated as shown in Fig. 4.13, which is useful for our purpose. Through a beamsplitter the pump beam is re-routed into the two counter-propagating pump beams seen in Fig. 4.13 (a) and they are hereinafter refer to as: the forward pump (P_1) and the backward-pump (P_2). The pump beams P_1 and P_2 were focused to an e^{-2} intensity radii of 155 μm and 200 μm, respectively, inside the PPKTP crystal. A slightly larger beam waist of the

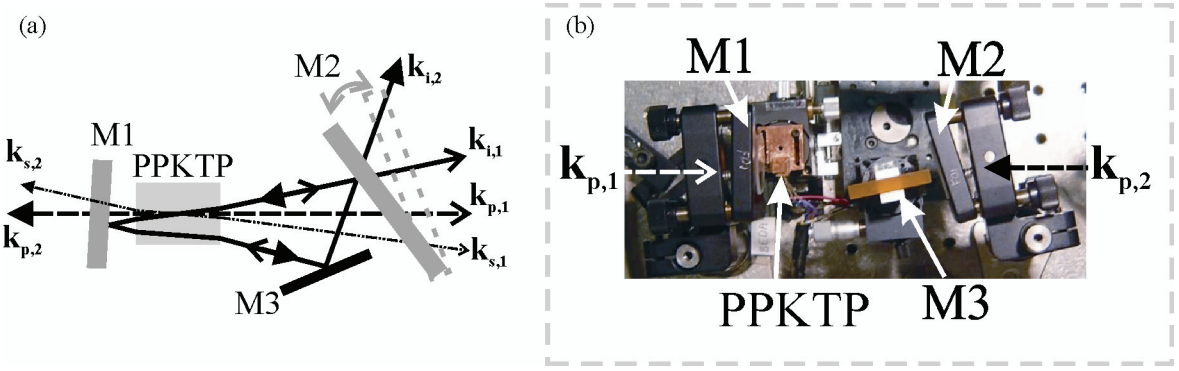

Fig 4.13. (a): double-pumped OPO setup, where $k_{p,1}$ and $k_{p,2}$ are counter-propagating and generating two independent idler-resonant waves $k_{i,1}$ and $k_{i,2}$, respectively. They are also emitted in different direction, see the figure. (b): top-view picture of the experimental setup.

backward-pump beam was chosen in order to better mode-match the seed beam and thus to increase the seeding efficiency in a cross-seeded ring OPO configuration, as will be described below. The larger beam size of the backward pump yields a lower operational threshold since the effective noncollinear parametric interaction length will now be longer than for the forward pump.[68] It was found that the threshold for the forward pump was approximately 1.5-times larger, corresponding to the ratio between the pumps radii squared. Since the counter-propagating ring oscillators share the same physical beam path, the output wavelength generated in both rings can simultaneously be tuned by rotating the mirror M2.

The independence of the two counter-propagating ring OPO's can also be exploited to generate two signal (idler) waves at distinct and tunable wavelengths in the same cavity by using the forward- and the backward-propagating pump sources at slightly different wavelengths, which are still within the phase-matching range of the QPM crystal. For instance, by employing the PPKTP crystals with the periodicity of 9.1 μm, and using two frequency-doubled single-frequency Q-switched YAG lasers detuned by 50 GHz as pump sources would produce two counter-propagating signal or idler waves with an approximately constant frequency separation of 500 GHz over the whole tuning range.

On the other hand, the double-ring OPO configuration can also be used to generate parametric waves with a modified spectrum by seeding one of the ring oscillators by the spectrally-filtered output of the other ring, as we will demonstrate below. In order to achieve this, the aluminum mirror (M3) was exchanged with a diffraction grating. The grating diffracted the idler wave generated by the forward-pump (P_1) into the minus first order (m = -1) with an efficiency of approximately 35 %. In Fig. 4.14, the expanded experimental setup is seen. The diffraction grating and the mirror M4 were located in the conjugate planes of the lens with a focal length of f = 50 mm. This is a zero-dispersion arrangement, which only reverses the direction of propagation of the optical beam without changing the spectral or the spatial properties at the point of beam diffraction at the grating.[80] The spectral filtering can be performed in the Fourier plane (plane of the mirror M4) by inserting appropriate spatial masks. Overall, about 10% of the idler generated in the forward-pumped OPO was utilized for seeding the opposite-directional ring OPO.

The measured pump depletion for the unseeded backward-pumped (P_2) SRO and the seeded backward-pump OPO are depicted in Fig. 4.15 (a). The pump depletion was measured for the OPO alignment, corresponding to the noncollinear internal angle of θ_i = 22.3 mrad (the conjugate angle for the signal was θ_s = 16.7 mrad). The unseeded, backward-pumped ring OPO reached the threshold at 43 MW/cm^2. It is evident by comparing Fig. 4.12 with

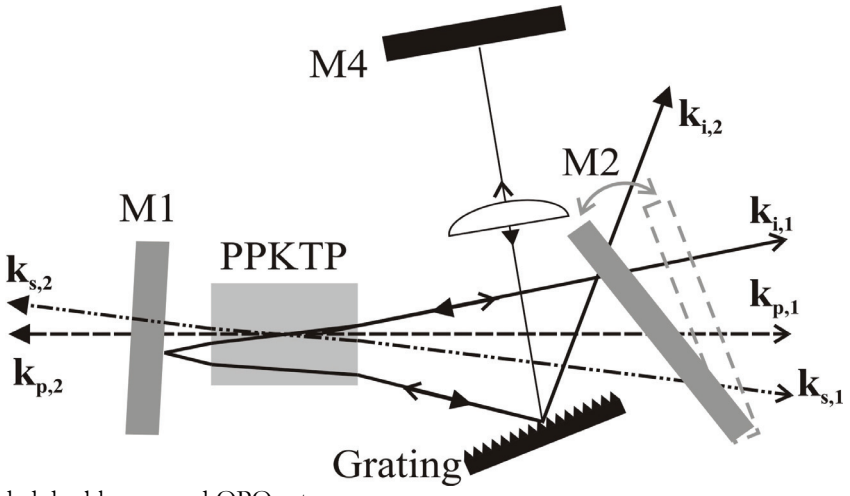

Fig. 4.14. Self-seeded double-pumped OPO setup.

Fig. 4.15 (a) that the larger beam waist of the backward pump provides for a faster rise in the backward-pumped ring OPO efficiency; this is a usual feature for noncollinear parametric interactions.[68] Consequently, the unseeded, backward-pumped ring system reached an efficiency of 46 % at a pump intensity of 110 MW/cm^2 and was only limited by the available pump power. When evaluating the cross-seeded ring configuration, we kept the forward pump power at a constant intensity of 200 MW/cm^2 and varied the power of the backward pump. At this forward pump level, and with an aluminum mirror as M4, the seed energy injected into the opposite-directional ring was 14 μJ. In the seeded configuration, the backward pump depletion reached nearly 46 % at 84 MW/cm^2 pump power generating 117 μJ idler and 123 μJ signal energies, respectively.[b] The measured spatial profile of the idler beam in the far-field region was almost perfectly circular and the intensity distribution was Gaussian, with an $M^2 = 2$.

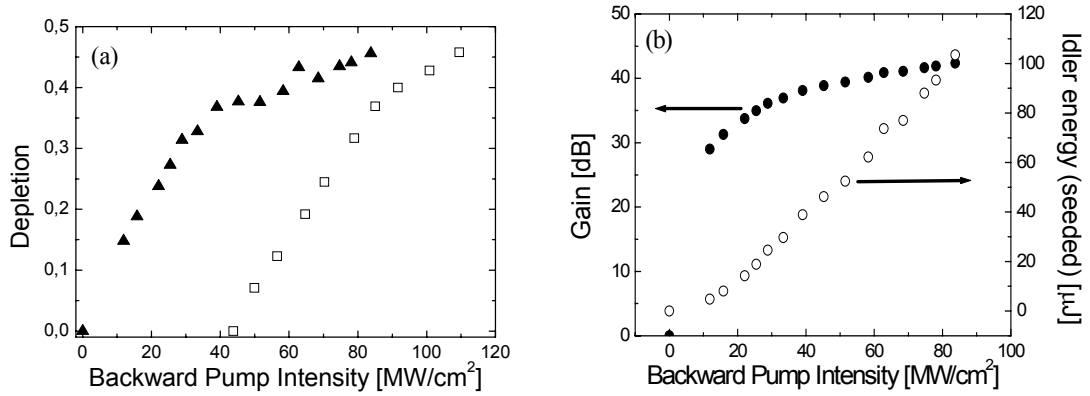

Fig. 4.15. (a): measured pump depletion as a function of pump intensity (in the case of M4 is an aluminum mirror). The unseeded backward pumped OPO (open squares) and the seeded backward pumped (solid triangles) OPO. In the latter case the intensity of the forward pump P_1 was kept constant at 200 MW/cm^2 (seed of 14 μJ). (b): measured gain when M4 is a strip mirror and the idler energy output as a function of pump intensity (seed of 6 nJ). P_1 was kept constant at 200 MW/cm^2.

Next we investigated the possibility of manipulating the seed spectrum in the Fourier plane by utilising the fact that the spectral frequencies are spatially distributed over mirror the M4. First, we inserted a vertical 40 μm-wide beam block onto the front of the mirror M4 thus

[b] Misprint in article [III]. These are the correct energy levels.

producing a hole in the seed spectrum. The effect on the backward-pumped OPO idler spectrum is shown in Fig. 4.16 (a). The beam block could be translated horizontally thus placing the spectral "void" at a pre-desired position. The FWHM width of the spectral hole in the OPO output was 295 GHz. Thereafter, we inserted a 20 μm-wide, thin-strip mirror instead of the mirror M4 and hence reflected back only a small part of the frequency spectrum, as shown in Fig. 4.16 (b). The seed's FWHM bandwidth was 56 GHz and its position could be tuned over the whole frequency range by translating the stripe-mirror in the Fourier plane. For this Fourier filter setup, a theoretical calculation, assuming a diffraction-limited optical system, indicated a spectral bandwidth of 38 GHz. For the beams with an $M^2 = 2$, as in the case of the OPO idler, the spectral bandwidth of the filter increases to about 54 GHz which concurs very well with the experimental data.

In this configuration, the seed energy incident on the PPKTP was only 6 nJ, being significantly reduced due to imperfections of the stripe-mirror. The saturated gain was measured to be 42 dB and an idler energy of 103 μJ was achieved, as seen in Fig. 4.15 (b). The resulting seeded idler spectrum from the backward-pumped ring OPO, at full pump power, is shown in Fig. 4.16 (b), where it is compared with the unseeded OPO spectrum. The

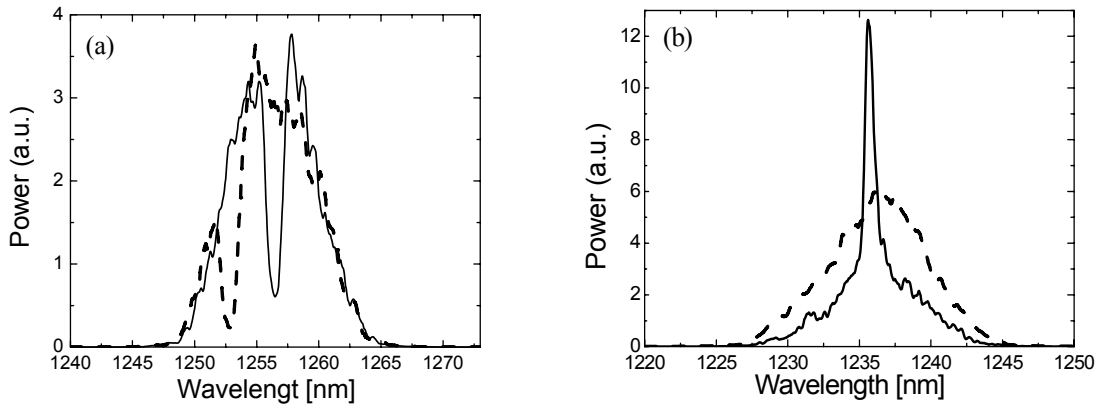

Fig. 4.16. (a): output spectra for the P_2 idler spectrum, when the seed was manipulated with a beam block in the Fourier plane. (b) output spectra when seeded from a thin stripe-mirror in the Fourier plane (high peak, solid curve) and unseeded idler spectrum (broader spectrum, dashed curve).

broadband pedestal appearing in the seeded spectrum originates from the onset of the competing unseeded operation of the OPO due to the low seed energy. The measured peak-to-pedestal contrast ratio was 35 dB at the backward pump intensity of 33 MW/cm^2 and it decreased to 6.4 dB for the pump intensity of 68 MW/cm^2. Clearly, the contrast can be increased by using a better quality stripe-mirror and more pump power in the forward-pumped ring OPO. The FWHM of the spectral peak at full pump power ($P_1 = 200$ MW/cm^2) was 137 GHz and should be compared with the FWHM of 1.43 THz of the unseeded OPO.

In order to further reduce the spectral bandwidth of this novel, double-pump ring SRO, a diffraction grating with larger groove density and a Fourier lens with a longer focal length can be used. The use of diffraction-limited beams would also be preferable. The goal during this investigation was not to reach as narrow spectral bandwidths as possible, however, it can clearly be achieved. In addition to the spectral narrowing, the current ring OPO setup allows one to manipulate and shape the spectrum in many other ways as an application requires. This configuration would, for example, be suited for measuring small objects, by placing them in the Fourier plan. For more details regarding the study, consult article [IV].

4.2 Cascaded Second-Order Interactions

Parametric devices with crystals that lack inversion symmetry are very useful for a number of nonlinear processes that can be identified through the second-order susceptibility tensor, $\chi^{(2)}$. Effects such as harmonic generation and frequency-mixing have paved the way for accessible coherent multi-frequency laser sources, which can be used, for example, in spectroscopy. The concept of multi-frequency source can be further extended when considering the cascaded second-order nonlinear interaction occurring in a nonlinear crystal. The well-known phenomena arise from the $\chi^{(2)}$:$\chi^{(2)}$ interaction and emulate the third-order susceptibility.[24] The magnitude of the effective $\chi^{(2)}$:$\chi^{(2)}$ interaction is, in many cases, greater than in pure $\chi^{(3)}$ materials, which, on the other hand, is limited to third-harmonic generation and Kerr-like effects. Furthermore, cascading of optical parametric devices have been used to: (a), create new optical frequencies in parametric oscillators and amplifiers;[81,82] (b), introduce nonlinear phase-shift in a counter-propagating parametric amplifiers;[83] (c), induce amplitude modulation in order to passively mode locked a laser;[84] and (d), to self-diffract the output beams from a barium borate (BBO) crystal.[85]

In the work described in article [IV], we have demonstrated a resonant coupling of two independent noncollinear OPO's realized in the same PPKTP crystal and the same cavity by using a parametric gain grating. Through a cascaded, nondegenerate four-wave mixing process, a resonant coherent coupling leads to the generation of equidistant frequency sidebands in the signal, the idler and the pump beams.

Graphically, the process can be understood from an analysis of the wave-vector diagrams in Fig. 4.17. The OPO cavity is pumped by two pump waves, k_{p1} and k_{p2}, which intersects with an angle of 2θ inside the same PPKTP crystal. The OPO cavity is formed by two mirrors which are, in general, aligned at an angle with respect to the crystal x-axis, seen as angle α in the Figure. The QPM grating wave vector is directed along the x-axis and is denoted k_{QPM}. Because the angles between the resonator axis and the two pump waves are different, two

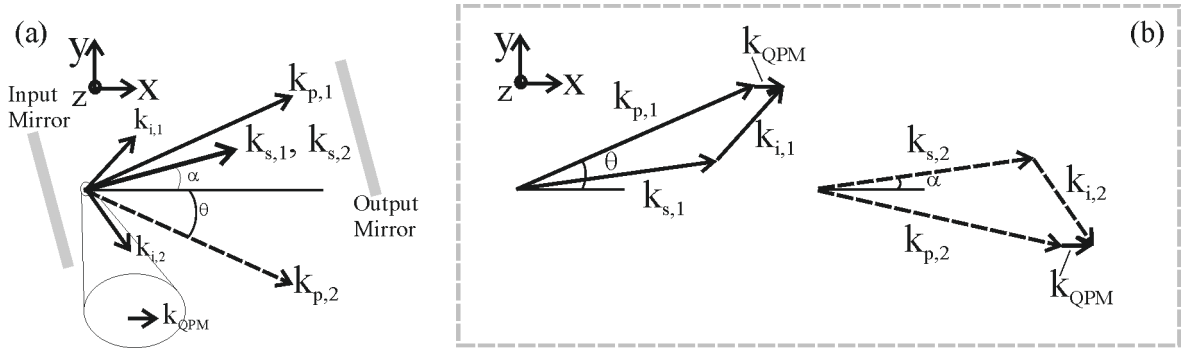

Fig. 4.17. (a): The OPO cavity shown without the PPKTP crystal. Two different and independent signal waves are generated in direction of the cavity, which is set by the angle α. (b): the wave vector diagrams of the two independent processes taking place within the same PPKTP crystal.

distinct signal (idler) waves k_{s1}, k_{s2} (k_{i1}, k_{i2}) will be generated in the cavity. It is only in the case of the symmetric configuration, i.e., when the cavity axis is aligned along the PPKTP x-axis (α = 0), that both pump waves will generate OPO signals (idlers) at the same wavelength. In the two-beam pumped OPO, the mutual coherence of the pump waves plays a crucial role. Conceptually, when the mutually coherent pump waves interfere inside the PPKTP crystal an interference pattern is formed which can be viewed upon as a gain grating. The corresponding wave vector, K_{gg}, of the periodic interference pattern is directed along the y-axis and the modulation period is $\Lambda = \lambda_p/(2n \sin\theta)$, where λ_p is the pump wavelength, n is the refractive

index at the pump wavelength and θ is the pump angle as seen in Fig. 4.17. The interference of the pump beams has three important consequences for the operation of the OPO:

(i), the increase of the intensity will reduce the OPO threshold.

(ii), due to the interference-related gain grating along the y-axis, there is a possibility to phase-match the signal and the idler pairs which are normally not amplified. For instance, for gain grating related coupling, the signal wave $k_{s2} = k_{p2} - k_{i2} - k_{QPM}$, can now be amplified by the pump wave, k_{p1}, in the process $k_{s2} = k_{p1} - k_{i2} - k_{QPM} - K_{gg}$, leading to a coupling between two independent noncollinear OPO's.

(ii), cascaded interactions between the parametric waves in the coherently coupled OPO's will lead to the resonant generation of new frequencies in the signal, the idler and the pump beams. From the $\chi^{(2)}:\chi^{(2)}$ interaction new frequencies can be deduced analytically. For example, the new signal frequencies, ω_{s3} and ω_{s4}, can be found through:

$$\begin{aligned}\chi^{(3)}_{zzzz}\left(-\omega_{s3};-\omega_{i3},\omega_{i2},\omega_{s1}\right) &= \chi^{(2)}_{zzz}\left(-\omega_{s3};-\omega_{i3},\omega_{p3}\right)\times\chi^{(2)}_{zzz}\left(-\omega_{p3};\omega_{i2},\omega_{s1}\right)\\ \chi^{(3)}_{zzzz}\left(-\omega_{s4};-\omega_{i4},\omega_{i1},\omega_{s2}\right) &= \chi^{(2)}_{zzz}\left(-\omega_{s4};-\omega_{i4},\omega_{p4}\right)\times\chi^{(2)}_{zzz}\left(-\omega_{p4};\omega_{i1},\omega_{s2}\right),\end{aligned} \tag{4.6}$$

where we have followed the convention from reference [6]. Since the highest nonlinearity in PPKTP is along the crystallographic z-axis, we only consider Type I interaction. In addition, these interactions are only phase-matched at a specific noncollinear angle, α, and are depending on the presence of the wavevector K_{gg}. Thus, it is a result of resonant phase-matching due to the parametric gain grating. The corresponding idler and pump frequencies should also be expected in the OPO spectrum.

The experimental setup is shown in Fig. 4.18. It consists of an SRO built around a PPKTP crystal with a grating period of Λ = 35.4 μm. The input and output mirrors supported signal resonance between 1450 nm and 1650 nm, respectively, while transmitting the pump beams at 1064 nm and the idlers. The pump source (the same as in the above experiments, i.e., 5 ns pulse length at 1064 nm) was split into two parts by a beamsplitter and a delay line was

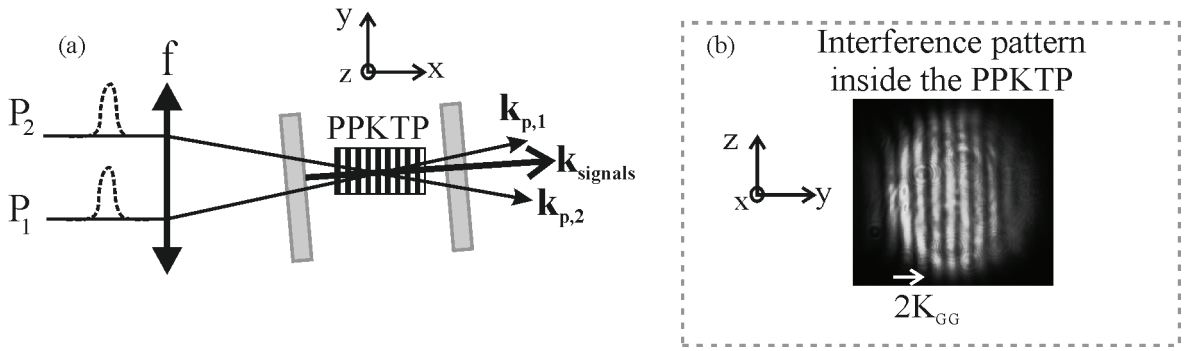

Fig. 4.18. (a): the experimental setup. Two pump beams (P1 and P2) are incident on the SRO, where P1 can be delayed in respect to P2. (b): the interference pattern inside the PPKTP crystal, due to the mutual coherence of the pump beams. Note the axis orientation.

inserted in the path of P1 (not shown). Since the two beams are from the same laser source they are mutually coherent. However, the temporal coherence length of the source is only around 120 ps. This enables us to investigate the multi-beam pumped OPO's dependence on the mutual coherence of the pump beams. Thus, when the coherent waves, $k_{p,1}$ and $k_{p,2}$, are

overlapping temporally and spatially inside the PPKTP crystal an interference pattern is formed in the pump beam, as shown in the CCD-camera frame in Fig. 4.18 (b). The OPO cavity axis was rotated with respect to the PPKTP x-axis.

When the OPO's were operated in a collinear mode ($\alpha = 0$, see Fig. 4.17), it was possible to investigate the dependence of the mutual pump coherence on the threshold for the OPO's. In this case, two signal wavelengths at 1550 nm were generated at a pump angle of $\theta = 22$ mrad. Shown in Fig. 4.19 (a) is the OPO threshold energy as a function of the delay-time of pump P_1 with respect to P_2, whereas Fig. 4.19 (b) shows the superimposed spectra from the waves $k_{s,1}$ and $k_{s,2}$. As is evident from the Figure 4.19 (a) the threshold is

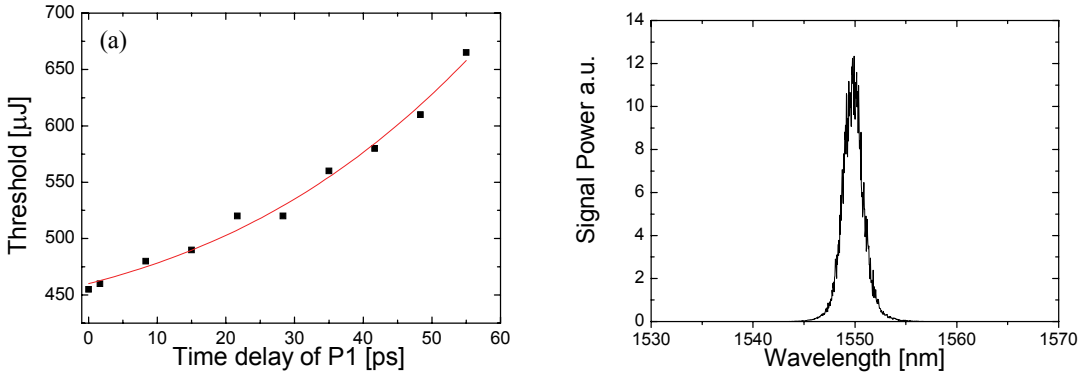

Fig. 4.19. (a): Threshold as a function of time delay of pump P1. Square - measurement. Curve: Gaussian fit. (b): measured spectrum when $\alpha = 0$. The wavelengths $\lambda_{s1} = \lambda_{s2}$.

exponentially increasing as P_1 is delayed, which concurs with the statement (i) given above. At perfect overlap between P_1 and P_2, the measured thresholds were ~ 455 μJ (for P1 and P2, respectively) and, when only one pump beam was incident, it was measured to be ~900 μJ. The solid-line in Fig. 4.19 (a) is a Gaussian fit to the experimental results and can be seen as the result of the convolution of the interference term $2\langle E_{P1}(t) \bullet E_{P2}(t-\tau)\rangle$. From the limited number of data points, the temporal coherence length of the pump could be approximated to be equal to ~ 140 ps (at e^{-2} intensity). For the same pump angle of $\theta = 22$ mrad, we recorded the spectra of the two signals when the OPO-cavity was closely aligned along P_1's direction (α~7.5 mrad), depicted in Fig. 4.20 (a). The wave vector diagram corresponding to this situation is seen in Fig. 4.17 (b), whereas the energy diagram for this particular process is depicted in Fig. 4.20 (b). At this cavity angle, there are no presence of coherent coupling nor of cascading, only the two signal beams ($k_{s,1}$ and $k_{s,2}$) generated by P_1 and P_2 are obtained. The spectral distance between the two signal peaks can be adjusted by rotating the cavity axis, a feature which can be useful is some applications. The coherent coupling and cascading have a resonant character due to lateral phase-matching by the parametric gain grating, K_{gg}. Thus, for a given pump angle of incidence one should expect the cascading to occur for a particular separation between the two signal peaks. When rotating the cavity to a noncollinear angle of $\alpha = 3$ mrad, the coherent coupling becomes evident, as shown in Fig. 4.21 (a). Here, the new resonant signal beams are seen as sidebands symmetrically spaced by 1.5 THz around the original signal peaks. There were also frequency sidebands in the spectral vicinity of $k_{p,1}$ and $k_{p,2}$, which are depicted in Fig. 4.21 (b). These side peaks, denoted P3 and P4, are observed both along P1's direction as well as along P2's direction. Thus, in the case of P3, it is first generated through the process of $\chi^{(2)}_{zzz}(-\omega_{p3};\omega_{i2},\omega_{s1})$ along with P2; thereafter, a part of the

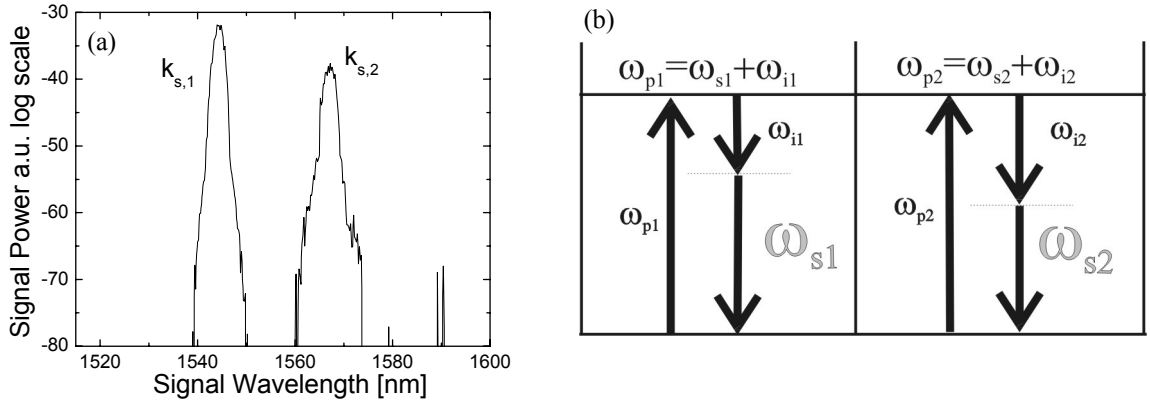

Fig. 4.20. (a): recorded spectrum at a cavity angle of α = 7.5 mrad. No resonant coupling between the two OPOs has occurred. (b): energy diagram of the process.

P3-wave is self-diffracted by the presence of K_{gg} into the direction of P1. The *new* pump wave generates a signal and an idler at the frequencies $\omega_{s,3}$ and $\omega_{i,3}$, where the signal is resonant along the cavity direction. P4 is created in the same manner (see the second row in equation (4.6)) and undergoes self-diffraction, however, in the opposite direction. For the pump angle of θ = 22 mrad the gain grating wave vector, K_{gg}, corresponds to the separations of the generated sidebands (1.5 THz). Due to the coherent coupling character of the pump beams, it was easy to verify the complete disappearance of all of the sidebands by delaying the P_1 pump beam by ~ 50 ps.

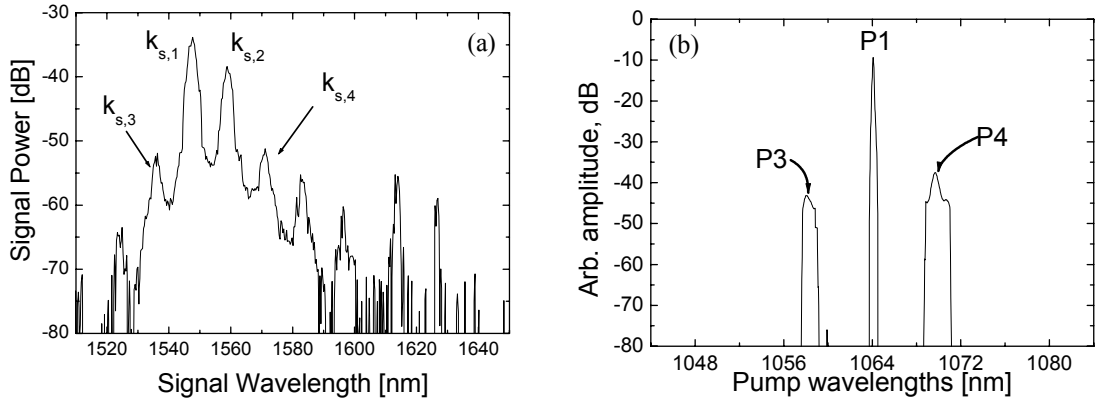

Fig. 4.21. (a): coherent coupling between the two resonant SROs at a noncollinear angle of α = 3 mrad, this effect is due to the gain grating wave vector, K_{gg}. (b): spectrum recorded in the direction of P1, when cascaded resonance is present. The same spectrum is observed along P2's direction. The spacing between the side-peaks is 1.5 THz.

Additional side-peaks are seen in Fig. 4.21 (a) with the same spacing (i.e., 1.5 THz), and they are believed to be due to higher-order cascaded interactions. However, they are not further investigated. With this work, we have demonstrated a two-beam-pumped noncollinear OPO in PPKTP, which generated two signal (idler) waves with tuneable spectral separation. Furthermore, the coherent pumping scheme leads to a parametric gain grating that resonantly enhances the generation of sidebands by the cascaded second-order interaction. These new frequencies were deduced through the susceptibility tensors $\chi^{(2)}$:$\chi^{(2)}$ which is similar to the third-order parametric process.

Preceding this work, with mutually coherent pump beams, we have investigated the same OPO with two synchronized Nd:YAG lasers. The lasers were passively Q-switched with Cr:YAG as saturable absorbers which were pumped slightly below threshold. A third laser that acted as an active Q-switcher, was beamsplitted and the two new beams were focused into the respective Cr:YAG crystals. Hence, the Cr:YAG crystals could be bleached at the same time and pump the OPO in a similar way as described above. However, since the pump beams were not mutually coherent, no cascaded effects were seen.

Chapter 5

Broadband Parametric Generation and Amplification

In 1965 Wang and Racette measured less than 1 dB gain from an OPA using an ADP crystal,[5] and two years later optical parametric fluorescence was observed by Harris *et al*.[4] The delay in observation of OPG and the low gain of the OPA was due to two limiting parameters at that time: low pump powers and inefficient nonlinear optical materials. Today, with matured QPM technology and commercially available high-power pump sources, QPM OPAs can support small signal single-pass gain of more than 55 dB.[86,87] If there are no suitable seed source one can utilize an QPM OPG for seeding an OPA.[88,VII] The benefits with using an OPG as a seed source, is that it extends the tuning range of a pump laser source and the seed's output spectra can easily be matched to that of the OPA; this becomes especially important when broadband amplification is wanted.

OPAs operated in ps and fs regimes are today a common tuneable source and are used in ultrafast spectroscopy.[16,89] These kind of devices can be tuneable from the UV and all the way to mid-IR, however, in multiple stages.[89] Broad bandwidths are also needed for producing few-cycle pulse in order to be able to generate high harmonics, so called soft x-rays.[90] For this particular application it is beneficial to have ultrashort pulses (= broad bandwidths) in the mid-IR.[91] The time scale of these high harmonics are a few hundred of attosecond (10^{-18} seconds), and this is also the time scale for which an electron revolves around its hydrogen core. Thus, it now becomes possible to monitor an atom's response and behaviour on an atomic time scale; making observation of quantum dynamics possible.[90] Moreover, in the field of biomedical optical imaging, it is beneficial to use picosecond broadband sources in the infrared in order to improve the resolution of, for example, optical coherence tomography.[92]

In contrast to lasers nonlinear optical materials do not store energy,[6-8] which means that the thermal load in these devices are low and this makes OPAs very attractive for power scaling applications. As mentioned above, an OPG can serve as a seed source for the OPA, and one of the challenges is to find a nonlinear material that have broad parametric gain and large nonlinearity. The motivation being that it would be possible to construct a table-top parametric device, which is pumped at moderate pump levels, while having the ability to be tuneable over a large spectral range. This would, especially, be interesting for spectroscopic applications.

The observation of the "magic" angle in BBO by Gale *et al.* in 1995,[93] lead to interest for BBO in femtosecond OPOs and OPAs, since it become possible to generate broadband parametric gain in the visible and the near-IR.[16,94] This concept has been extended to longer wavelengths in an OPA source emitting at around 3 μm based on type-I oo-e phase-matched MgO:$LiNbO_3$, pumped by an amplified Ti:Sapphire.[95] Nevertheless, in the spectral region 0.8 μm to 4 μm it is in many cases beneficial to employ QPM nonlinear crystals, since they can offer larger effective nonlinearities and noncritical interaction over the whole spectral

range. In the case of PPKTP, it possible to generate parametric gain between ~1.06 μm and up to about 4 μm in collinear propagation direction, when appropriate grating period and pump wavelength are deployed.

In this chapter the observation of ultrabroad bandwidths in PPKTP parametric generator are discussed and explained. Later in the chapter, the construction of an ultrabraod spectrum is spectrally manipulated and then usein a highly efficient OPA.

5.1 Towards Ultra-Broad Spectral Bandwidths

If large bandwidth is the objective for a parametric device, then there are two important criterions that should be fulfilled in order to generate ultra-broad bandwidths. First, the parametric device should be operated at degeneracy; the spectral bandwidth then becomes dependent on the GVD, see equation (2.17). Secondly, it is also beneficial that the degeneracy point and the point of zero-GVD of the nonlinear material overlap. At this particular point equation (2.17) needs to take third-order dispersion into account, since the GVD of the idler and the signal are approximately equal and the bandwidth becomes very broad. According to

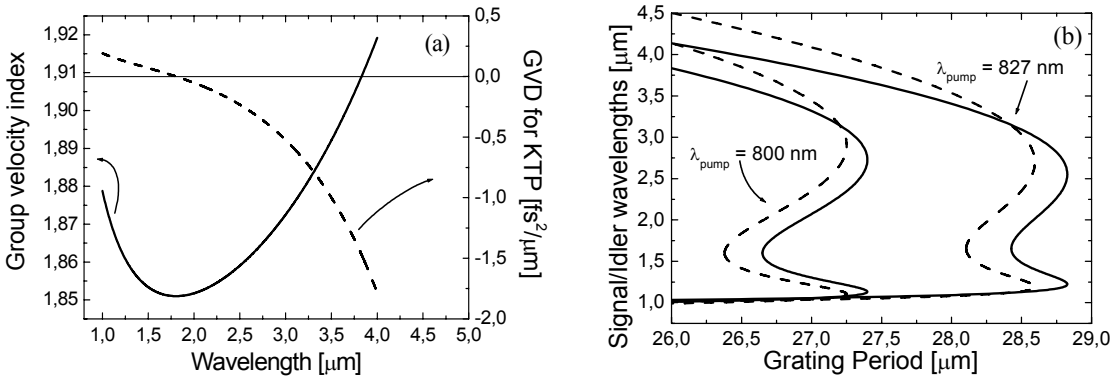

Fig. 5.1. (a): group velocity index (solid) and GVD (dashed) as a function of wavelength for KTP. Zero-GVD is at 1.803 μm, when using reference [108] in the Sellmeier expansion. (b): phase matching curve for two different Sellmeier expansions and the pump wavelengths 800 nm and 827 nm, respectively. Dashes: Sellmeier expansion according to Fradkin *et al.*[109] Solids: Sellmeier expansion according to Kato *et al.*[110]

most accurate Sellmeier expansions for KTP, the zero-GVD can be calculated to around 1.8 μm,[96,97] see Fig. 5.1 (a). In order to access ultrabroad bandwidths the pump wavelength should be chosen so that it is half the zero-GVD, i.e., at around 900 nm. However, in view of Fig. 5.1 (a), this wavelength is perhaps not the most favourable for generation of the broadest OPG bandwidth. The reason for this is that the group velocity index increases rapidly when the idler wave reaches the mid-IR absorption band. Consequently, this is also seen in the GVD curve. In other words, the pump wavelength should be slightly shorter, more in the region of 800 nm and 850 nm. Furthermore, it is evident from Fig. 5.1 (b) that the discrepancy between different Sellmeier expansions in this region causes uncertainties when designing the QPM periods. Therefore, it was necessary to experimentally map this region for several QPM periods and pump wavelengths. The goal was to find the right combination of grating period and pump wavelength for generation of the broadest possible parametric gain.

For the work described in article [VI] we fabricated six periodically poled crystals, five of those were PPKTP with the periods Λ = 29.5 μm, 28.5 μm, 28 μm, 27 μm and 26.3 μm,

respectively, while the sixth one was a PPRTP with the period $\Lambda = 25.7$ μm. All the crystals had the dimensions 8x5x1 mm^3 (along the x, y, z crystal axes, respectively) and were left uncoated. The pump source, a 1 kHz amplified Ti:Sapphire system, delivered 1 ps pulses with a spectral width of about 0.8 nm, and the central wavelength could be tuned between 770 nm and 900 nm. The narrow-linewidth pump pulses where specifically employed in order to determine the optimum pump wavelength more accurately. The pump beam was loosely

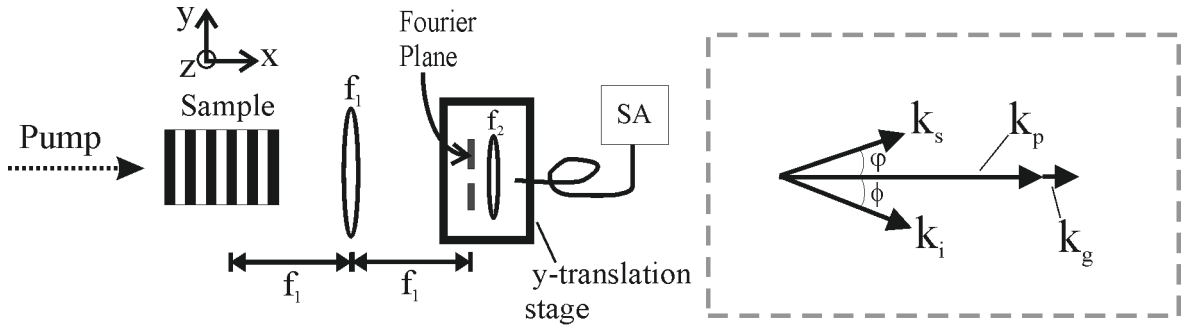

Fig. 5.2. To the left: the experimental setup. The output is Fourier transformed by the lens f_1 and the spatial distribution of the spectra can be observed by moving the translation stage in the y-direction. To the right: wave vector diagram for a pump beam which is parallel to the grating wave vector. The angular distribution of the signals and the idlers can be recorded in the Fourier plane.

focused in the sample. The parametric fluorescence is emitted over a range of angles with respect to the pump, as seen to the right in Fig. 5.2, and the angular distribution can be found from the equations (4.1) and (4.2). In order to determine the angular distribution of the emitted wavelengths, the parametric superfluorescent output was first Fourier-transformed by f_1. In the Fourier plane the angular wavevector distributions could be recorded on an optical spectrum analyzer by translating an aperture in the y-direction. The experimental setup is shown in Fig. 5.2. Each sample was characterized at pump wavelengths ranging from 777 nm to 850 nm and all OPG spectra were measured at a constant parametric gain at four-times the OPG threshold (~ 1 GW/cm^2). For more details on the setup, see article [VI].

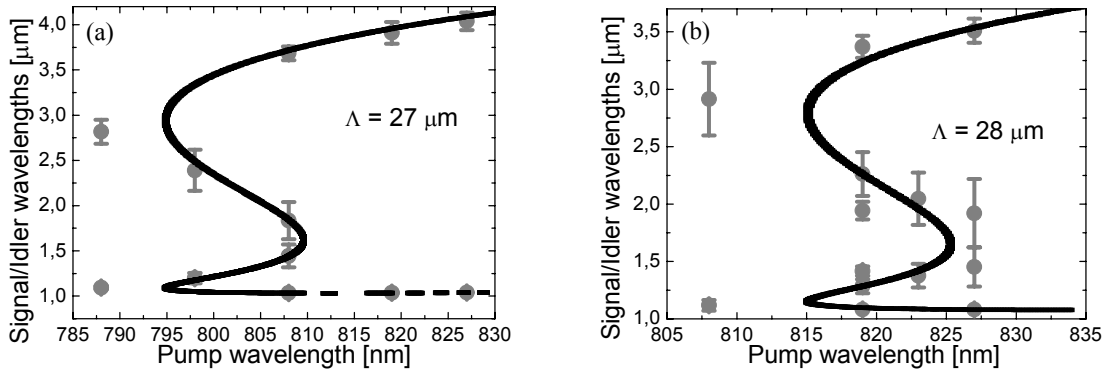

Fig. 5.3. Grey data points are measurements, with errorbars indicating the FWHM. The black lines are calculations using the Sellmeier expansion from Fradkin *et al.*[109] (a): 27 μm PPKTP crystal. (b): 28 μm PPKTP crystal.

In Fig. 5.3 are two wavelengths scans shown, which are conducted on the PPKTP periods $\Lambda = 27$ μm and 28 μm. The data points are measurements and the errorbars indicate the FWHM. The (quasi) solid lines are calculation of equation (2.14) (in the limit: $\Gamma << \Delta k/2$). At pump wavelengths below 800 nm the 27 μm-crystal generated bandwidths that were relatively small. For instance, going from 788 nm to 798 nm the signal bandwidths (central wavelengths 1100 nm and 1200 nm) increased from 40 nm to 110 nm (FWHM), respectively. Degeneracy

for this particular crystal was found at pump wavelength of 808 nm, and a signal bandwidth of 254 nm with a central wavelength around 1440 nm could be measured. However, the broadest spectral bandwidths was found for the 28 μm-crystal when pump at 827 nm. The parametric gain extends from 1080 nm to around 3800 nm, while the FWHM bandwidth was close to 1000 nm. The spectra for 28 μm-crystal pumped at 823 nm and 827 nm are depicted

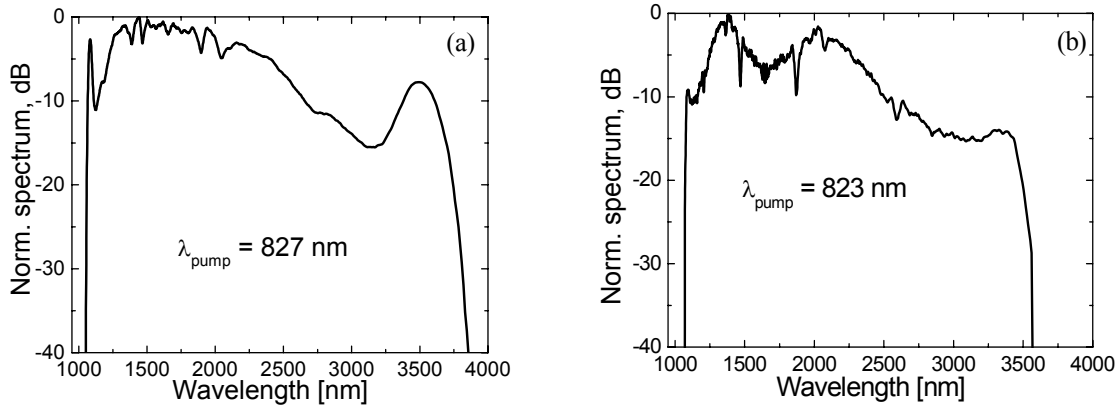

Fig. 5.4. Recorded spectra for the 28 μm PPKTP crystal at the pump wavelengths 827 nm, (a), and 823 nm, (b). The latter spectrum was recorded with a 3 mm aperture positioned 100 mm after the crystal, at four times above threshold.

in Fig. 5.4. The signal bandwidths for the PPKTP crystals in collinear propagation direction are summarized in Table 5.1. The 25.7 μm PPRTP crystal showed similar tuning behavior as the 26.3 μm PPKTP crystal.

λ_p / Λ	788 nm	798 nm	808 nm	819 nm	823 nm	827 nm	842 nm	849 nm
26.3 μm	1012/15	1005/6	1008/8	1019/7	N/M	1024/10		
	1193/120	1486/277						
27 μm	1094/40	1198/114	1035/12	1036/17	N/M	1040/13		
			1444/254					
28 μm	N/P	N/P	1118/93	1082/20	1377/206	1082/20		
				1416/82		1453/342		
28.5 μm	N/P	N/P	N/P	1197/87	N/M	1266/186	N/M	1103/16
29.5 μm	N/P	N/P	N/P	N/P	N/P	N/P	1287/107	1218/40
								1569/195

Table 5.1. Valid for collinear direction and PPKTP. First row is the pump wavelength and the first colon is the grating period of the PPKTP crystals. The numbers in the table indicates the central signal wavelength / the FWHM bandwidth in nm, i.e., $\lambda_0/\Delta\lambda$. N/P: no phase matching. N/M: not measured.

Next, the noncollinear generated spectra were studied. A well known fact is that the broadest parametric bandwidth to date has been obtained in short BBO crystals deployed in noncollinear OPAs.[94,98] However, this broad bandwidth is only accessible when the GVM is continuously geometrically compensated. In our case, we found noncollinear angles where the signal output showed angular dispersion-free operation over the entire spectrum. In Fig. 5.5 (a) the noncollinear phase-matching equations (4.1) and (4.2) are solved for three cases, using the Sellmeier expansions derived by Kato *et al*.[97] Two of them has close to angular dispersion-free signal distribution ($d\theta/d\omega \approx 0$), whereas the third one has a chirped angular dispersion ($d\theta/d\omega < 0$). Indeed, these properties were experimentally verified by moving the

aperture along the y-axis in the Fourier plane (see Figs. 5.2). Two of the spectra that were spatial invariant in the Fourier plane are depicted in Figs. 5.5 (b) and (c); at an external noncollinear angle of 24 mrad and 52 mrad, the parametric signal bandwidths of 60 THz and

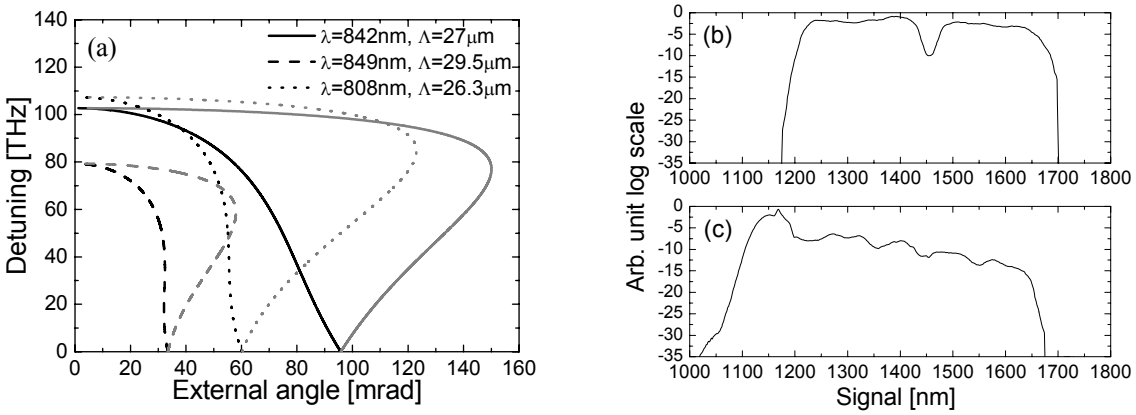

Figs. 5.5. (a): calculated noncollinear phase-matching curves when detuned from degeneracy as a function of the external angle. Black curves: signals. Grey curves: idlers. Dashes: λ_{pump} = 849 nm, Λ = 29.5 μm. Dots: λ_{pump} = 808 nm, Λ = 26.3 μm. Solids: λ_{pump} = 842 nm, Λ = 27 μm. (b): close to zero-angular distribution spectra. Top view: φ_{ext} = 24 mrad, λ_{pump} = 849 nm, Λ = 29.5 μm. Bottom view: φ_{ext} = 52 mrad, λ_{pump} = 808 nm, Λ = 26.3 μm.

65 THz were obtained, respectively. In the case of 27 μm-PPKTP crystal pumped at λ_{pump} = 842 nm, the spectral distribution was fairly linearly spaced around the central external angle φ_{ext} = 70 mrad, which corresponded to the wavelength 1290 nm. The generated signal spectrum extended from 1180 nm to 1500 nm, corresponding to the external angles φ_{ext} = 58 mrad and 82 mrad, respectively. As seen from Fig. 5.5 (a) the close to zero-angular dispersion observed for the signal in these noncollinear OPGs does not apply for the idler band (grey curves).

During the course of the experiments we found that the PPRTP with the period of 25.7 μm performs almost identically to the PPKTP with the QPM periodicity of 26.3 μm. Keeping in mind that the dispersion curves of KTP and RTP are to a large extent parallel to each other, one can easily deduce the proper periodicity for this isomorph from the PPKTP results reported here. Note that these results apply when the pump propagation direction is parallel to the grating wavevector.

In this study, the Sellmeier expansion derived by Fradkin *et al.*[96] was better suited for calculating collinear propagation of the constituent waves, whereas Kato's *et al.*[97] expansion concurred better with noncollinear signal and idler propagation. Nevertheless, the accuracy of these expansions around degeneracy is still not adequate. However, with the results from this investigation it will be possible to fabricate PPKTP and PPRTP for broadband applications using Ti:sapphire laser as a pump source.

5.2 Tunable Parametric Amplification

Tunable picosecond (ps) pulses in the infrared (IR) spectral region are desired in many spectroscopic applications within medical, biological, and material science. Since it gives unique possibilities to fingerprint specific molecules or atoms in different samples, and also

measure the dynamics of molecule in a non-invasive way, such as radiative lifetimes. In this study, which is described in article [VI], two ways of spectral manipulation are investigated. First we investigated pulse-stretching in a dispersion line and, secondly, a zero-dispersion arrangement.

The experimental setup for the temporally seed-stretching arrangement is depicted in Fig. 5.6. The setup consists of two uncoated PPKTP crystals with the grating periods 28 μm and 26.3 μm, respectively. The former PPKTP crystal has proven very useful as a broadband seed source [see Figs. 5.4], whereas the 26.3 μm PPKTP crystal is used in a noncollinear OPA scheme. A noncollinear OPA setup was chosen, since it facilitates seeding arrangements and enables easy double pass configuration if needed.The pump beam is split in a 12:88 ratio, where the 12 % is directed to the OPG stage, while the remaining pump is propagating through a delay-line and synchronized with the seed in the OPA stage. At both stages, collimated beams were formed through the PPKTP crystals by the telescopes: f_1-f_2 and f_1-f_3. Even though the 28 μm crystal provides ultrabroad bandwidth, here, we only use the signal part of the spectrum, i.e., 1080 nm to 1650 nm. The seed's transversal beam parameter, M^2, is improved by inserting an aperture after the collimating lens f_3. Moreover, the spatially filtered

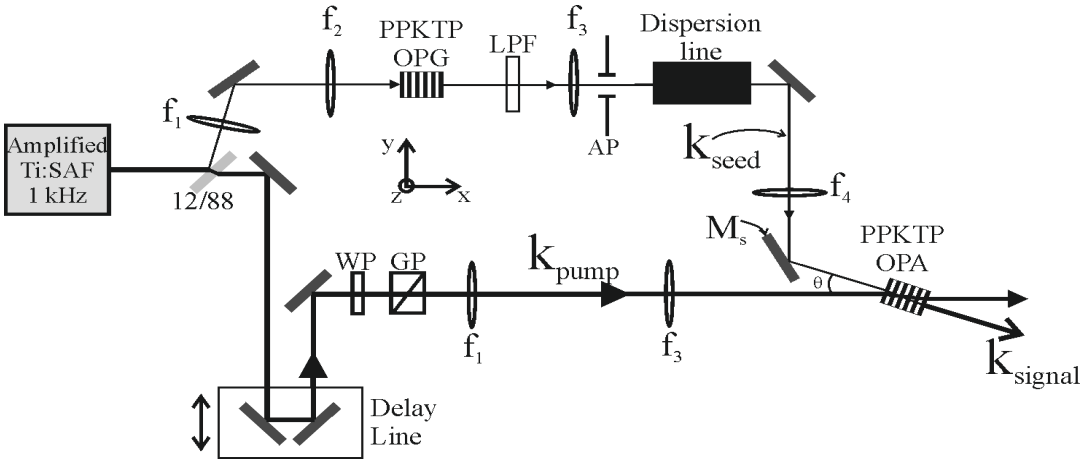

Fig. 5.6. The experimental setup consists of an OPG-stage (top) and an OPA-stage (right bottom). The pump for the OPA-stage is delayed and the power output is adjusted with the λ/2-wave plate (WP) and the Glan polarizer (GP). The telescopes with the lenses: f_1-f_2 and f_1-f_3 (f_1 = 500 m, f_2 = 50 mm, and f_3 = 100 mm), forming the beam radii of 300 μm and 600 μm (e^{-2} intensity) inside the OPG and OPA crystals. The pump wavelength is filtered out after the OPG by the long pass filter (LPF). The seed is then collimated by f_3. The dispersion line consists of three SF6 glass slabs and one SF8 glass slab, each one with an equal length of 75 mm. The seed is finally focused with f_4 = 250 mm into the OPA.

seed is then sent through a dispersion line, which consists of a 30 cm long glass slab. Two-thirds of the length was SF6 glass and one-third was SF8 glass. In order to support amplification of the whole seed's spectrum, the 26.3 μm PPKTP OPA crystal was rotated clockwise at an angle of 22 degrees in respect to the x-axis (see Fig. 5.6). At this crystal angle the cone shaped parametric fluorescence is emitted at an external angle of ~63 mrad. This crystal-rotation angle (22 degrees) would approximately correspond to the solid curve in Fig. 5.5 (a) that shows an angular chirp in the output spectrum.

The OPG was pumped at 27 mW and after the LPF filter, the spatial filtering and the dispersion line a seed power of 40 μW was measured, corresponding to 40 nJ of pulse energy. The acquired group delay time between the trailing edge at 1100 nm and the leading edge at 1650 nm of the seed spectrum could be investigated by scanning the 1 ps long pump pulse over the seed's pulse. Through the dispersion line the seed pulse was stretched close to nine times, which can be seen in Fig. 5.7 (a). It was possible to tune the OPA from 1616 nm to close to 1100 nm, which was done by delaying the pump beam by 17 ps. As seen in Fig.

5.7 (b), the measured full-width at half maximum (FWHM) spectral bandwidths varied between 21 THz and 5 THz when going from degeneracy to 1100 nm. The reason for the variation in bandwidth is that the point of zero-group velocity dispersion (GVD) for SF6

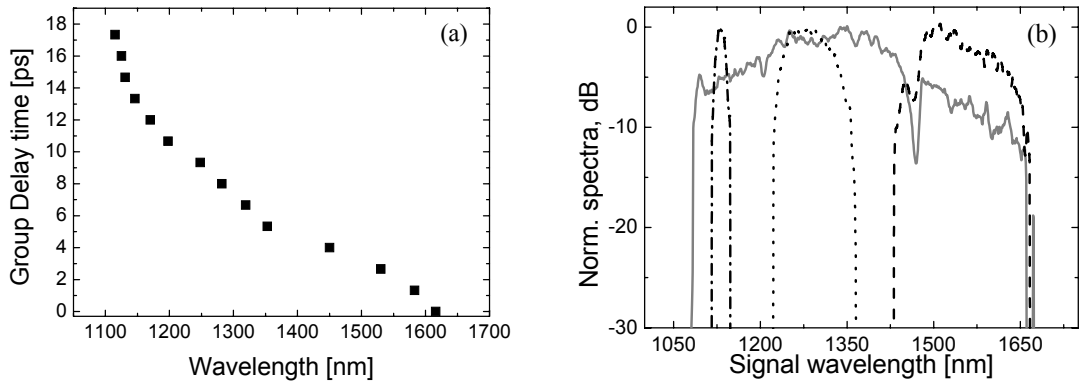

Fig. 5.7. (a): the amplified central wavelength as a function of the time delay of the OPA pump beam. The data points are measurements, while the solid line is calculations. (b): the output spectra. The grey curve is the OPG output spectrum. Dashed curve: at a delay of 2 ps. Dotted curve: at a delay of 8 ps. Dotted-Dashed: at a delay of 14.6 ps.

and SF8 are at 1.9 μm and 1.6 μm, respectively, and this result in poor temporal separation of the spectral components near degeneracy. Furthermore, the overall efficiency at a time delay of 8 ps was about 18 %, resulting in an amplification of 36 dB at incident pump energy of 86 μJ. The amplified seed had a central wavelength of 1280 nm and a full-width at half maximum (FWHM) spectral bandwidth of 87 nm. If we assume a flat spectral power distribution of the seed spectrum, then the resultant seed energy within the pump's envelope of 1 ps can be derived from Fig. 2 (a) and consequently approximate to 2.7 nJ. Similar power

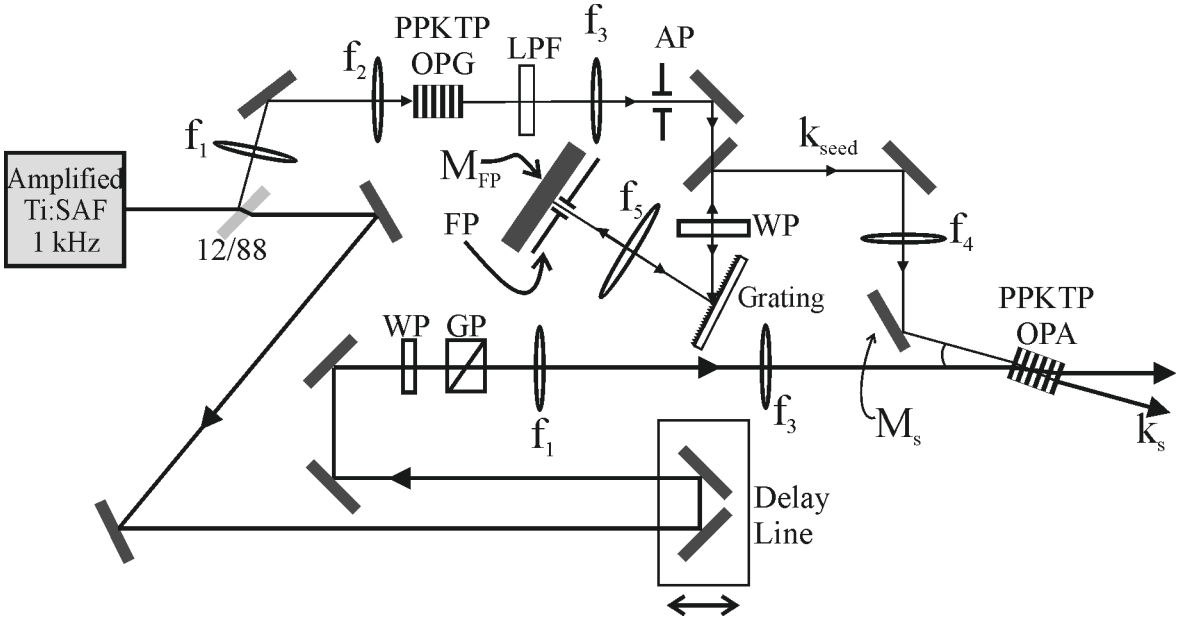

Fig. 5.8. The modified experimental setup. The OPA-stage is similar to that seen in Fig. 5.6. The OPG seed is spectrally manipulated in a zero-dispersion arrangement. The seed's polarization is rotated with the λ/2-wave plate (WP) in order to maximize the diffraction efficiency into the minus first-order of the grating (900 grooves/mm). The distance between the grating and the Fourier plane (FP) is $2\times f_5$ (f_5 = 80 mm, diam. 30 mm). The aperture (AP) in the FP was rectangular and had a width of 0.3 mm.

levels were observed at zero and 14 ps time-delays, corresponding to the central wavelengths 1616 nm and 1134 nm, respectively.

In order to increase the spectral control and to reduce the seed's spectral bandwidth, the dispersion line was removed and instead a zero-dispersion arrangement was inserted after the OPG. In Fig. 5.8 the modified experimental setup is seen. The zero-dispersion setup, also called the Fourier-filtering setup, consists of: a λ/2-wave plate (WP), a grating with 900 grooves/mm, a lens (f_5), a slit-aperture in the Fourier plan (FP), and an aluminium mirror. The distance between the grating and the mirror M_{FP} is $2\times f_5$, and consequently the grating's minus first-order is Fourier transformed by f_5. This means that, in the Fourier plane (i.e. at the mirror M_{FP}) the seed's spectrum is spatially distributed over the mirror M_{FP} and it is amenable for spectral filtering. Since the seed's spectral bandwidth is very broad, the angular dispersion of the grating also becomes very large and as a consequence the lens f_5 can not collect all the frequencies. However, by rotating the grating once the whole spectral range form 1080 nm to 1650 nm can be covered. At OPG pump energy of 27 μJ, the resultant Fourier-filtered seed power was approximated to 570 femto Joule (fJ). This was done by calibrating a fast InGaAs-detector with a power meter.

Narrow bandwidth tuning is achieved by translating the slit-aperture along the mirror M_{FP}. In this manner, a < 3 nm narrow bandwidth (FWHM) seed could be continuously tuned

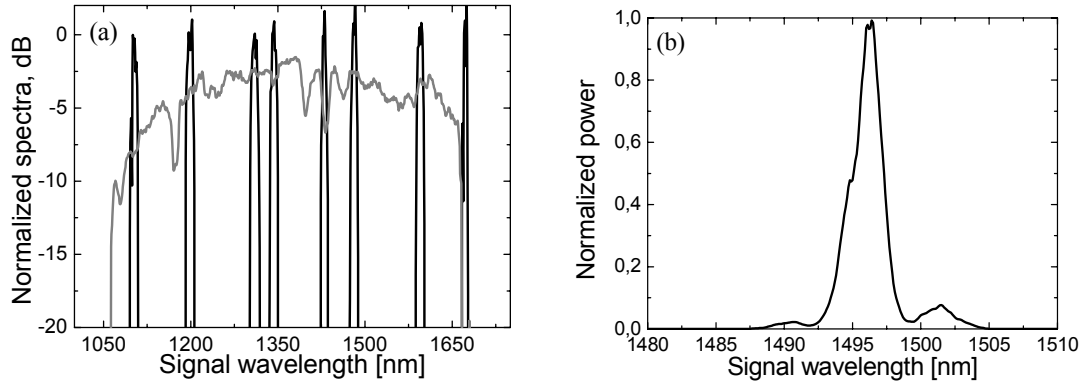

Fig. 5.9. (a): grey curve is the OPA crystals gain spectrum. Black curves: tuning of the seed by moving the aperture in the FP. (b): single-pass amplified spectrum. The central wavelength of 1497 nm, with a preserved bandwidth of 2.2 nm (FWHM). Diffraction-limited spectrum, due to the slit-aperture in the Fourier plane.

from 1080 nm to 1650 nm. The seed spectra are depicted in Fig. 4 (a) where the grey curve is the parametric gain spectrum of the 26.3 μm PPKTP crystal used in the OPA, while in Fig. 5.9(b) is a zoomed-in amplified spectrum of the signal wavelength at 1497 nm. The latter spectrum is recorded at OPA pump pulse energy of 50 μJ and the corresponding amplified signal (idler) energy was 2.7 μJ (2.2 μJ), same energies were found throughout the tuning range. This corresponds to a parametric gain of 67 dB and an overall efficiency of 10 %. As evident from Fig. 5.9 (b), the spectral bandwidth of 2.2 nm (FWHM) was preserved even after the amplification. The spectrum has the typical Fraunhofer diffraction pattern of a single slit.

To further increase the power level, a double-pass configuration was constructed by re-using the undepleted OPA-pump. Fig. 5.10 illustrates this arrangement. The undepleted pump and the signal are imaged off-axis with a lens, f_3, in order to displace the constituent beams when sending them back for a second pass amplification through the OPA PPKTP crystal. The distance between the PPKTP and the mirrors, M1 and M2, are $2\times f_3$, where M1 is mounted on a translation stage for temporal synchronization between the pump and the signal.

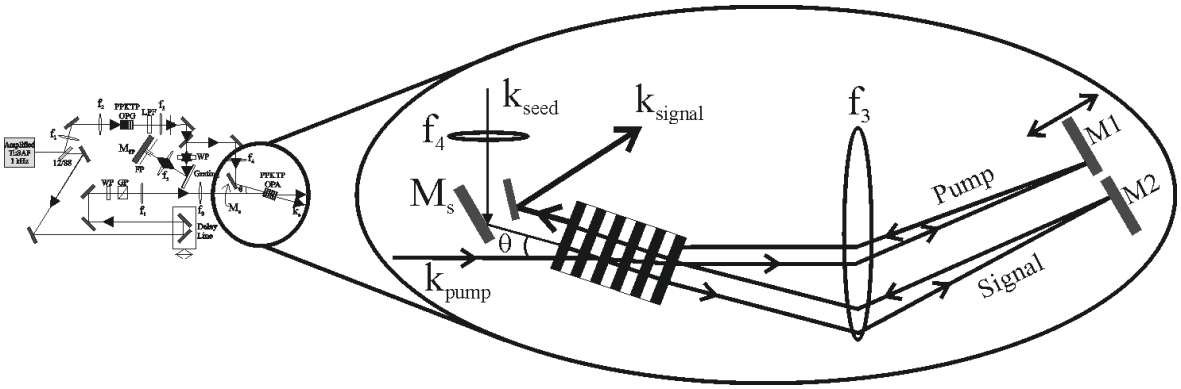

Fig. 5.10. Second-pass experimental setup. The signal and the pump propagate off-axis through the lens f_s and the mirrors M1 and M2 displaces the beams when returning for a second-pass through the PPKTP crystal.

Since the signal, on the return path, is displaced, a mirror can be inserted in the beam path to couple out the double-passed signal. The second-pass amplification increases the overall efficiency to 20 %, generating signal (idler) pulse energy of 6.5 μJ (5.3 μJ), as seen in Fig. 5.11 (a). Furthermore, in Fig. 5.11 (b), the spectra from a seeded and an unseeded double-pass through OPA are seen. As seen, the APF is almost completely suppressed when the OPA is seeded. A small amount of the fluorescence is still amplified, however, at a -25 dB lower power level. For more details regarding the setups and further discussions, see article [VI].

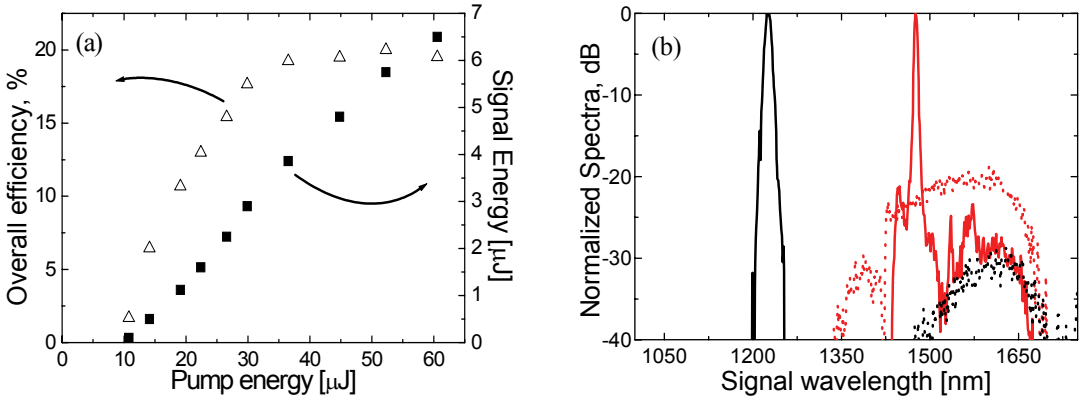

Fig. 5.11. (a): overall efficiency and signal energy as a function of incident pump energy. (b): Spectra at pump energy of 60 μJ. Dotted curves - unseeded double-pass OPA. Solid lines - seeded double-pass OPA.

To conclude, we demonstrated narrow bandwidth picosecond PPKTP OPA that was continuously tunable between 1100 nm and 1650 nm. The seed source was an ultrabroad bandwidth-generating PPKTP OPG and, due to the broad spectrum, the seed was spectral manipulated in order to supply narrow bandwidth spectrum to the OPA. Two different bandwidth narrowing techniques were investigated: temporal broadening through a dispersion line and Fourier-filtering. The latter technique supported less than 0.3 THz (FWHM) bandwidths, which was preserved through the amplification process in the OPA and throughout the whole tuning range. In order to increase the conversion efficiency of the OPG-OPA system, we re-use the undepleted pump in a second-pass through the OPA PPKTP crystal. In doing this, a parametric gain of 70 dB could be measured. For a total pump energy-budget of 100 μJ to the whole system, a signal (idler) output energy of 6.5 μJ (5.3 μJ) was achieved, corresponding to a total overall conversion efficiency of 12 %. It should be noted that this PPKTP OPG-OPA arrangement should achieve same amplification factors in higher-

repetition rate picosecond systems. For instance, a typical Ti:Sapphire regenerative amplifier operating at 150 kHz repetition rate provides pulse energies of about 8 μJ. In order to achieve same amplification ratio the pump beam radius in the OPG and OPA PPKTP crystals have to be reduced by approximately a factor of 3.5 down to 86 μm and 171 μm, respectively.

Chapter 6

Application – Biological Sensing

Laser technology is widely used in the field of biochemistry and biotechnology for detection and characterization of biomolecules. Laser induced fluorescence (LIF) techniques are applied in studies of everything from protein folding to DNA sequencing. In this work the UV-excitation is targeted at some specific building blocks of proteins that have natural fluorophores, such as tryptophan (Trp) and tyrosine (Tyr).[1] These two amino acids have their excitation peak around 280 nm, while their emission peaks are at 355 nm and 300 nm, respectively. In general, protein molecules and nucleotides, fluoresce when excited with light in the region 280 - 340 nm.[99] Obviously, when studying biological particles there will be more than one fluorophore and excitation wavelength present; thus, by tuning the wavelength to, for example, 340 nm, nucleotides such as NADH (involved in the cell metabolism) can be excited.[99] With this information we can assume that the spectral response from a protein (or nucleotide) has specific signatures, which can be used for classification. However, in order to produce fingerprint signatures of a bacterium, several different excitation and emission wavelengths must be scanned in order to thoroughly investigate its fluorescence signature. That is, for this kind of classification to be reliable and fast, a tuneable or multi-wavelength UV-laser source and an efficient detection system are needed.

In recent years the detection of biological warfare agents (BWA) has become a high-intensity research field and has been the topic for several conferences.[100,101] The overall goal is to be able to detect BWA in a fast, sensitive, and reliable way. The main reason for this, is that even small amounts of biological agents can infect a human and still be undetectable for the available biosensors.[102] Common used detectors are immunoassay-based, and they can take up to 30-45 min before identification is completed and still the sensitive of theses detectors are very poor.[103] Different detection systems based on LIF has been developed, such as the Fluorescence Aerodynamic Particle Sizer (FLAPS)[104] and the Wide Issure Bio-aerosol Sensor (WIBS2).[105] However, the former system uses only one excitation wavelength, which will not give a accurate measurement; while the WIBS2 system is using fragile Xenon lamps, which needs additional filtering and precision optics.

In our work we have constructed a UV-laser sources which enables emission of two or more wavelengths in the above specified spectral region and a detection system on the photon level, with good spectral resolution. The projected started with LIF experiments on biological particles in liquids and later we conducted experiments with bioaerosol.

The biological sensing work was conducted within the frame of two different projects, however, both with the same goal: detecting BWA through LIF spectroscopy. Initially, the work was founded and funded by the FOI - Swedish Defense Research Agency and all the published articles on biosensing by the candidate was within this project.[VII,A1,A2,A4,A5,A7] The gained knowledge was then transferred to the European consortium FABIOLA, where the work on detecting BWA continued. In this chapter I will first summaries the work done with

FOI and, thereafter, the work done within the FABIOLA consortium. The focus will be on the development of the UV source.

6.1 Low frequency – The Ultraviolet Laser Source

The frequency converting unit developed here consisted of a PPKTP parametric oscillator with intracavity sum-frequency mixing (SFM) in a BBO crystal. The pump source was also developed within the project, consisting of a diode pumped passively Q-switched Nd:YAG laser. This whole system fitted on a 40×60 cm^2 breadboard. The frequency converting processes can be described in a step wise manner:

(i), the 1064 nm output from the Nd:YAG laser is frequency double to 532 nm by a PPKTP crystal.

(ii), the 532 nm is used to pump the PPKTP OPO, which generates a signal between 610 nm to 940 nm. The output signal is tuned by chancing the grating period of the PPKTP crystal.

(iii), the signal and the undepleted pump is then sum-frequency mixed in a BBO crystal in order to generate ultraviolet radiation between 285 nm and 345 nm.

The output was then used for spectroscopic measurements on non-pathogenic agents. The construction of this step-wise tunable parametric device and the passively Q-switched pump-source will be topic of this section.

6.1.1 Beam shaping of a Diode Bar and Construction of a pulsed Nd:YAG Laser

Within the FOI-project a passively Q-switched Nd:YAG laser was especially developed for pumping the frequency conversion unit (described later in Section 6.1.2). The experimental setup is seen in Fig. 6.1. The laser medium was pumped by a fast-axis (FA) collimated quasi-CW diode-laser bar (QCW), with the bar dimensions 1 μm×10 mm. Due to the highly

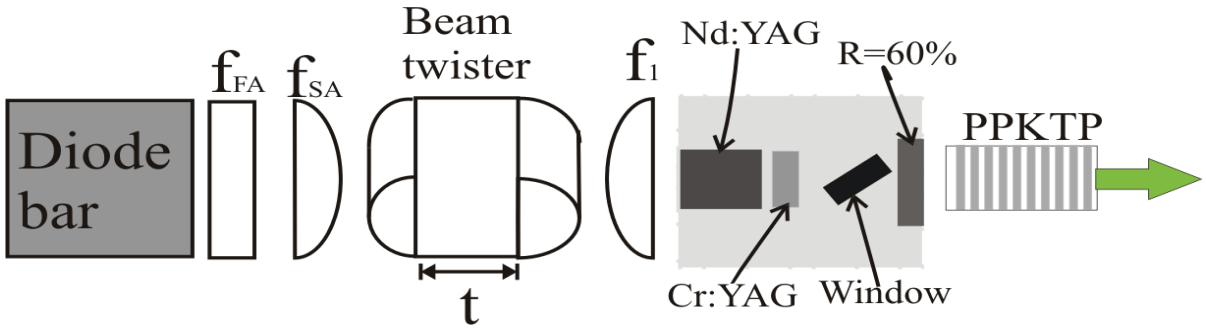

Fig. 6.1. Diode-pumped Q-switched Nd:YAG laser setup. The output from the QCW diode bar was mode converted from an astigmatic beam into a homogenous beam through the so called beam twister. The 1.064 μm output was frequency doubled immediately after the output mirror in a PPKTP crystal.

astigmatic pump profile a mode converter was used; twisting the astigmatic beam into an axially more homogeneous irradiance profile.[106] With two cylindrical lenses with fast and slow axis (SA) foci of f_{FA} = 50 mm and f_{SA} = 30 mm, respectively, a focus was formed on the front surface of the beam twister. The beam twister was rotated at an angle of $\alpha = 45°$ in respect to the transversal fast-axis and had the shape of a thick cylindrical lens with radius of curvature of r = 5 mm and the thickness of the centre plate t = 16.6 mm. The nearly symmetric beam was focused with a lens f_l = 10 mm to a beam radius of 1 mm (e^{-2} intensity) inside the laser medium. For more details regarding the mode converter see article [VII].

The Nd:YAG crystal was 4 mm long with a diameter of 5 mm and HR-coated on the left side (see Fig. 6.1) and AR-coated on the other side for 1064 nm and the 808 nm pump was transmitted through. Here we used a plane output mirror with a reflectivity of 60 % at 1.064 μm. Pulsed operation was provided with a Cr:YAG saturable absorber, with an initial transmission of 34 %. This generated pulses of 2.3 ns (FWHM) at 100 Hz, an average power of 130 mW and an optical-to-optical efficiency of nearly 10 %. The beam-quality parameter, M^2, and beam radius was measured to 1.3 and 390 μm (e^{-2} intensity), respectively. In order to generate 532 nm radiation a 3 mm long PPKTP crystal designed for second harmonic generation (period, Λ = 9.01 μm), was placed in front of the output mirror and kept at a temperature of 22 ˚C. A 50 % optical conversion efficiency was measured and a shortening of the pulse to 1.8 ns was observed, while the M^2-value was the same. The pulse shortening is a consequence of use of a second-order nonlinear process. The laser cavity and the doubling crystal were implemented on a monolithic copper block with a length of 35 mm. The total length of the laser, including diode bar, beam twisting and focusing optics, and PPKTP crystal was 25 cm.

6.1.2 Intra-cavity Sum-Frequency Mixing in an Optical Parametric Oscillator

The frequency converting unit we proposed and built consists of a linear SRO with intracavity SFM and is pump by the laser described above. The experimental setup is depicted in Fig. 6.2. It consists of an incoupling mirror, a PPKTP crystal, a type-I (ooe) BBO crystal, a dichroic mirror and to close the cavity, an output mirror. The cavity mirrors were HR at the signal wavelengths and HT of the pump and the idlers. In this particular parametric device and with

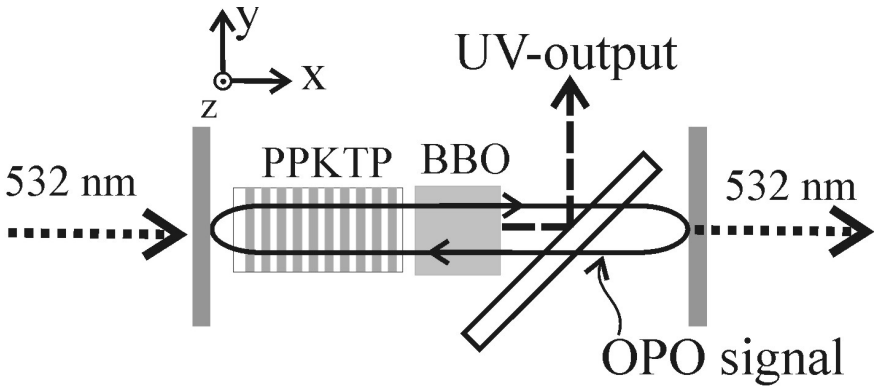

Fig. 6.2. The frequency converting unit. The PPKTP's signal is oscillating within the cavity and together with the undepleted 532 nm pump the waves are SFM in the BBO crystal. Consequently, the generated UV-radiation is coupled out of the cavity by the dichroic mirror.

the pump at 532 nm, it is possible to generate any wavelength between 285 nm and 345 nm with simple grating engineering. However, in article [VIII] the grating periods $\Lambda_1 = 12.77$ μm and $\Lambda_2 = 9.1$ μm, respectively, were chosen. These PPKTP crystals generate the signals wavelengths 652 nm and 965 nm, respectively. The 5 mm long BBO crystals were cut and polished for BPM between the signals and the undepleted pump. The dichroic mirror coupled out the UV-radiation from the cavity while transmitting the signals and the pumpwaves. The entire OPO-SFM cavity was only 26 mm long. The output spectra shown in Fig. 6.3 (a) have rather different bandwidths. The reason being that the 965 nm signal is approaching

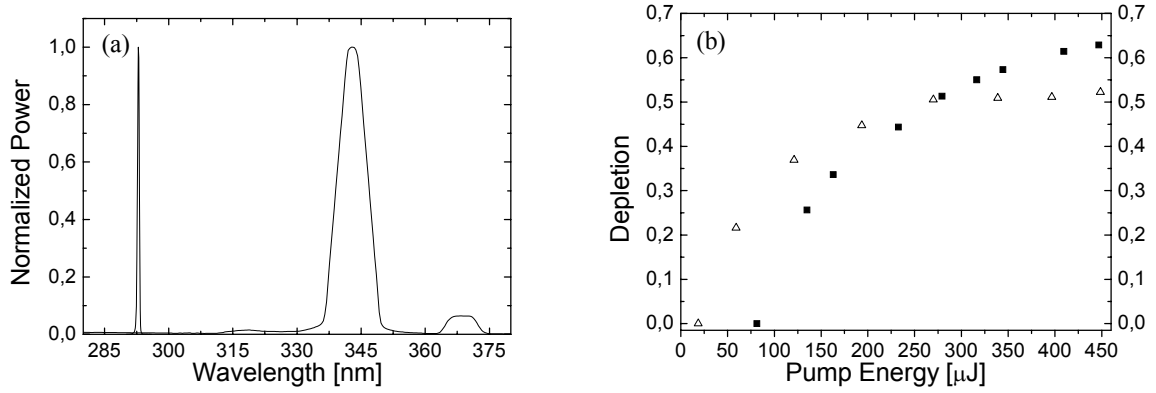

Fig. 6.3. (a): UV spectra. SFM between the generated signal and the undepleted pump. The 293 nm corresponds to SFM between 652 nm and 532 nm, while 343 nm to SFM between 965 nm and 532 nm. (b) OPO depletion measurements. Triangles: signal at 650 nm. Squares: signal at 965 nm.

degeneracy and its bandwidth becomes broad, see Fig. 3.3 and equation (2.16). The small peak to the right of the 343 nm-peak, is the SFM between the undepleted pump and the idler. In the case of generating 343 nm, it would be beneficial to replace the dielectric output coupler with a bulk Bragg grating, so that the efficiency would be improved in the SFM-stage. Even so, the measured depletions were as high as 63 % and 52 % for the 940 nm and 650 nm OPO, respectively. The depletion measurements are shown in Fig. 6.3 (b). The conversion efficiency from 532 nm to UV was close to 7 % for both cases. The output power at 343 nm and 293 nm, for pump pulse energy of 400 μJ, were 26 μJ and 28 μJ, respectively, for more details see article [VII].

6.2 Detecting Biological Particles

The detection system was developed by P. Jonsson *et al.* at FOI - Swedish Defense Research Agency.[105] In short the system consists of a 32 channel linear PMT-array (Hamamatsu) inserted in a spectrograph by Oriel. The fluorescent light from the biological particle was coupled into a quartz fiber and recorded through the constructed spectrometer. The non-pathogenic samples were prepared by the FOI in a NaCl-solution. In Fig. 6.4 a typical read-out from the linear PMT-array is shown. Fig. 6.4 (a) is Ovalbumin with the concentration 48 μg/ml, while Fig. 6.4 (b) is *Bacillus globigii* (BG) with the concentration 16 μg/ml. This kind of different emission characteristics can then be used for classification of biological agents. It will, most probably, not be possible to identify a biological particles by using LIF spectra only.[102] However, in conjunction with e.g. immunoassay-based sensors it will be possible. Thus, the constructed UV laser, seen in article [VII], is one step in the direction of

an early-warning system of BWA. The work conducted on bacteria in liquid (NaCl solutions) within the frame of detection of BWA's has continuously evolved and have been the subject of several reports.[A1,A2,A4]

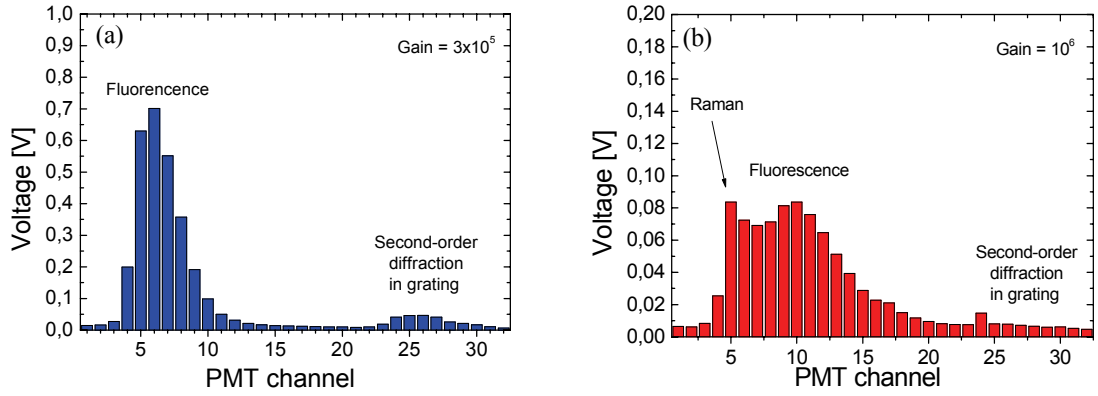

Fig. 6.4. (a): the protein ovalbumin is excited at 293 nm. It consists of the intrinsic fluorophore Tryptophan and has the characteristic emission spectrum. (b): BG samples excited at 293 nm. Due to the lower concentration the gain over the PMT-array is higher and the response is slightly lower. The channels (Ch) corresponds to the following wavelengths: Ch 3 to 293 nm; Ch 5 to 337 nm; Ch 8 to 380 nm; Ch 10 to 420 nm; Ch 15 to 500 nm and Ch 17 to 535 nm. Both graphs are courtesy of P. Jonsson at FOI.

Since the BWA are thought to be spread in air, it is desirable to monitor the air in cities, airports, post offices, etc.[102,103] However, this is particularly difficult, due to the presence of various natural occurring particles in the air (pollen, diesel soot, dust, etc). Nevertheless, at FOI they have constructed an aerosol chamber which lets us excite and record the emission from bioagents in a controlled way.[A5]

The system can be triggered by the presence of a particle in the excitation volume by a probe beam. Thus, when a particle is present the probe beam is scattered and detected with another PMT-array and a TTL pulse is generated. The UV-laser can then be triggered and subsequently excite the particle. Moreover, the size of biological particles was measured in order to have an additional orthogonal variable for classifying the sample. Similar systems using Xenon lamp and harmonics from Nd:YAG laser have been developed.[105,108]

The overall aim with both the liquid and aerosol based system is to have an early-warning system for detection of BWA and this was demonstrated. Both systems were based on excitation at 293 nm and 343 nm, while recording the fluorescent spectra. Within the project, a detection system based on a spectrograph and a PMT-array with sensitivity near the single-photon level was developed. Furthermore, the most severe restriction in both systems is the sensitivity level of the PMT array and was caused by background signals. These appear to originate from contamination of the sample cell glass walls by the used biological aerosols. However, by measuring the background signal this could be circumvented or at least significantly reduced. It seems that the wavelength 293 nm is close to optimum for excitation of Tryptophan, while the auxiliary wavelength adds additional fluorescence data to facilitate the classification of bioagents. However, it is not yet determined which or how many excitation wavelengths are needed in order to conduct a definite identification. With the QPM technique the UV wavelength can easily be changed in the present setup and it will be further investigated within the FABIOLA consortium.

6.3 The FABIOLA Consortium

The Western European Armament Organisation (WEAO) sent out a request for proposal for their Common European Priority Area 13 (CEPA 13) under the Research and Technology Project 13.13 (RTP 13.13) in April 2004.[109] The objective with this project is to develop an early-warning system for BWA attacks and demonstrate the feasibility to improve the detection of BWA using LIF. In order to send an application we formed a consortium together with 9 different companies and universities within the EU.[c] The name of the consortium became FABIOLA and it is originated from: Fluorescence Applied to BIOLogical Agents Detection. Our application was accepted and we started our work in January 2005. The candidate's role in this consortium is to assist in optical design matters, developing a tuneable UV-laser and integrate it into the detection system and project management.

6.3.1 High Frequency - The Ultraviolet Laser Source

In order to speed up the measurements a kHz-repetition rate laser is needed. Obviously, the laser should still have a good beam quality in order to have efficient conversion from IR to UV. Unfortunately, scaling up the repetition rate to kHz level in the laser described in article [VII] would degrade the beam quality severely and imposed stability issues, due to the increased thermal load. Thus, another type of laser architecture was needed and the candidate constructed a master oscillator power amplifier (MOPA) laser for this purpose.[17] The master oscillator is a passively Q-switched Nd:YAG laser, similar to that described in article [VII], however, here it is pumped by a fiber coupled 808 nm diode. The saturable absorber (Cr:YAG) had an initial transmission of 70 %. The amplifier stage consists of a Nd:YVO_4 (1 % atm. doping and 4 mm long) laser crystal pumped by a fast-axis collimated QCW laser diode bar from Jenoptik. The pump diode has an peak power of 100 Watts and is only focused in the slow axis into the Nd:YVO_4 crystal, emitting an elliptical area. The MOPA is shown in Fig. 6.5. The output from the master oscillator is passed through the Nd:YVO_4 crystal four times.

Characterization of the master oscillator was done separately. In the CW regime the cavity showed a slope efficiency as high as 51%, which indicates perfect mode-overlap between the pump (808 nm) and the oscillating 1064 nm waves. When inserting the saturable absorber (Cr:YAG) inside the cavity, pulse energies of 33 μJ in 3.2 ns long pulses could be achieved. The build-up time for the cavity was ~230 μs, with a measured pulse-to-pulse jitter of ± 5 μs. The transversal output parameter, M^2, was measured to 1.1.

The output from the fast-axis collimated QCW pump diode was focused with two cylindrical lenses (horizontal plane), having an effective focal length of ~13 mm. The input pulse energy to the amplifier was 33 μJ and after four passes through the amplifier and a gain of 15 was achieved, which corresponds to pulse energy of close to 500 μJ. The pulse length became slightly longer in the amplifications process and was measured to 3.5 ns. However, for stability reason the output pulse energy was limited to 400 μJ for 1 kHz repetition rate. The main reason for the instability was that the amplifier was lasing between the output coupler of the master oscillator and the Nd:YVO_4 crystal's back surface. However, long term

[c] Thales (France), Teletel (Greece), Dekati (Finland), Galileo Avionicas (Italy), Military University of Technology (Poland), Technical University of Tampere (Finland), Cobolt (Sweden), Umetrics (Sweden).

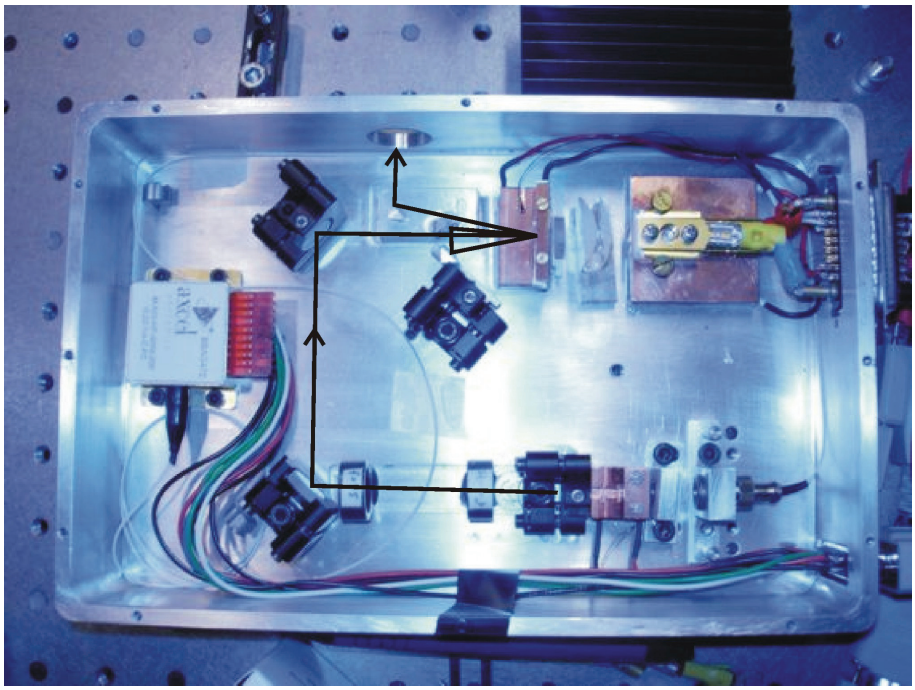

Fig. 6.5. The MOPA system was built into a tailored monolithic aluminium frame. Middle left: the fiber coupled 808 nm diode laser; its fiber is routed along the sides of the frame to the master oscillator. Bottom right: the master oscillator. Top right: the power amplifier. The seed is passed through the vanadate crystal four times. The hole in the top middle of the picture is the output of the MOPA laser.

measurements showed that peak-to-peak stability was around ± 4 % at a pulse repetition rate of 300 Hz.

The 1.064 μm output was frequency doubled in a 3 mm long PPKTP crystal with an efficiency of 50 %. Thus, close to 200 μJ could be used for frequency conversion to UV. The UV converting device, which is seen in Fig. 6.6 (b), was design to be stable and easy to use. Tuning was done be translating a multigrating PPKTP perpendicular to the propagating direction for the constituent waves. The PPKTP crystals used, had 3 gratings on each sample, which enabled fast tuning of the parametric device. In this way, the frequency conversion unit could be tuned between 285 nm and 345 nm. The crystals were manufactured by Cobolt AB (participates in the FABIOLA consortium) and were AR-coated. The corresponding spectra are seen in Fig. 6.6 (a). Furthermore, the OPO threshold and intracavity signal energies for the different crystal periods are ranging from 30 μJ to 100 μJ (532 nm) and 15 μJ to 55 μJ (signals), of the green pump beam. This indicates a slight variation of the quality of the PPKTP crystals. However, the UV pulse energies ranged from 4 μJ to 6 μJ. The lower pulse energies compared to what was observed in article [VII], first of all, are due to, lower pump energies and secondly, that the device can not optimize the position of the PPKTP crystal. The reason for this is that we wanted to have a stable and easy tuneable device and, unfortunately, the efficiency has to suffer. Although the intracavity signal energies varied, the OPO/SFM stage generates enough UV-radiation in order to conduct the spectroscopic measurements which are held at Military University of Technology in Poland (MUT).

The UV-laser is since October 2005 installed at MUT (Poland) and is used in LIF spectroscopic measurements on biological agents in aerosol and in liquids; however, detection in air is the main objective of this project. An additional feature of the FABIOLA aerosol

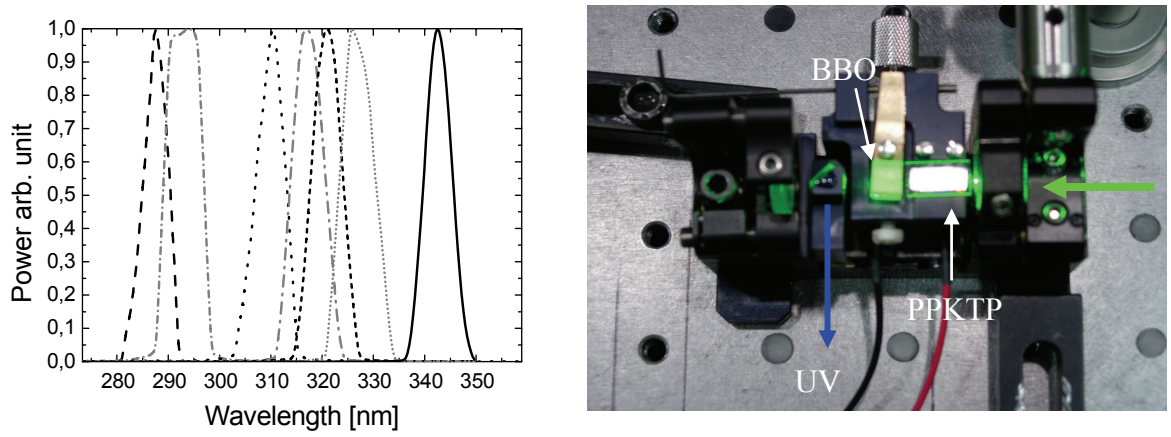

Fig. 6.6. (a): generated UV-wavelengths in the frequency conversion unit when pumped at 532 nm. Each wavelength is generated with a specific PPKTP grating. The grating period ranges from 13.5 μm to 9.1 μm, corresponding to signal wavelengths 630 nm to 970 nm (b): the frequency conversion unit.

chamber, compared to reference [105], is that it can concentrate predetermined particle sizes in a so called virtual impactor,[110] which is developed by Tampere University of Technology (Finland). The experiments on aerosol have just started and there are no results when this is written. Nevertheless, results on, for example, *Penicilium Chrysogenum* in liquid LIF experiments have been conducted with this high repetition rate laser seen in Fig. 6.5. In Fig. 6.7 are the emission spectra for different excitation wavelengths. From left to right are the excitations of: 285 nm, 293 nm, 320 nm, 325 nm and, finally, 340 nm. The excitation peaks are cut out from the spectra.

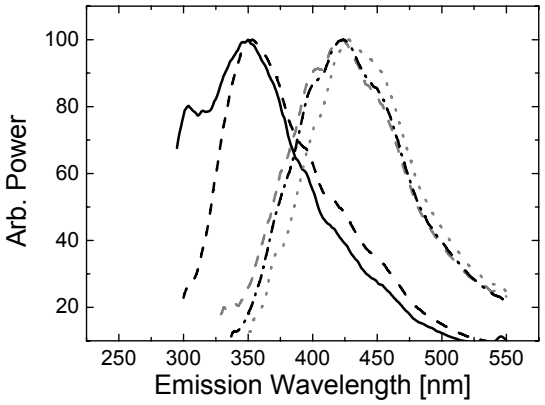

Fig. 6.7. The emission spectra of Penicilium Chrysogenum for different excitation wavelengths. The corresponding Black solid line: 285 nm; Dash black line: 293 nm; Dash grey line: 320 nm; Dash dot line: 325 nm; Grey dots: 340 nm. The spectra are raw data recoded by Dr. M. Kwasny at Military University of Technology, Warsaw, Polen.

The FABIOLA project time is extending over four years and within that time frame an early-warning BWA detection prototype should be developed. The prototype will be used in field tests at different locations in Europe, in order to characterize the ambient air. The reason for this is that the background air varies over the year and with location (pollen, pollution, etc) and this need to be investigated. With this particular device, the sensitivity level of detections of biological substances will increase.

Chapter 7

Description of Work and Author Contribution

Article I

Spectral and spatial limiting in an idler-resonant PPKTP optical parametric oscillator
M. Tiihonen, V. Pasiskevicius and F. Laurell
Opt. Comm. **250**, 207 (2005).

In this paper spectral narrowing and improvements of the spatial beam quality in a periodically poled $KTiOPO_4$ optical parametric oscillator was demonstrated. This was achieved by taking advantage of the inherently lower angular dispersion properties of the idler wave, compared to that of the signal wave. Thus, by letting the idler resonate in a noncollinear optical parametric oscillator cavity, the spectral output was decreased by a factor of 2 compared to a signal resonant cavity. Moreover, the spatial beam quality was significantly better of the idler wave, since diffraction was more pronounced in this case. The efficiency for both the signal- and the idler-resonant cases were close to 67 %.

Contribution by the author: The candidate, together with V. Pasiskevicius, designed the experimental setup and conducted the measurements. The derived theory and simulations, and writing of the paper were also done by the candidate and V. Pasiskevicius.

Article II

Narrowband bulk Bragg grating optical parametric oscillator
B. Jacobsson, M. Tiihonen, V. Pasiskevicius and F. Laurell
Opt. Lett. **30**, 2281 (2005).

This paper was the first report on using a bulk Bragg grating as an output coupler in an optical parametric oscillator. The Bragg grating works as a spectral filter and only reflects a predetermined wavelength with a narrow spectral bandwidth. This particular property is advantageous when operating a (near-)degenerate optical parametric oscillator, where the spectral bandwidth is typically broad. We showed that a periodically poled $KTiOPO_4$ parametric oscillator pumped at 532 nm and emitting close to degeneracy, had a spectral bandwidth of only 0.16 nm (full width half maximum); this is a decrease by a factor of 20 compared to using a conventional output mirror. With this device the efficiency was the same

as for the conventional mirror, however, the brightness of the optical parametric oscillator had increase drastically. Furthermore, the bulk Bragg grating can withstand peak high powers and is insensitive to temperature fluctuations. In a folded cavity the optical parametric oscillator could be tuned over 60 nm and maintain the same linewidth.

Contribution by the author: The candidate and B. Jacobsson designed and carried out the experiment. The idea for the bulk Bragg grating optical parametric oscillator was made by F. Laurell. The paper was written by the candidate and B. Jacobsson.

Article III

Noncollinear double-ring optical parametric oscillators with periodically poled $KTiOPO_4$
M. Tiihonen, V. Pasiskevicius, F. Laurell
Opt. Exp. **12**, 5526 (2004).

Here we showed a novel optical parametric oscillator design for spectral manipulation of the output beam. This was achieved by pumping a ring optical parametric oscillator from two opposite sides, which, consequently, supported two counter-propagating idler waves. The cavity could be tuned by rotating a single cavity mirror, between 1189 nm and 1267 nm. In order to manipulate the output spectra, one of the resonant idler waves were coupled out from the cavity by a grating, which was one of the cavity mirrors. The minus first-order diffraction from the grating was subsequently Fourier transformed and in the Fourier domain the generated spectral bandwidth could be spectrally filtered. This was either done by a stripe-mirror or inserting a beam block at different positions in the Fourier plane. When sending back the filtered idler, it propagated in the opposite direction and, hence, acted as a seed for the counter-propagating pump wave. The seeded optical parametric oscillator achieved efficiency of 45 % and in the case of a stripe-mirror in the Fourier plane the idler's spectral bandwidth was 56 GHz, compared to 1.43 THz when cavity was unseeded.

Contribution by the author: The candidate and V. Pasiskevicius designed the setup and conducted all the measurements. The derivation of the theory and writing the article were done by the candidate and V. Pasiskevicius.

Article IV

2D Quasi-Phase-Matched Multiple-Cascaded Four-Wave Mixing in a periodically Poled $KTiOPO_4$
M. Tiihonen and V. Pasiskevicius
Submitted to Optics Letter in May 2006

In this work we studied cascaded interaction in a double resonant periodically poled $KTiOPO_4$ parametric oscillator pumped by two mutually coherent laser beams. The two pump beams, with wavelength 1.064 μm, generated two independent signal beams in the 1.55 μm region. The pump beams were symmetrically launched at an angle into the cavity and were intersecting inside the $KTiOPO_4$ crystal. In the case of collinear cavity mode (cavity mirrors parallel to the crystal's end surfaces), the two generated signals wavelengths were equal, however, by rotating the cavity mirrors two different signal wavelengths was observed due to

the difference of the pumps' angle in respect to the resonator axis. Thus, two distinct, independent and tuneable signal wavelengths could be generated in the propagation direction of the resonator. Furthermore, the mutual coherence of the pump beams gave rise to an interference pattern inside the crystal and this particular feature can be viewed upon as a parametric gain grating. This grating works as an additional phase-matching component that facilitates coupling between the two independent signal, idler and pump wavelengths. At a specific noncollinear cavity angle this was observed as spectral sidebands in the signal and the pump region and the measured spacing was 1.5 THz around the constituent wavelengths. The origin of these sidebands is due to the first-order cascaded process through the $\chi^{(2)}:\chi^{(2)}$ interaction and are dependent on the angle of the intersecting pump beams, i.e., larger pump angle creates a denser interference pattern and thus larger frequency spacing. The dependence of the coherence properties on the optical parametric oscillation threshold were also investigated and explained.

Contribution by the author: The candidate designed the experimental setup and conducted all the measurements. The paper was written by the candidate and V. Pasiskevicius.

Article V

Ultrabroad Gain in an Optical Parametric Generator with periodically poled $KTiOPO_4$
M. Tiihonen, V. Pasiskevicius, A. Fragemann, C. Canalias, and F. Laurell
Accepted for publication in Applied Physics B in march 2006.

Ultrabroad bandwidths can be generated in a periodically poled $KTiOPO_4$ when pumped at half the wavelength of the zero-group velocity dispersion point. According to calculations this point is approximately around 1.6 μm for $KTiOPO_4$. However, the Sellmeier equation close to degeneracy is inaccurate and this in turn renders grating fabrication cumbersome. So, in order to map this region thoroughly we fabricated six different grating periods, which were pumped by an amplified picosecond Ti:Sapphire laser. The pump laser could be tuned between 770 nm and 900 nm. At a pump wavelength of 827 nm and a crystal with the period 28 μm, the collinear spectral bandwidth reached 115 THz, which extended from 1080 nm to 3800 nm in a single propagation direction. The largest noncollinear signal spectrum, with low angular dispersion, was observed for the 29.5 μm period crystal when pumped at 849 nm. The signal spectral bandwidth in this case was recorded to 64 THz. These bandwidths are the broadest possible bandwidths accessible in periodically poled $KTiOPO_4$ for collinear and noncollinear propagation directions.

Contribution by the author: C. Canalias and A. Fragemann fabricated the periodically poled crystals. A. Fragemann and V. Pasiskevicius constructed the experimental setup. The candidate and V. Pasiskevicius conducted the major part of the experimental campaign. Finally, the article was written by the candidate and V. Pasiskevicius.

Article VI

Broadly Tunable picosecond narrowband pulses in a periodically-poled $KTiOPO_4$ parametric amplifier.
M. Tiihonen, V. Pasiskevicius, and F. Laurell
Submitted to Optics Express in May 2006.

The knowledge gained in article [V] was used for constructing a tuneable picosecond optical parametric amplifier. The 28 μm period crystal from article [V] is pumped at 822 nm and is used as a seed source for the amplifier stage. The seed's output is first spectrally filtered in a zero-dispersion arrangement, resulting in a spectral bandwidth of less then 300 GHz. The narrowed seed is tunable over the spectral region between 1075 nm and 1655 nm and subsequently, amplified in a noncollinear periodically poled $KTiOPO_4$ crystal, with a period of 26.3 μm. A double-pass scheme is deployed and yields a small-signal gain of 70 dB when pumped at pulse energy of 60 μJ. The corresponding signal energy was 6.5 μJ and the total efficiency of the amplifier stage was close to 20 %. The same energy levels were found between 1157 nm to 1648 nm.

Contribution by the author: The experimental design and execution of the experimental campaign were done by the candidate. Later the candidate and V. Pasiskevicius wrote the paper together.

Article VII

Tailored UV-laser source for fluorescence spectroscopy of biomolecules
M. Tiihonen, V. Pasiskevicius, F. Laurell
Accepted for publication in *Optics and Lasers in Engineering*, March 2005.

A ultra-violet solid-state laser system was constructed, with the aim to enable detection of bacteria in liquids. The ultra-violet is reached through three different nonlinear processes. The pump source is a diode pump Neodymium-doped ytterbium aluminum garnet laser of own design. The diode bar's Hermite-Gaussian output beam was re-shaped into a homogenous output beam with a mode converting optical system. Moreover, a 50 % conversion efficiency of the 1064 nm output to 532 nm was achieved in a periodically poled $KTiOPO_4$; the 532 nm output was then used for pumping a periodically poled $KTiOPO_4$ parametric oscillator with a β- BaB_2O crystal capable of supporting intra-cavity sum-frequency mixing between the oscillator signal and undepleted 532 nm. In this compact and robust frequency converting unit the ultra-violet wavelengths 293 nm and 343 nm was generated, by deploying two different grating periods in the latter $KTiOPO_4$ crystal. The output was then successfully used for detection of non-pathogenic bacteria.

Contribution by the author: The candidate constructed the Nd:YAG laser system with advise from Dr S. Spiekermann. The frequency conversion unit was also design and constructed by the candidate. The spectroscopic measurements were done at the labs of Swedish Defense Agency (FOI) and were conducted by Dr P. Jonsson. The paper was written by the candidate.

Chapter 8

Conclusions

This thesis is dealing with novel parametric devices based on periodically poled $KTiOPO_4$ (PPKTP). Focus has been put on the spectral manipulation of bandwidths and output spectra, particularly linewidth narrowing and tuning behavior in optical parametric oscillators (OPOs), generator (OPGs) and amplifier (OPAs) have been invstigated.

In the case of singly-resonant OPOs (SROs), it has been revealed that the difference in angular dispersion of the signal and the idler can, in many circumstances, be used for bandwidth manipulation. Under the same pump conditions, i.e., same parametric gain, the idler-resonant, quasi-phase-matched (QPM) noncollinear SRO generates narrower spectral bandwidth as compared to the signal-resonant device. In fact, in our case, the idler-resonant cavity had two times smaller bandwidth than in the case of the signal-resonant one and both cases showed efficiencies of close to 70 %. This particular property can be utilised as the first step of bandwidth narrowing in SROs, which does not sacrifice the efficiency of the device. Further line-narrowing was accomplished by using an external element: the output mirror was replaced by a bulk Bragg grating. This simple design decreased the bandwidth by 20 times compared to a conventional mirror and still had high efficiency. The Bragg grating narrowed SRO is very attractive for spectroscopic applications, as well as for being a pump source for subsequent parametric interactions. This was actually the first report of an OPO with a bulk Bragg grating as an output coupler. Furthermore, in a double-ring OPO, one of the folding mirrors was replaced with a grating. The grating provided access to the resonant idler's spectrum through the minus first-order diffraction. In a zero-dispersion arrangement, the spectrum could be filtered in the Fourier plane and sent back into the cavity as a seed for the counter-propagating pump beam. This double-ring OPO could easily be tuned between 1190 nm and 1280 nm and, by inserting an aperture or stripe-mirror in the Fourier plane, the seed spectrum could be manipulated in an arbitrary way. We believe it should be possible with this novel filter design to measure the size of small objects fast and accurately. The resolution can easily be adjusted according to specifications, since it is set by the grating and the Fourier transforming lens. Furthermore, in distinct contrast to ordinary lasers, the spectral properties of a parametric device can be tailored by the pump geometry and, in the case of two pump beams, the mutual coherence plays a crucial role. In a two-pump-beam OPO, we have demonstrated the emergence of an additional degree of freedom in the QPM parametric interaction, due to a transversal gain grating produced by the interference of the two beams. This gain modulation enhances a cascaded $\chi^{(2)}$:$\chi^{(2)}$ four-wave mixing process and provides gain in angularly spaced spectral channels. These channels are seen as sidebands spaced 1.5 THz from the original signal, idler and pump waves. This concludes the studies made on linewidth narrowing techniques and spectral manipulations in OPOs. It shows that OPOs are

versatile and efficient light sources, which can be manipulated with respect to both the spectra and the bandwidth with simple tools, in order to fit a specific application.

In the thesis it has also been shown that it is possible to generate ultrabroad bandwidths in a collinear picosecond (ps) PPKTP OPG, where the parametric gain extended over three octaves. This is probably the largest spectral bandwidth generated in PPKTP, and it was done by first finding the wavelength of zero-group velocity dispersion for KTP and then pumping at half of this wavelength. Broad bandwidths in the mid-infrared region are attractive, for example, for the generation of few-cycle pulses, which can be used for pump and probe spectroscopy and also for generation of high-harmonics, so called soft x-rays, in the atto-second time domain. However, in this thesis, the ultrabroad output was spectrally manipulated in a Fourier-filter arrangement and used as a seed for an OPA. The filtered seed had a spectral bandwidth of 3 nm and could be tuned over the whole signal bandwidth, i.e., from 1100 nm to 1650 nm. The small-signal gain was 70.5 dB in a double-pass configuration, reaching 6.5 μJ of pulse energy at 1450 nm.

Finally, it was demonstrated that with parametric devices it is possible to construct a tunable ultraviolet light source, which, in this case, was used for detection of biological substances through fluorescence spectroscopy. The ultraviolet source could be step-wise tunable between 285 nm and 345 nm. Throughout the project time, no less than three sources were constructed for different end users. The ultraviolet lasers are used for characterising the fluorescence spectra of know biological agents in order to be able to classify them in a, so called, early-warning system, which can be used for monitoring the air in cities, post offices, airports, etc. Successful results were gained of biological particles both in liquid solution and in aerosol from.

It should be noted that the results obtained within this thesis are not only applicable to periodically poled KTP, the same type of results should be seen with, for example, periodically poled $LiNbO_3$ (PPLN). However, PPKTP's beneficial properties made it the preferred choice in the applications described here.

Keep it simple, straightforward and elegant
Professor Robert L. Byer thoughts on designing
lasers and parametric devices.

References

1. T. H. Maiman, Nature **187**, 493 (1960).
2. P. Franken, A. Hill, C. Peters, and G. Weinreich, Phys. Rev. Lett. **7**, 118 (1961).
3. J. A. Giordmaine and R. C. Miller, Phys. Rev. Lett. **14**, 973 (1965).
4. S. E. Harris, M. K. Oshman, and R. L. Byer, Phys. Rev. Lett. **18**, 732 (1967).
5. C. C. Wang and G. W. Racette, Appl. Phys. Lett. **6**, 169 (1965).
6. P. N: Butcher and D. Cotter, *The Elements of Nonlinear Optics*, Eds. P. L. Knight and W. J. Firth, Cambridge Studies in Modern Optics:9, Cambridge University Press, UK (1990).
7. R. W. Boyd, *Nonlinear Optics*, Academic Press, San Diego, USA (1992).
8. A. Yariv, *Quantum Electronics*, 3rd ed, John Wiley & Sons Inc, New York (1988).
9. D. A. Kleinman, Phys. Rev. **126**, 1977 (1962).
10. G. D. Boyd and D. A. Kleinman, J. Appl. Phys. **39**, 3597 (1968).
11. J. A. Armstrong, N. Bloembergen, J. Ducuing, and P. S. Pershan, Phys. Rev. **127**, 1918 (1962).
12. M. M. Fejer, G. A. Magel, D. H. Jundt, and R. L. Byer, IEEE J. Quantum Electron. **28**, 2631 (1992).
13. R. L. Byer and S. E. Harris, Phys. Rev. **168**, 1064 (1968).
14. S. E. Harris, Proc. IEEE **57**, 2096 (1969).
15. R. L. Sutherland, *Handbook of Nonlinear Optics*, Optical Engineering, Marcel Dekker Inc., New York (1996).
16. G. Cerullo and S. De Silvestri, Rev. Sci. Inst. **74**, 1 (2003). (see also references therein)
17. A. E. Siegman, *Lasers*, University science books, Sausalito, California, USA, (1986).
18. F. G. Colville, M. J. Padgett, and M. H. Dunn, Appl. Phys. Lett. **64**, 1490 (1994).
19. A. Piskarskas, V. Smilgevicius, A. Umbrasas, A. Fix, and R. Wallenstein, Opt. Commun. **77**, 335 (1990).
20. J. E. Bjorkholm, IEEE J. Quantum Electron. **QE-7**, 109 (1971).
21. J. M. Manley and H. E. Rowe, Proc. IRE **44**, 904 (1956).
22. S. J. Brosnan and R. L Byer, IEEE J. Quantum Electron. **QE-15**, 415 (1979).

23. D. Bedeaux and N. Bloembergen, Physica **69**, 57 (1973).

24. R. DeSalvo, D. J. Hagan, M. Sheik-Bahae, G. Stegeman, and E. W. Van Stryland, Opt. Lett. **17**, 28 (1992).

25. M. Zavelani-Rossi, G. Cerullo, and V. Magni, IEEE J. Quantum Electron. **34**, 61 (1998).

26. S. Holmgren, V. Pasiskevicius, and F. Laurell, Opt. Express **13**, 5270 (2005)

27. D.E. Spence, P.N. Kean, and W.Sibbett, Opt. Lett. **16**, 42 (1991).

28. M. H. Chou, I. Brener, G Lenz, R. Scotti, E. E. Chaban, J. Shmulovich, D. Philen, S. Kosinski, K. R. Parameswaran, and M. M. Fejer, IEEE Phot. Tech. Lett. **12**, 82 (2000).

29. E. Yablonovitch, C. Flytzanis, and N. Bloembergen, Phys. Rev. Lett. **29**, 865 (1972).

30. D. K. Cheng, "Field and wave electromagnetics", 2nd, Addison-Wesley, USA, (1989).

31. P. A. Franken and J. F. Ward, Rev. Mod. Phys. **35**, 23 (1963).

32. B. F. Levine, C. G. Bethea, and R. A. Logan, Appl. Phys. Lett. **26**, 375 (1975).

33. L. Becouarn, E. Lallier, M. Brevignon, and J. Lehoux, Opt. Lett. **23**, 1508 (1998).

34. T. Skauli, K. L. Vodopyanov, T. J. Pinguet, A. Schober, O. Levi, L. A. Eyres, M. M. Fejer, J. S. Harris, B. Gerard, L. Becouarn, E. Lallier, and G. Arisholm, Opt. Lett. **27**, 628 (2002).

35. M. Yamada, N. Nada, M. Saitoh, and K. Watanabe, Appl Phys Lett. **62**, 435 (1993).

36. J. Wejbjörn, V. Pruneri, P. S. J. Russel, J. R. M. Barr, and D. C. Hanna, Electron. Lett. **30**, 894 (1994)

37. H. Karlsson and F. Laurell, Appl. Phys. Lett. **71**, 3474 (1997).

38. L. K. Cheng, L. T. Cheng, J. Galperin, P. A. Morris Hotsenpiller and J. D. Bierlein, J. Cryst. Growth **137**, 107 (1994).

39. G. Hansson, H. Karlsson, S. Wang, and F. Laurell, Appl. Opt. **39**, 5058 (2000).

40. J. Hellström, G. Karlsson, V. Pasiskevicius, and F. Laurell, Opt. Lett. **26**, 352 (2001).

41. H. Karlsson, *Fabrication of periodically poled crystals from the KTP family and their applications in nonlinear optics*, PhD-thesis, ISSN 0280-316X, Royal Institute of Technology, Sweden (1999).

42. J. Hellström, *Nanosecond optical parametric oscillators and amplifiers based on periodically poled $KTiOPO_4$*, PhD-thesis, ISBN 91-7283-214-2, Royal Institute of Technology, Sweden (2001).

43. C. Canalias, *Domain Engineering in $KTiOPO_4$*, PhD-thesis, ISBN 91-7178-152-8, Royal Institute of Technology, Sweden (2005).

44. L.E. Myers, R.C. Eckardt, M.M. Fejer, R.L. Byer, and W.R. Bosenberg, Opt. Lett. **21**, 591 (1996).

45. K. Fradkin-Kashi and A. Arie, IEEE J. Quantum Electron. **35**, 1649 (1999).
46. K. A. Tillman, D. T. Reid, D. Artigas, J. Hellström, V. Pasiskevicius, and F. Laurell, J. Opt. Soc. Am. B **20**, 1309 (2003).
47. T. Sasaki, Y. Mori, M. Yoshimure, Y. K. Yap, and T. Kamimura, Mat. Sci. Eng. **30**, 1 (2000).
48. C. Chen, Z. Lin, and Z. Wang, Appl. Phys. B **80**, 1 (2005).
49. M. Ghotbi and M. Ebrahim-Zadeh, Opt. Express **12**, 6002 (2004).
50. C. Chen, Laser Focus World **40**, 91 (2004).
51. G.D. Boyd, E. Buehler, and F. G. Storz, Appl. Phys. Lett. **18**, 301 (1971).
52. J.-J. Zondy, Opt. Commun. **119**, 320 (1995).
53. R. L. Byer, H. Kildal, and R. S. Feigelson, Appl. Phys. Lett. **19,** 237 (1971).
54. K. L. Vodopyanov and P. G. Schunemann, Opt. Lett. **28**, 441 (2003).
55. K. L. Vodopyanov and P. G. Schunemann, Opt. Lett. **23**, 1096 (1998).
56. R. L. Byer and A. Piskarskas, J. Opt. Soc. Am. B **10**, 2148 (1993).
57. W. R. Bosenberg and R. C. Eckardt, J. Opt. Soc. Am B **12**, 2084 (1995).
58. L. E. Myers, G. D. Miller, R. C. Eckardt, M. M. Fejer, R. L. Byer, and W. R. Bosenberg, Opt. Lett. **20**, 52 (1995).
59. P. E. Powers, T. J. Kulp, and S. E. Bisson, Opt. Lett. **23**, 159 (1998).
60. V. Smilgevicius, A. Stabinis, A. Piskarskas, V. Pasiskevicius, J. Hellström, S. Wang and F. Laurell, Opt. Commun. **173**, 365 (2000).
61. M. J. Missey, V. Dominic and P. E. Powers, Opt. Lett. **24**, 1227 (1999).
62. O. Pacaud, J. P. Fève, B. Boulanger, and B. Menaert, Opt. Lett. **25**, 737 (2000).
63. J. P. Fève, O. Pacaud, B. Boulanger, B. Menaert, J. Hellström, V. Pasiskevicius, and F. Laurell, Opt. Lett. **26**, 1882 (2001).
64. V. Pasiskevicius, H. Karlsson, J. A. Tellefsen, F. Laurell, R. Butkus, A. Piskarskas, V. Smilgevicius, and A. Stabinis, Opt. Lett. **25**, 969 (2000).
65. S. T. Yang and S. P. Velsko, Opt. Lett. **24**, 133 (1999).
66. G. Arisholm, G. Rustad, and K. Stenersen, J. Opt Soc Am B **18**, 1882 (2001).
67. Y. He and B. J. Orr, Opt. Lett. **29**, 2169 (2004).
68. V. Smilgevicius, A. Stabinis, A. Piskarskas, V. Pasiskevicius, J. Hellström, S. Wang, and F. Laurell, Opt. Commun. **173**, 365 (2000).
69. T. Y. Fan, C. E. Huang, B. Q. Hu, R. C. Eckardt, Y. X Fan, R. L. Byer, and R. S. Fiegelson, Appl. Opt. **26**, 2390 (1987).
70. L. Bragg and H. Lipson, J. Scient. Instr. **20**, 110 (1943).

71. C. Chiang, Y. Y. Lin, T. D. Wang, Y. C. Huang, and J. T. Shy, Opt. Lett. **27**, 1815 (2002).
72. S. Victori, T. Lepine, P. Georges, and A. Brun, in *Advanced Solid-State Lasers*, M. E. Fermann and L. R. Marshall, eds., Vol. **68**, page 66 of OSA Proceedings Series (Optical Society of America, Washington, D.C., USA, 2002).
73. O. Efimov, L. Glebov, L. Glebova, K. Richardson, and V. Smirnov, Appl. Opt. **38**, 619 (1999).
74. L. B. Glebov, L. N. Glebova, V. I. Smirnov, M. Dubinskii, L. D. Merkle, S. Papernov, and A. W. Schmid, presented at the Solid State and Diode Laser Technology Review, Albuquerque, New Mexico, USA, 8-10 June 2004.
75. T. Chung, A. Rapaport, V. Smirnov, L. B. Glebov, M. C. Richardson, and M. Bass, Opt. Lett. **31**, 229 (2006).
76. B. Jacobsson, V. Pasiskevicius, and F. Laurell, Opt. Lett. to be published in June 2006.
77. H. Kogelnik, J. Bell Syst. Tech. **48**, 2909 (1969).
78. S. E. Harris, IEEE J. Quantum Electron. **2**, 701, (1966).
79. B. Hitz, "Bragg grating reduces OPO bandwidth by factor of 20," Photonics Spectra **39**, 106 (2005).
80. J.-C. Diels and W. Rudolph, *Ultrashort Laser Pulse Phenomena*, Academic Press, (1996)
81. X. Zhang and H. Giessen, Appl. Phys. **B 79**, 4417 (2004).
82. A. Varanavicius, A. Dubietis, A. Berzanskis, R. Danielius, and A. Piskarskas, Opt. Lett. **22**, 1603 (1997).
83. K. Gallo, P. Baldi, M. De Micheli, D.B. Ostowsky, and G. Assanto, Opt. Lett. **25**, 966 (2000).
84. M. Zavelani-Rossi, G. Cerullo, and V. Magni, IEEE J. Quantum Electron. **34**, 61 (1998).
85. R. Danielius, P. Di Trapani, A. Dubietis, A. Piskarskas, D. Podenas, and G. P. Banfi, Opt. Lett. **18**, 574 (1993).
86. J. Hellström, G. Karlsson, V. Pasiskevicius, and F. Laurell, Opt. Lett. 26, 352 (2001).
87. A. Fragemann, V. Pasiskevicius, G. Karlsson, F. Laurell, Opt. Express **11**, 1297 (2003).
88. K. W. Aniolek, R. L. Schmitt, T. J. Kulp, B. A. Richman, S. E. Bisson and P. E. Powers, Opt. Lett. **25**, 557 (2000).
89. M. Towrie, D. C. Grills, J. Dyer, J. A. Weinstein, P. Matousik, R. Barton, P. D. Bailey, N. Subramaniam, W. M. Kwok, C. Ma, D. Phillips, A. W. Parker, and M. W. George, Appl. Spectrosc. **57**, 367 (2003).
90. A. Scrinzi, M. Yu. Ivanov, and D. M. Villeneuve, J. Phys. B **39**, R1 (2006). (see reference within)

91. A. Gordon and F. X. Kärtner, Opt. Express **13**, 2941 (2005).
92. J. G. Fujimoto, Nature BioTech. **21**, 1361 (2003).
93. G. M. Gale, M. Cavallari, T. J. Driscoll, and F. Hache, Opt. Lett. **20**, 1562 (1995).
94. N. Ishii, L.Turi, V. S. Yakovlev, T. Fuji, F. Krausz, A. Baltuska, R. Butkus, G. Veitas, V. Smilgevicius, R. Danielius, and A. Piskarskas, Opt. Lett. **30**, 567, (2005).
95. F. Rotermund, V. Petrov, and F. Noack, Opt. Commun. **169**, 183 (1999).
96. K. Fradkin, A. Arie, A. Skliar, and G. Rosenman, Appl. Phys. Lett. **74**, 914 (1999).
97. K. Kato and E. Takaoka, Appl. Opt. **41**, 5040 (2002).
98. A. Baltuska and T. Kobayashi, Appl. Phys. B **75**, 427 (2002).
99. J. R. Lakowicz, *Principles of Fluorescence Spectroscopy*, 2nd edition, New York: KA/PP (1999).
100. *Optically Based Biological and Chemical Sensing for Defence*; Eds. J. C. Carrano and A. Zukauskas, Proc. SPIE, vol. **5617** (2004).
101. *Optically Based Biological and Chemical Sensing, and Optically Based Materials for Defence*; Eds. J. C. Carrano, A. Zukauskas, A. W. Vere, J. G. Grote, and F. Kajzar, Proc. SPIE, vol. **5990** (2005).
102. A. Sabelnikov, V. Zhukov, and R. Kempf, Biosens. Bioelectron. **21**, 2070 (2006).
103. D. R. Walt and D. R. Franz, Anal. Chem. **A-746**, 738 (2000).
104. J. Ho, Anal. Chim. Acta **457**, 125 (2002).
105. P. H. Kaye, W. R. Stanley, E. Hirst, E. V. Foot, K. L. Baxter and S. J. Barrington, Opt. Express **13**, 3583 (2005).
106. C. Gao, H. Laabs, H. Weber, T. Brand, and N. Kugler, Opt. Quantum Electron. **31**, 1207 (1999).
107. P. Jonsson, F. Kullander, M. Nordstrand, T. Tjärnhage, P. Wästerby, and M. Lindgren, Proc. SPIE **5617**, 61 (2004).
108. V. Sivaprakasam, A. L. Huston, C. Scotto, and J. D. Eversole, Opt. Express **12**, 4457 (2005)
109. http://www.weao.weu.int/. Project name: SOCRATE/CEPA 13/RTP13.13/RFP 017
110. J. Keskinen and K. Janka, Aero. Sci. Tech. **6**, 79 (1987).